MONTAN
UNIVERSITÄT
LEOBEN

Chair of Petroleum Geology

Doctoral Thesis

Advanced micromechanical and pore structural characterization of organic matter-rich rocks: Toward a better understanding of dual porosity and permeability

Sanja Vranješ-Wessely, MSc

May 2021

Affidavit

MONTANUNIVERSITÄT LEOBEN
www.unileoben.ac.at

AFFIDAVIT

I declare on oath that I wrote this thesis independently, did not use other than the specified sources and aids, and did not otherwise use any unauthorized aids.

I declare that I have read, understood, and complied with the guidelines of the senate of the Montanuniversität Leoben for "Good Scientific Practice".

Furthermore, I declare that the electronic and printed version of the submitted thesis are identical, both formally and with regard to content.

Date 22.05.2021

Sanja Vranjes-Wessely

Signature Author
Sanja Vranjes-Wessely

Abstract

In recent years, nano-scale material characterization in many geoscience disciplines and particularly in petroleum-related fields is becoming increasingly important. The necessity to understand transport properties of fine-grained, organic matter-rich rocks (including coals) for the purpose of unconventional hydrocarbon production (e.g., shale oil/gas, coal bed methane) represents a main driving force for method development in the field of high-resolution imaging and micromechanical characterization. A profound characterization of the nano-scale matrix pore system and the mechanical behavior of individual constituents from such low-permeability rocks helps to predict producibility of oil and gas. However, analysis at the nanometer scale still represents a major challenge in source rock studies, as many well-established, spatially-resolving characterization techniques have not been fully transferred from traditional material science to petroleum geoscience yet.

This thesis aims at filling this gap by providing a profound nano-scale characterization workflow for organic matter-rich rocks. Furthermore, it gives insights on the interdependency between nano-mechanical and micro-structural properties, as well as on the geological controlling factors of these. To do so, nanoindentation, a broad spectrum of high-resolution imaging techniques, and gas adsorption methods were applied on i) a well-investigated set of Carboniferous coal samples from the Ukrainian Donets Basin (0.62 – 1.47 %Rr vitrinite reflectance) and ii) Cretaceous shales from the Chinese Songliao Basin (1.33 – 2.23 %Rr).

The nanoindentation study on Donets coals revealed different impact factors on material parameters (hardness H and reduced elastic modulus E_r) for each maceral group. Mechanical parameters of liptinite seem to be mainly impacted by transformational processes, linked to thermal maturation and depositional environment, while H and E_r of inertinite are mainly controlled by the prevailing temperature during paleo-wildfires. In comparison, vitrinite macerals revealed a more complex evolution of H and E_r with thermal maturity. This might be due to the pore-structural evolution of vitrinite with increasing maturity, as observed during the subsequent high-resolution transmission electron microscopy (HRTEM) study. It was demonstrated that E_r of vitrinite is controlled by pore sizes, as smaller pores (≤ 5 nm) likely facilitate a more efficient load-sharing between individual pores. HRTEM imaging revealed further nano-structural heterogeneities in vitrinite, such as domains of higher ordering observed already at low-coal rank (0.69 and 0.81 %Rr). Low-pressure CO_2 and N_2 adsorption, Raman spectroscopy and high-pressure CH_4 sorption experiments collectively indicated severe structural changes at around 1.10 %Rr as a result of thermally induced processes marking the transition from peak oil to gas window.

In comparison to coal macerals, the micromechanical characterization of dispersed organic matter within shale rocks is further complicated due to mineral matrix effects and the small sizes of individual particles. The high-speed nanoindentation mapping and correlative imaging study on organic matter particles in fine-grained rocks of the Cretaceous Shahezi Formation (Songliao Basin), facilitated by femtosecond laser grids, revealed complex influencing factors on phase-specific micromechanical parameters. Various impacting effects were identified by correlative imaging (optical microscopy, scanning electron microscopy, and helium ion microscopy). Furthermore, the micromechanical raw data was processed by an unsupervised machine learning algorithm (*k*-means clustering). Future characterization and micromechanical modelling studies will benefit from the established, fast and reliable micromechanical and pore structural assessment workflows, including the presented sample preparation and data processing routines.

Kurzfassung

Die Materialcharakterisierung auf Nanoebene gewinnt in vielen geowissenschaftlichen Disziplinen, insbesondere den erdölbezogenen Fachbereichen, zunehmend an Bedeutung. Eine maßgeblich treibende Kraft für die Methodenentwicklung, sowohl im Bereich der hochauflösenden Bildgebung als auch der mikromechanischen Charakterisierung, ist das notwendige Verständnis von Transporteigenschaften komplexer, feinkörniger Gesteine mit einem hohen Anteil an organischer Substanz (einschließlich Kohle). Die resultierenden Erkenntnisse sind von besonderer Bedeutung für die unkonventionelle Kohlenwasserstoffgewinnung (z.B. Schieferöl/-gas, Flözgas). Jedoch stellen Untersuchungen auf Nanoebene für diese Proben eine besondere Herausforderung dar, da hochauflösende Charakterisierungstechniken, die vor allem in den Materialwissenschaften etabliert sind, noch nicht gänzlich für geowissenschaftliche Fragestellungen optimiert wurden. Diese Arbeit zielt darauf ab diese Lücke zu schließen indem ein Workflow für eine fundierte Charakterisierung im Nanobereich, geeignet für Gesteine mit hohem Anteil an organischer Substanz, entwickelt wird. Darüber hinaus werden sowohl Erkenntnisse über die Wechselwirkung zwischen den nanomechanischen Eigenschaften und Mikrostruktur, als auch deren geologische Kontrollfaktoren, untersucht. Dazu wurde Nanoindentierung, ein breites Spektrum an hochauflösenden Bildgebungsverfahren und Gasadsorptionsmethoden zur Untersuchung von i) Kohleproben aus dem Karbon im ukrainischen Donets Becken (0.62 – 1.47 %Rr Vitrinitreflexion) und ii) Kreide-zeitlichen Schiefergesteinen aus dem chinesischen Songliao Becken (1.33 – 2.23 %Rr) eingesetzt.

Die Nanoindentierungsstudie der Donets-Kohlen ergab unterschiedliche Einflussfaktoren auf die Materialparameter (Härte H and reduzierter Elastizitätsmodul E_r) der verschiedenen Mazeralgruppen. Die mechanischen Parameter von Liptinite-Mazeralen scheinen hauptsächlich von transformativen Prozessen, die im Zusammenhang mit der thermischen Reife stehen sowie Ablagerungsbedingungen, beeinflusst zu sein. H und E_r von Inertinit-Mazeralen werden hauptsächlich von Paläowaldbrand-Temperaturen kontrolliert. Im Vergleich dazu, zeigen Vitrinite eine komplexe Beziehung der mechanischen Parameter mit zunehmender Reife. Die weiterführende Studie, basierend auf der Untersuchung mittels hochauflösende Transmissionselektronenmikroskopie (HRTEM), zeigt, dass E_r von der Porengröße abhängt da kleinere Poren ($\leq$ 5 nm) wahrscheinlich eine effizientere Lastverteilung ermöglichen. HRTEM Aufnahmen zeigten weitere nanostrukturelle Heterogenitäten in Vitrinitpartikeln, wie beispielsweise Domänen höherer Ordnung bei niedriger Reife (0.69 und 0.81 %Rr). CO_2 and N_2 Adsorptionsmessungen, Raman Spektroskopie und Hochdruck CH_4 Sorptionsmessungen deuteten bei ca. 1.10 %Rr auf signifikante strukturelle Veränderungen hin.

Die mikromechanische Charakterisierung von fein verteilter organischer Substanz innerhalb von Schiefergestein ist im Vergleich zur Kohle aufgrund von Mineralmatrixeffekten und der geringen Größe der einzelnen Partikel deutlich erschwert. Organische Partikel in feinkörnigen Schiefergesteinen aus der Shahezi-Formation (Songliao Becken) wurden mikromechanisch mithilfe von Highspeed Nanoindentation Mapping sowie einer korrelativen Bildgebungsstudie hochauflösend charakterisiert. Durch den korrelativen Einsatz von optischer Mikroskopie, Rasterelektronenmikroskopie und Heliumionenmikroskopie konnten, erleichtert durch Femtosekundenlaserpräparation, komplexe Einflussfaktoren auf mechanische Parameter untersucht werden. Darüber hinaus wurden die mikromechanischen Rohdaten mithilfe von Unsupervised Machine Learning (*k*-means clustering) analysiert.

Zukünftige Charakterisierungs- und mikromechanische Modellierungsstudien werden von den etablierten, schnellen und zuverlässigen Workflows profitieren. Insbesondere durch die Probenpräparation und Routine der Datenanalyse.

Danksagung

Die vorliegende Arbeit ist das Ergebnis des interdisziplinären Dissertationsprojekts „Geomat“ der Lehrstühle Erdölgeologie und Materialphysik, dass vom Rektoratsprogramm „zur Förderung der interdisziplinären wissenschaftlichen Arbeit an der Montanuniversität“ gefördert wurde.

Die letzten Jahre hatte ich die große Ehre und das Privileg mit hervorragenden Wissenschaftler/innen, Kolleginnen und Kollegen zusammenzuarbeiten die mich auf dem Weg zur Promotion unterstützt haben. Diesen Menschen möchte ich an dieser Stelle aus tiefstem Herzen meinen Dank aussprechen, allen voran meinem tollen Betreuertrio:

Zuerst möchte ich mich bei Priv.-Doz. Dr. David Misch für die hervorragenden Zusammenarbeit, große Geduld und Unterstützung bedanken. Die vielen kritischen Diskussionen, inspirierenden Denkanstöße und motivierenden Gespräche haben wesentlich zum ständigen Fortschritt meiner wissenschaftlichen Herangehensweise und der Weiterentwicklung dieses Projekts beigetragen.

Ganz besonders möchte ich mich bei meinem Doktorvater Univ.-Prof. Dr. Reinhard Sachsenhofer für die hervorragende und geduldige Betreuung bedanken. Der intensive wissenschaftliche Diskurs mit meinem Doktorvater hat mir bei vielen Fragestellungen immens geholfen und mir ermöglicht in wichtigen Phasen dieses Projekts weitsichtiger zu denken.

Als nächstes möchte ich mich bei meinem Mentor Assoz. Prof. Dr. Daniel Kiener für die große Unterstützung und Hilfsbereitschaft bei allen materialwissenschaftlichen Fragestellungen herzlich bedanken. Seine Anregungen und sein Feedback haben mich stets inspiriert und einen wichtigen Beitrag zum Fortschritt dieser Arbeit geleistet.

Großer Dank gilt den vielen Kolleginnen und Kollegen die mich vor allem bei meinen Messungen und Experimenten unterstützt haben.

Merci beaucoup an Dr. Inas Issa für die tolle Unterstützung und Schulung am TEM. Die TEM Sessions waren für mich immer ein Highlight und es hat großen Spaß gemacht mit ihr zusammenzuarbeiten. Vielen Dank auch an Priv.-Doz. Dr. Megan J. Cordill für die engagierte Betreuung bei den Nanoindentierungs-Experimenten und dafür, dass ich trotz COVID-bedingten Beschränkungen weiterhin wichtige Messzeit für meine Arbeit in Anspruch nehmen durfte.

Es macht mich sehr traurig, dass ich ihm die fertige Arbeit nicht mehr zeigen kann, aber ich möchte zumindest diese Stelle nützen, meinem Nanoindentierungs-Lehrmeister Dr. Thomas Schöberl für seine Geduld und Herzlichkeit zu danken. Er ist mir zu Beginn meines Doktorates stets helfend und motivierend zur Seite gestanden.

Ich möchte mich bei Assoz. Prof. Dr. Doris Groß für die große Hilfe und geduldige Einschulung bei der organischen Petrographie und Schliffpräparation herzlich bedanken. Für die wertvolle und kreative Unterstützung bei der Präparation von Kohle- und Shaleproben möchte ich mich auch bei Ass.-Prof. Dr. Reinhard Gratzer bedanken.

Ein Dankeschön gebührt auch Ao.Univ.-Prof. Dr. Gerd Rantitsch für die engagierte Unterstützung bei der Raman Spektroskopie.

Im Zuge der herausfordernden Präparationsarbeiten und Messungen konnte ich sehr viel von talentierten Laborant/innen und Techniker/innen lernen. Dazu gehören insbesondere Silke Kaufmann, Marie-Luise Harmsen, Dipl.-Ing. Caroline Freitag und Gerhard Hawranek.

Vielen Dank an Alexandra Schellich und Ursula Schmid für die Hilfe in allen administrativen Belangen.

Ich möchte mich bei all meinen Co-Autor/innen, Kolleginnen und Kollegen der LEK-Petrophysikgruppe und des CIM der RWTH Aachen, der Fakultät für Physik der Universität Bielefeld, des Institute of Unconventional Oil and Gas der Northeast Petroleum University und der GEOS4 GmbH herzlich für ihre Unterstützung bedanken.

Ich möchte mich auch bei meiner Familie und meinen Freunden herzlich bdedanken:

Dankeschön an meine Freundin Dr. Sandra Baltić, die mit mir durch alle Höhen und Tiefen des Studiums und Alltags gegangen ist und immer für mich da war.

Hvala za sve Mama i Tata! Meinen Eltern Jelena und Nedeljko Vranješ möchte ich von Herzen für ihre ständige Unterstützung und ihren unerschütterlichen Glauben an mich danken. Kaum ein Mensch schafft es so wie meine Schwester Dejana Vranješ, mich in herausfordernden Zeiten aufzubauen und zum Lachen zu bringen. Danke für deine Unterstützung Dejana, du hast einen besonderen Platz in meinem Herzen.

Und zu guter Letzt möchte ich meiner großen Liebe, meinem besten Freund und Ehemann Lukas Wessely für alles danken. Du bist meine größte Stütze, ohne dich an meiner Seite, wäre ich nicht da, wo ich heute bin.

Inhaltsverzeichnis

General part of the thesis

1 Introduction and aim of the thesis

Over the course of the last two decades, nano-scale characterization of organic matter-rich rocks including coal became an essential approach in energy-related research. Apart from the central role of coal as an affordable and worldwide occurring fossil energy carrier (including production of coal bed methane), coal seams or coaly interlayers in organic-rich, fine-grained sedimentary successions may be prospective targets particularly for long term CO_2 storage (Li and Fang, 2014; Metz et al., 2005). Organic matter-rich mudstones and shales may source hydrocarbons of conventional oil and gas reservoirs, but also host enormous resources of shale oil/gas globally. Furthermore, such fine-grained rocks frequently form the geological barriers of conventional hydrocarbon reservoirs, which may be utilized for CO_2 and H_2 storage after the end of their hydrocarbon-production lifetime (Charlet et al., 2017; Khosrokhavar et al., 2014). Due to their favorable properties including low permeability, ductility, as well as considerable chemical and physical retention capacity, fine-grained sedimentary successions may also be suitable as permanent disposal sites for radioactive waste (Neuzil, 2013; Sassani et al., 2010). For all of these applications, a full understanding of the structural heterogeneities and resulting storage/transport behavior of these rocks is required. Particularly, the prediction of dual permeability, including matrix permeability assigned to matrix pores frequently at nanometer scale, as well as fracture permeability which may be naturally existent or induced by artificial stimulation procedures, is a key goal. Shale rocks are per definition fine-grained rocks that consist of >50% siliciclastic grains with sizes less than 62 µm (Boggs, 2006). Their compositional variability and organic-richness are related to the primary depositional setting, but also later diagenetic processes. Coal hosts mainly organic constitutes which were deposited as peat together with relatively minor amounts of inorganic mineral matter. The organic matter fraction of both shales and coals, which initially is mainly insoluble kerogen (Littke, 1993), is not only the source for gaseous and liquid hydrocarbons during proceeding thermal maturation (Clayton, 1993), but also shows a complex pore structural evolution in relation to transformational processes. These secondary changes contribute crucially to the overall effective porosity and sorptive storage capacity (Chalmers and Bustin, 2007; Crosdale et al., 1998; Gasparik et al., 2014; Löhr et al., 2015; Misch et al., 2019; Shabani et al., 2018). Furthermore, the organic matter content in shale rocks has reportedly a significant impact on their overall physical properties which in turn control the tendency to form fractures e.g., during hydraulic fracturing, but also influence wellbore stability and the interpretation of geophysical data such as seismic reflections and sonic logs (Khatibi et al., 2018; Kumar et al., 2015; Sayers, 2013; Vernik and Nur, 1992).

The inherent complexity of organic matter-rich rocks which goes down to micro- to nano-scale features, as well as the manifold changes in relation to diagenesis and organic matter transformation, represent a great challenge for both microstructural characterization and modelling approaches (Abedi et al., 2016). A wide spectrum of methods is used to resolve the textural and pore-structural characteristics, including i) petrophysical techniques such as low pressure N_2 and CO_2 physisorption, Hg intrusion (MICP), and nuclear magnetic resonance (NMR) porosimetry, ii) 3D tomographic techniques such as X-ray micro computed tomography (micro-CT), synchrotron-based nano-CT, and focused ion beam - scanning electron microscopy (FIB-SEM), as well as iii) 2D high-resolution imaging techniques such as broad ion beam - scanning electron microscopy (BIB-SEM), helium ion microscopy (HIM), and transmission electron microscopy (TEM) (e.g., Busch et al., 2017; Cała et al., 2017; Cardott and Curtis, 2018; Cavanaugh and Walls, 2016; Chalmers et al., 2012; Clarkson and Bustin, 1999; Fink et al., 2018; Harris and Yust, 1976; Kelly et al., 2016; King et al., 2015; Kwiecińska et al., 2019; Liu et al., 2017; Misch et al., 2018, 2016; Okolo et al., 2015; Zhao et al., 2018).

Conventional mechanical characterization (e.g., static or dynamic macro-scaled experiments) of organic matter-rich rocks is still challenging mainly due to poor core recovery and sample instability (e.g., Kumar et al., 2015). Furthermore, these standard testing routines often exhibit low precision and inconsistency due to sample heterogeneity, and the phase-specific properties of individual constituents cannot be extracted either. In contrast, nanoindentation is a powerful spatially resolved characterization method and well-established in many material science disciplines working with heterogeneous materials at the sub-micron scale (Oliver and Pharr, 2010, 1992). While not commonly applied, it has also proven feasible for shale rock testing (Abedi et al., 2016; Bennett et al., 2015; Cała et al., 2017; Graham et al., 2020; Luo et al., 2020; Ma et al., 2020; Shukla et al., 2015, 2013; Ulm and Abousleiman, 2006; Yang et al., 2020; Zhao et al., 2020), as well as for application with coals (Borodich et al., 2015; Epshtein et al., 2015; Hou et al., 2020; Kossovich et al., 2019; Ma et al., 2020; Manjunath and Jha, 2019; Yu et al., 2018). Still, method development both on the experimental as well as on the data processing side is urgently needed to lift nanoindentation up to its full potential with respect to geoscience-related research.

This thesis covers two main aspects:

At first, an improved structural and micromechanical characterization workflow for organic matter in both coals and shales should be established, as routines for a comprehensive assessment are still lacking. A major problem is that correlation between different investigation techniques is challenging and therefore, phase-specific organic matter properties cannot easily be determined. Furthermore, particularly micromechanical testing of disseminated fine-grained mudstones and shales requires post-processing of data in order to deconvolute material parameters of the present phases for later modelling approaches (Li et al., 2019; Liu et al., 2018; Luo et al., 2020; Wu et al., 2020). Pore structural investigations of organic matter often suffer from limitations in imaging resolution; the most common BIB-SEM technique is not able to visualize primary and secondary porosity in the lower mesopore range (< 10 nm). This applies in particular for the micropore (≤ 2 nm) range, which is of particular importance for the CH_4 sorption capacity in coal, as it is mainly controlled by the abundance of microporosity (e.g., Clarkson and Bustin, 1999). Therefore, additional imaging methods like TEM and HRTEM, ideally combined with gas adsorption data, are required to fill this resolution gap.

Secondly, this thesis aims at linking the structural evolution of organic matter during thermal maturation with the micromechanical changes observed. Due to the abovementioned importance of organic constituents for the development of dual porosity and permeability (matrix vs. fracture systems), these were put into the focus of this work. Two sample sets from the Ukrainian Donets Basin (Carboniferous coal; Sachsenhofer et al., 2012) and Chinese Songliao Basin (Lower Cretaceous Shahezi Formation shale; Hou et al., 2020) were selected for the experimental studies. The coal sample set was ideal for the clear identification of macerals and was therefore used to fundamentally understand the facies- and maturity-related influencing factors on changing structural and mechanical properties. The shale samples from the Shahezi Formation represent a potential shale gas target at wet gas to dry gas window maturity, for which the knowledge of mechanical behavior is of great importance. Nano-porous organic matter particles can be considered as preferred spots for stress-localization in shales, and depending on their brittle or ductile behavior could facilitate or impede crack propagation. The investigations on the coal and shale sample sets are briefly summarized below (see also the individual publication summaries in chapter 5).

Donbas coals

The first part (publications I and II) combines gas (ad)sorption measurements (N_2, CO_2, CH_4), highest-resolution imaging (particularly HRTEM), nanoindentation and characterization via Raman spectroscopy for a comprehensive assessment of maceral-specific coal properties over a broad maturity range (0.62 – 1.47 %Rr). Primary depositional and secondary diagenetic influences were considered and a general understanding of property evolution (H, E_r and pore structural parameters) could be established.

Songliao Basin shales

The second part (publication III) targets the micromechanical evaluation of dispersed organic matter (mainly vitrinite and solid bitumen) in overmature gas shales from the Lower Cretaceous Shahezi Formation of the Songliao Basin. A focus was set on the fast and reliable assessment of representative material parameters (H and E_r) of organic matter via high-speed nanoindentation mapping. These investigations were complemented by correlative optical and high-resolution imaging via BIB-SEM and HIM, to reliably identify organic matter types and exclude artefacts and measurements biased by grain boundary effects. Furthermore, the implementation of data post-processing by *k*-means clustering, an unsupervised machine learning algorithm, enabled the extraction of representative material parameters despite the small particle sizes.

The presented approach allowed to link facies- and maturity-related factors with property variations and yielded important micromechanical input data for use in future numerical fracture modelling at the microscale.

2 Depositional environments of coals and organic matter-rich rocks

Organic matter has a ubiquitous occurrence in sedimentary rocks and its amount is dependent on various biological, physical and chemical factors (Taylor et al., 1998). However, the preservation of organic matter is usually limited to aquatic environments where organic matter is produced more rapidly than it can be destroyed as the oxygen gets exhausted by its presence (Tourtelot, 1979; Welte, 1969). Despite its pervasive presence in the earth´s crust, economic hydrocarbon deposits can be considered as rare anomalies rather than the rule due to ideal geological conditions that are required (Littke, 1993). In this chapter, important depositional environments of organic matter rich rocks will be highlighted and discussed, predominantly based on the summary by Littke (1993).

2.1 Deep marine environments

Deep sea sediments cover a large part of the earth´s surface (Taylor et al., 1998). However, it was only through ocean drilling programs such as the Ocean Drilling Program (ODP) and the former Deep Sea Drilling Project (DSDP) that enabled organic geochemical and petrological studies on these sediments (Littke and Sachsenhofer, 1994). Organic matter in deep sea environments is characterized by all maceral groups; inertinite, vitrinite (indigenous and recycled from older, eroded sediments) and liptinite (Littke and Sachsenhofer, 1994; Taylor et al., 1998). Very little organic matter (<0.2 %, mostly inertinite) can be found in the central part of the oceans whereas along passive continental margins, in progradational submarine fans, vitrinite and terrigenous liptinite can be enriched. However, submarine fans also offer advantageous conditions for the preservation of organic matter due to favorable topography for hypersaline brines (Kennicutt et al., 1986). Generally, the preservation of organic matter is observed to be higher in shallow seas compared to deep marine environments (Vandenbroucke and Largeau, 2007). A further significant process for the preservation of organic matter is turbidity sedimentation due to rapid burial, especially for terrigenous macerals (Littke and Sachsenhofer, 1994; Taylor et al., 1998). Therefore, thick turbidite formation can represent favorable source rocks for gas (Taylor et al., 1998; Huang, 2018). Moreover, a great setting for oil source rocks is represented by anoxic silled basins (Black Sea as a recent example) (Demaison and Moore, 1980; Simmons et al., 2018). In such basins the anoxicity of bottom and pore water contribute to the preservation of produced organic carbon (Bralower and Thierstein, 1987). The resulting sediments in such settings are typically laminated black shales.

2.2 Upwelling areas

In upwelling areas, large masses of oceanic surface waters move offshore and are replaced by oceanic water from deep sea areas (Littke, 1993). These areas are characterized by high and continuous phytoplankton productivity as vertical currents constantly deliver nutrients to the photic zone (Parrish, 1982; Totman Parrish and Curtis, 1982). Upwelling currents are mainly wind-driven and a result of the Coriolis effect (Totman Parrish and Curtis, 1982). Examples for upwelling areas are offshore settings situated on the Northwest African shelf, Southwest Africa, Gulf of California, Peru and Oman (Diester-Haass, 1978; Littke, 1993 and references therein). However, depositional environments of upwelling zones are characterized by variability in typical characteristics of the respective upwelling zones such as oxygen content (not always anoxic), organic matter content, content of phosphorite, glauconite, opal, and barium (Demaison and Moore, 1980; Diester-Haass, 1978; Parrish, 1987, 1982). Differences in sedimentation mechanism can also be observed based on the organic matter type variability. The organic matter observed in upwelling sediments from prominent offshore sites such as Oman and Peru show a predominance of unstructured amorphous organic matter, so called bituminite. Whereas for the Northwest Africa shelf, the organic matter is mainly characterized by the high abundance of terrigenous macerals, in particular inertinites (Littke and Sachsenhofer, 1994). Differences in organic matter composition and consequently source rock quality are mainly a result of differing depositional conditions and oceanographic transport mechanisms (Langrock and Stein, 2004; Littke and Sachsenhofer, 1994). Overall, upwelling-influenced sediments have a significant role for the distribution of organic matter-rich rocks (Li et al., 2015; Parrish, 1987).

2.3 Anoxic continental shelves

Organic matter-rich sedimentary deposits in shallow and anoxic marine environments represent the most significant source rocks for oil. For instance, the Pennsylvanian black shales in North America represent typical and well-studied examples for depositions on anoxic continental shelves (Algeo and Heckel, 2008; Heckel, 1991; Littke, 1993; Schultz and Coveney, 1992). These deposits are usually relatively thin (<1 m) and normally do not host benthic fossils or show traces of bioturbation, which indicate that the sedimentation occurred under anoxic conditions (Littke, 1993; O'Brien, 1987). Organic petrography for the Upper Carboniferous Little Osage shale interval (USA) revealed that liptinitic (algal derived) as well as humic (terrestrial) macerals are present, exhibiting varying amounts and quality throughout the profile (liptinitic and organic carbon enrichment disappears towards the op of black shale interval) (Wenger and Baker, 1986). Organic matter and geochemical variations reveal that the level of anoxia was not constant and geological key factors such as eustatic sea level rise together with rapid marine transgression (influx of nutrients) mainly controlled the deposition. While the transgression-based influx of nutrients raised the algal production, input of terrigenous organic matter led to a considerable sink for oxygen levels which in consequence enhanced anoxia (Wenger et al., 1988; Wenger and Baker, 1986).

2.4 Lakes

Lakes represent advantageous depositional environments for prolific hydrocarbon source rocks (Kelts, 1988; Littke, 1993; Powell, 1986). European examples for organic matter-rich lacustrine sediments are Eocene Messel shales and Miocene Nördlicher Ries shale rocks (both Germany). These lacustrine sediments juxtaposed demonstrate the importance of various impact factors such as depositional setting, environmental conditions in the hinterland and water chemistry on organic matter composition (Littke, 1993). The organic matter-rich sequence (13 – 39 % C) of the Messel shale is a product of suitable environmental conditions such as a warm and humid climate, nutrient-rich freshwater input of an inflowing river, while in- and outflow did not disturb water stratification within the lake (Franzen und Michaelis, 1988; Rullkötter et al., 1988). Due to the fluviatile inflow, the kerogen in Messel shales consists of about 20% terrigenous higher plant material (vitrinite, inertinite) and the remaining 80% are derived by subaquatic organism (liptinite) (Jankowski and Littke, 1986; Rullkötter et al., 1988). Also, the sources for the organic matter input (autochthonous as well as allochthonous) varied the entire time while the lake existed (Bauersachs et al., 2014). However, the tectonic situation hindered sedimentation of a thick lacustrine sequence due to the development of Upper Rhein graben system. In contrast, the Nördlicher Ries shale, was not impacted by tectonic processes. The sediment was deposited in a Miocene meteoric impact crater and is characterized by organic carbon content between <2 and 26% (Littke, 1993; Rullkötter et al., 1990). Here, terrigenous macerals such as vitrinite and inertinite are significantly less abundant compared to the Messel shale rock, which is likely due to absent fluviatile transport mechanism through the Ries lake (Rullkötter et al., 1990). Another characteristic of the organic matter in the Ries shale is the abundance of structureless organic groundmass which is likely originated from cyanobacteria (blue-green algae) that could withstand hypersaline conditions prevailing within the Ries lake (Jankowski, 1983; Rullkötter et al., 1990).

Despite great variability, lakes represent an excellent depositional environment for oil-prone source rocks (Taylor et al., 1998). Due to the relatively small expansion of the aforementioned deposits, they have not been targeted for exploration as much as marine source rocks (Curiale and Gibling, 1994). However, lacustrine depositions are still investigated as potential economic source rocks (e.g., Browne et al., 2020; Liu et al., 2020; Song et al., 2020). The lacustrine basin fill of the Songliao Basin represents an exception with a thickness up to 4300 m (Hou et al., 2020; Taylor et al., 1998). The geological setting of the Songliao Basin is discussed in chapter 3.2.

2.5 Fluviodeltaic coal-bearing strata

Fluviodeltaic settings represent important depositional systems for coal and coal-bearing organic matter-rich-shale rocks (Dai et al., 2020). Sequences from this depositional setting are characterized by a high variability organic matter concentration (Littke, 1993). However, organic matter in fluviodeltaic sediments is dominated by terrigenous macerals derived from higher land plants (Omura et al., 2000; Scheidt and Littke, 1989; Scheihing and Pfefferkorn, 1984; Smyth, 1989). The organic matter composition can be generally described as a mixture of different maceral types. Littke (1993) provides a compilation of average maceral type percentage for different coal-bearing basins such as the Cenocoik Ardujan Basin, Jurassic Eromanga Basin, Permian Morondava Basin and the Carboniferous Ruhr basin (see figure 21 in Littke, 1993). The average vitrinite contents within these coal deposits range between 34 and 88%, average liptinite abundance ranges from 5 – 35% and average inertinite contents vary from 1 to 50%. Furthermore, the petrographic organic matter composition in clastic rocks can be comparable to the associated coal seams (Ramanampisoa et al., 1990; Scheidt and Littke, 1989) or a lower abundance in vitrinite can be observed. Another difference between the fluvial clastic rocks and related coal is that the organic matter disseminated in sediments is more degraded, leading to a lower petroleum generation capacity compared to the associated coal seam (Jasper et al., 2009; Littke and Zieger, 2020). However, the maceral composition can be highly variable. The relative enrichment of liptinite in the Ruhr Basin mudstones for instance can be explained by sorting processes during fluviatile transport mechanism due to its light weight, even at low velocities (Littke, 1993). Liptinite enrichment in also characteristic for fluviatile sediments such as the Pliocene to Pleistocene Uonuma Group (Japan). Here the high liptinite amounts are observed in estuary mouth sediments. This observation is viewed as a consequence of tidal, wave and fluvial currents (Omura et al., 2000).

3 Geological overview

3.1 Ukrainian Donets Basin

The Donets Basin (or Donbas), located largely in the Ukraine (figures 1a, b) and partly extending into Russia (eastern basin part), hosts one of the largest and most important coal fields worldwide. The basin extends over an area of 60 000 m^2 and contains approximately 130 economic coal seams and is one of the deepest sedimentary basins in Europe with a sediment thickness up to 19 km (Stovba et al., 1996) (figure 1c). Geologically it is the south-eastern part of the Pripyat–Dniepr–Donets Basin, a late Devonian rift structure within the southern part of the Eastern European Craton (Stephenson et al., 2001; Stovba and Stephenson, 1999). Sedimentation within the Donets Basin started in the Middle Devonian age with the deposition of shallow marine sediments (Stovba and Stephenson, 2002). The Devonian pre- and syn-rift sediment sequences are followed by post-rift filling of the Carboniferous, Permian, Mesozoic and Paleogene (Stovba et al., 1996). Devonian pre- and syn-rift sediments are widespread. They are about 750 m thick at the basin margins, but reach a thickness of about 5 to 6 km in the center of the basin (Maystrenko et al., 2003; figure 1c). Devonian syn-rift sequences include carbonate rocks, continental clastic, pyroclastic, volcanic and intrusive rocks and considerable amounts of salt (Maystrenko et al., 2003; Sachsenhofer et al., 2012; Stovba and Stephenson, 2002). As for the post-rift sediments, significant post-rift tectonic reactivations led to the development of the very thick (up to 14 km) Carboniferous succession (Sachsenhofer et al., 2012; Stephenson et al., 2006; Stovba and Stephenson, 2002). The Carboniferous sequence, consisting mainly of continental siliciclastic and shallow marine sediments as well as coal seams, are segmented into lithostratigraphic units, also named suites, A, B, C, to P (Lutugin and Stepanov, 1913). Their correlation with the standard time-scale is given by Sachsenhofer et al. (2003). Throughout the entire Carboniferous succession, coal seams are abundant. However, the Lower Serpukhovian (suite C) and Moscovian (suites K to M) are particularly rich in coal (Levenshtein et al., 1991). Serpukhovian coals, originated from a peat which was accumulated in an approximately 10 km wide shore-zone, characteristically exhibit low ash yield, have low to moderate S content, and are rich in inertinite and liptinite (Sachsenhofer et al., 2003, 2012). In contrast, Moscovian coals exhibit variable contents in sulphur (S) and ash yield and are rich in vitrinite. Furthermore, the aforementioned variability of S and ash yield of Moscovian seams indicate changing depositional environment with fluctuating marine influence (Misch et al., 2016a; Sachsenhofer et al., 2003).

The coal seams in the Donets Basin are characterized by a high CH_4 content which on one hand yields potential for economic productions but also represents a severe mine safety problem as Donets coal mines are prone to instantaneous outburst and gas explosions (Privalov et al., 2007; Sachsenhofer et al., 2012).

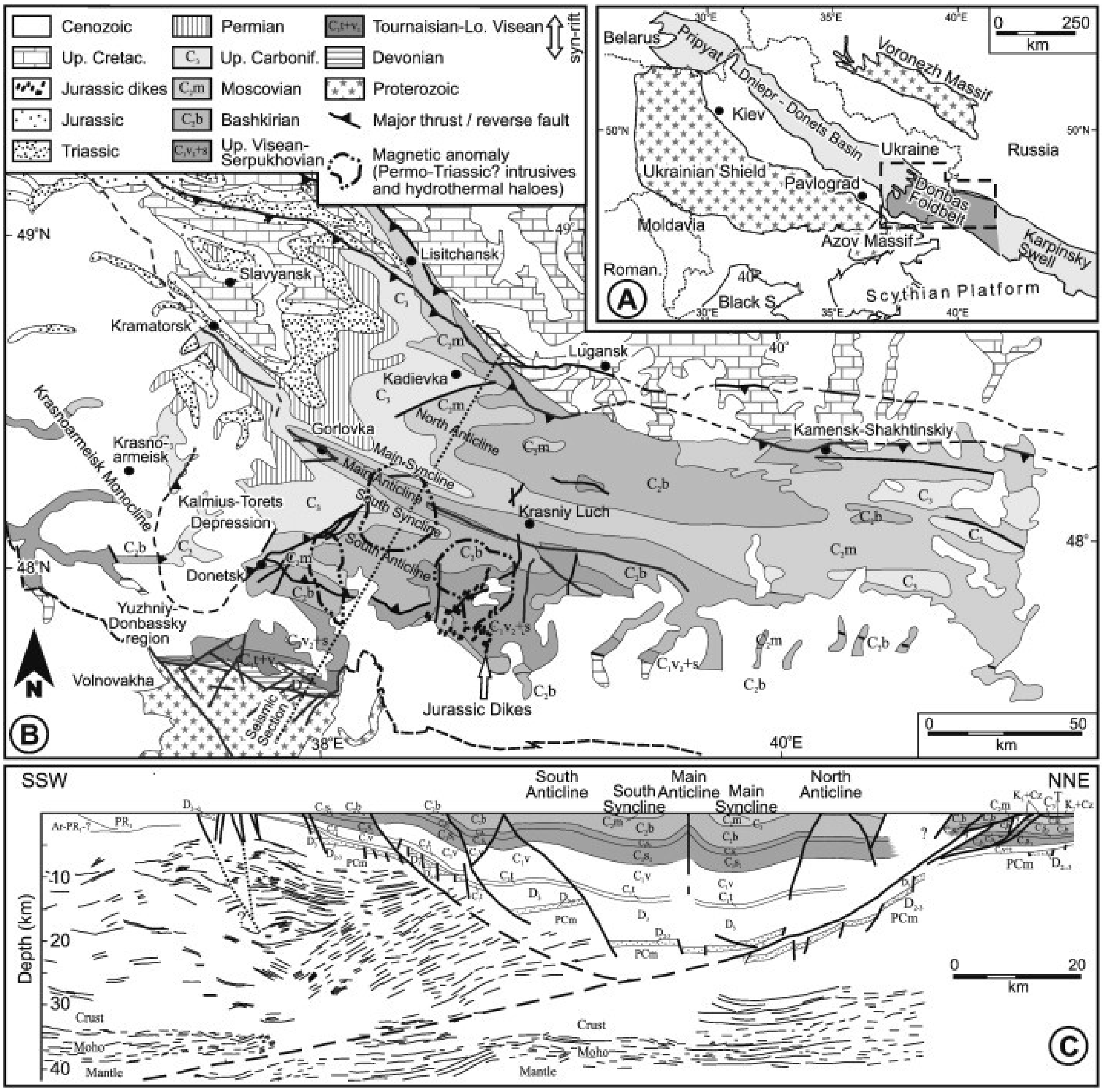

Figure 1. Maps and interpreted seismic lines from Sachsenhofer et al (2012). (A) Main location of the study area (after Stovba and Stephenson, 1999). (B) Geological map modified after Popov (1963) (C) Interpreted and depth-converted reflection seismic line after Maystrenko et al. (2003).

3.2 Chinese Songliao Basin

The Songliao Basin, located in northeastern China and eastern part of the Central Asian Orogen (figure 2a), is a Mesozoic rift basin covering an area of 260 000 km^2 (Hu et al., 1998). Paleozoic metamorphic rocks and Hercynian granites represent the basement. The basin fill reaches a thickness of more than 11 km and contains Jurassic, Cretaceous and Cenozoic sequences (Desheng et al., 1995; Hu et al., 1998). The Jurassic succession, deposited in rifts and reaching thickness values between 3 and 5 km, hosts mainly mudstones and sandstones interbedded with coal and volcanic rocks (Desheng et al., 1995). Sediments of early Cretaceous age overlie the Jurassic with an unconformity and are mainly represented by fluvial to shallow lacustrine sandstone and mudstones (Hu et al., 1998). During the main period of basin subsidence, Upper Cretaceous formations (Qingshankou, Yaojia and Nenjiang) were sedimented in an occasionally brackish influenced gigantic fresh water lake, which extended over an area of 90 000 to 100 000 km^2 (Hou et al., 2000). The Qingshankou and Nenjiang formations are the major petroleum source rock units within the Songliao basin. The lake was filled with fine-grained detrital sediments and has the longest continuous lacustrine sedimentation as well as subsidence history worldwide (Noah et al., 2020; Wang et al., 2017). Important new insights regarding stratigraphy, environmental evolution, paleoclimate, deep resource and energy exploration as well as tectonic settings were gained within the scope of the Deep Continental Scientific Drilling Engineering Project in the Songliao Basin (Hou et al., 2018; Xu et al., 2020). The Songke Number 2 well (also referred to as Well SK-2; figure 2), part of the aforementioned project and located in Anda City (Heilongjiang Province), is drilled down through the entire Cretaceous strata (Hou et al., 2018; figure 2b, c). The Shahezi and Huoshiling Formations were part of the main horizons drilled. Gas logging data of these formations revealed for 118 layers (cumulative thickness: 268 m) an abnormal high gas content (Hou et al., 2018). The extensive gas shows coupled with high organic matter abundance indicate the presences of energy sources in the deep Songliao Basin.

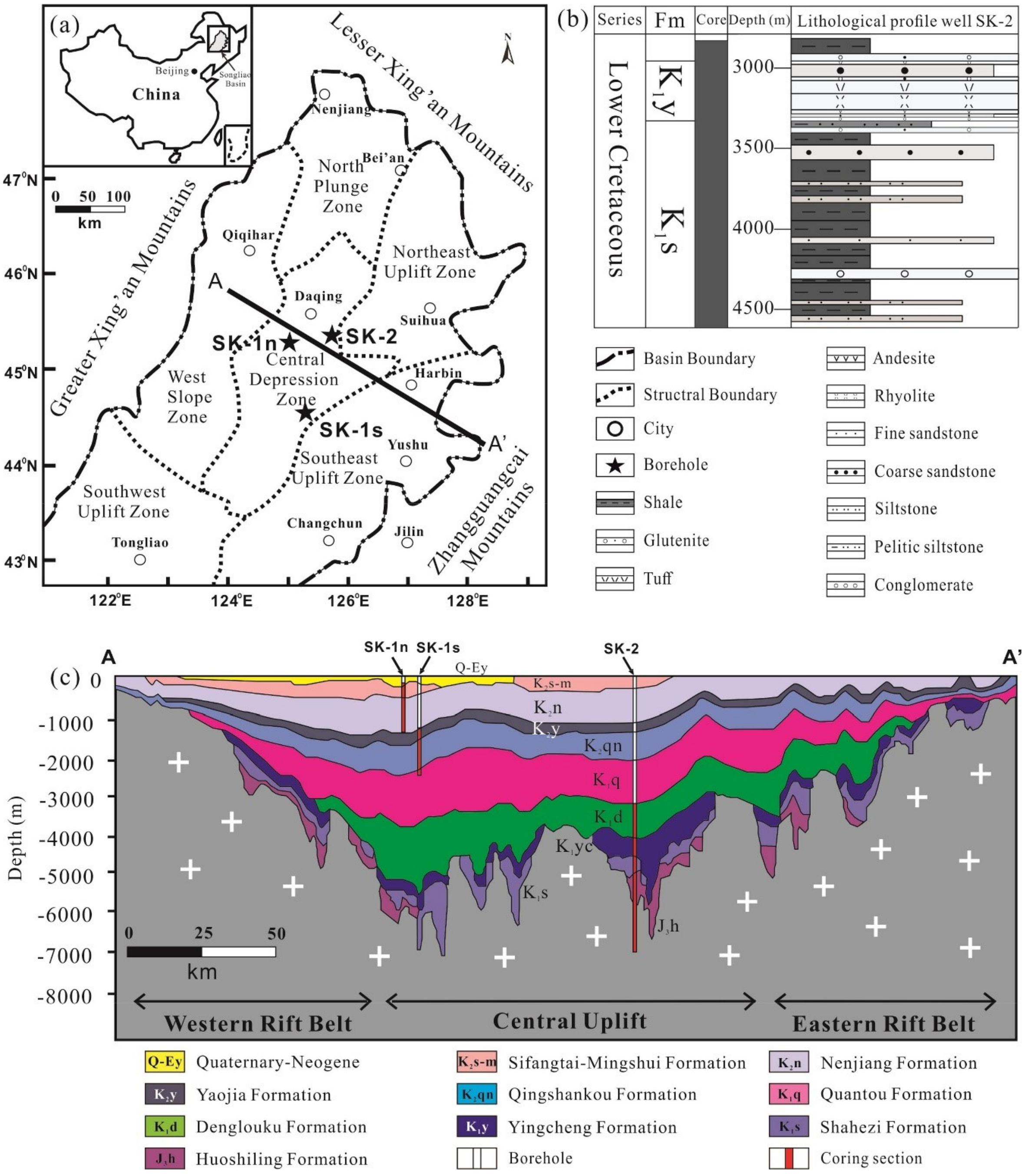

Figure 2: (a) Location of the Songliao Basin and SK-2 Well. (b) Stratigraphic column of the Lower Cretaceous in the SK-2 Well. (c) Structural cross-section of the Songliao Basin through the SK-2 Well. From Noah et al. (2020), modified after Hou et al. (2018).

4 Methods

The following section serves to provide a short overview of the characterization methods used in this study. Further details can be found in the respective cited literature.

4.1 Nanoindentation

To measure elastic and plastic properties with high spatial resolution, conventional nanoindentation testing and high-speed nanoindentation mapping were applied in this study. All measurements were conducted at the Erich Schmid Institute in Leoben (Austria). The samples (coal and shale rocks) were embedded in epoxy resin and mechanically polished (final polishing step: 0.05 μm). Conventional nanoindentation testing of Donets Basin coal macerals (see publication I) was conducted using a Hysitron (now Bruker) Triboscope system with the transducer being mounted on the scanner head of a Digital Instruments (now Bruker) D3100 atomic force microscope. This arrangement also enabled surface scans using the indentation tip as a probe to create a topological image of the investigated area. The indents were performed load-controlled with a trapezoidal loading profile with loading/unloading rates set to 500 μN s^{-1} and a maximum applied load of 1000 μN held for 10 s. Advanced high-speed nanoindentation mapping was conducted on organic matter particles in over-mature rocks from the Songliao Basin (see publication III). The measurements were performed using a Hysitron TS 77 Select (Bruker). Compared to conventional testing facilities, the Hysitron TS 77 Select enables accelerated data acquisition, allowing detailed statistical post-processing of a large data set. Maps with different sized grid patterns (up to 9 x 9 indents) and a spacing of 2 to 3 μm between the individual indentation spots, were positioned on macerals. The individual indents were performed with a trapezoidal loading profile (0.5 s loading, 1 s hold, 0.5 s unloading) in load-controlled mode to a maximum load of 800 μN. These load values were chosen to ensure small enough indents, thus avoiding unwanted interaction between neighboring imprints.

For both approaches, a Cube Corner diamond tip was selected as an indenter which also served as a scanning probe microscopy (SPM) tip. The attained SPM surface scans enable the identification of undisturbed spots prior to nanoindentation. The Cube Corner tip area function and load frame compliance for both systems were calibrated following the Oliver-Pharr method (Oliver and Pharr, 1992). Also, the proposed method by Oliver and Pharr (1992) was used to obtain hardness (H) and reduced elastic modulus (E_r).

H is calculated from Equation (1):

$$H = \frac{P_{max}}{A} \tag{1}$$

here P_{max} denotes the maximum load and A is the projected contact area between material and nanoindenter. E_r can be calculated following Equation (2):

$$E_r = \frac{\sqrt{\pi}}{2} \frac{S}{\sqrt{A}} \tag{2}$$

S defines the contact stiffness calculated as the slope of a tangent fitted to the upper portion of the unloading segment from the obtained load-displacement curve (figure 3). Theoretically, the diamond tip is also deformed elastically during nanoindentation, as it is not infinitely stiff. This can be considered through Equation (3):

$$\frac{1}{E_r} = \frac{1-\nu^2}{E} + \frac{1-\nu_i^2}{E_i} \tag{3}$$

where the Young's modulus of the tested material is denominated as E whereas its Poisson's ratio is described by v. The known material parameters for the diamond indenter tip are given by E_i and v_i. As the Poisson's ratios of macerals are not known, E_r was utilized and discussed as the main mechanical parameter. Furthermore, for soft materials, E and E_r are virtually equal, as the deformation of the diamond tip by the soft substrate is negligible.

The output data was subsequently statistically analyzed (see publication I and III). For the analysis of the acquired high-speed and high-throughput nanoindentation data, the unsupervised machine learning algorithm *k*-means clustering (Arthur and Vassilvitskii, 2007; Hartigan and Wong, 1979) was utilized to extract representative (e.g., non-affected by grain boundary effects) material parameters and to identify impacting factors causing the alteration of E_r and H of organic matter particles (see publication III).

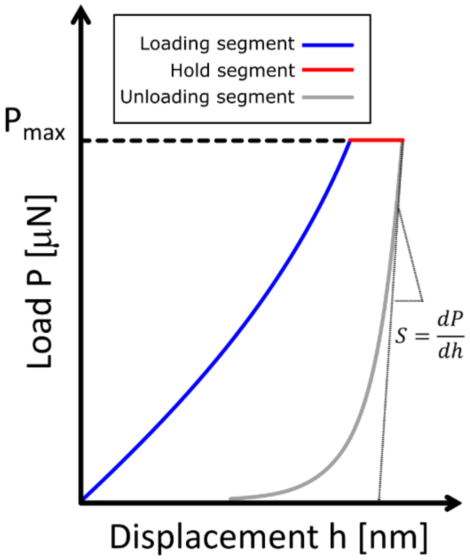

Figure 3: Sketch of a load-displacement curve.

4.2 Organic petrography

Organic petrography was conducted on the Donbas coals (publication I, II) as well as on the organic matter-rich rocks from the Songliao Basin (publication III). For the microscopy, the samples were embedded in epoxy resin and mechanically polished (final polishing step: 0.05 µm). The coal specimen was randomly embedded, while the shale rocks were cut and embedded perpendicular to their bedding plane. Organic matter was identified using a Leica DM 4P microscope under oil immersion. The microscope utilized in this study is located at the Chair of Petroleum Geology, Montanuniversität Leoben. Random reflectance measurements for inertinite (publication I) were conducted in non-polarized light (magnification of 100x) following Taylor et al. (1998). In order to enable a correlative imaging and mechanical testing approach, the sample surface (Songliao Basin shales) was marked with a femtosecond laser-grid (publication III). The grid preparation was realized with the Auriga Laser platform (Carl Zeiss) (Pfeifenberger et al., 2017) at the Erich Schmid Institute in Leoben (Austria). Under the microscope the three different maceral groups (vitrinite, intertinite and liptinite) can be distinguished from each other based on their reflectivity (Taylor et al., 1998). These groups contain various sub-groups and macerals which are described in detail by Stach et al. (1982) and Taylor et al. (1998). Detailed information is also given by the International Committee for Coal and Organic Petrology (ICCP) system. The vitrinite maceral group is mainly derived from woody tissues of stems, roots, barks and leaves which consist of cellulose and lignin (International Committee for

Coal and Organic Petrology (ICCP), 1998). Liptinite on the other hand, originates from non-humifiable plant matter, H-rich remains such as resins, waxes, fats and sporopollenin and is characteristically the maceral group exhibiting the lowest reflectance (Pickel et al., 2017). Inertinite macerals, mainly derived from woody tissue and resins, are the results of various alteration processes including redox and biochemical processes and oxidation due to wildfires (International Committee for Coal and Organic Petrology (ICCP), 2001).

4.3 Transmission electron microscopy

Transmission electron microscopy (TEM) imaging of vitrinite in Donbas coals (publication II) was performed on a 200 kV TEM JEOL 2100F equipped with a spherical aberration corrector (CEOS) and a Gatan Orius SC 1000 CCD camera at the Erich Schmid Institute in Leoben (Austria). Both, conventional bright field transmission electron microscopy (BF TEM) and high-resolution TEM (HRTEM) were conducted to determine pore characteristics and to visualize ultra-fine structures such as aromatic fringes, respectively. In order to obtain particles thin enough for proper analysis, material from vitrinite grains was carefully extracted with a scalpel and micro-drill bits. The extracted vitrinite powder was then diluted in isopropanol and dispersed by ultrasonication for 10 min. Few drops of the suspension containing vitrinite flakes were then deposited on a copper TEM grid with a lacey carbon film. The acquired micrographs from these particles were processed via the open-source software ImageJ (version 1.48) to acquire pore size distributions and geometry factors (see work flow in the supplemental material of publication II). Digital Micrograph (version 3.32) was used to analyze interlayer spacings between aromatic fringes by fast Fourier Transformation (FFT) based processing. An excellent summary of application and history of electron microscopy (TEM and SEM) in regards to the characterization of coals, organic matter-rich shales and carbonaceous matter is given by Kwiecińska et al. (2019) while further theoretical and practical insights are published by Williams and Carter (2009).

4.4 Scanning electron microscopy

Scanning electron microscopy (SEM) was conducted on a Tescan Clara field emission (FE)-SEM at the Chair of Physical Metallurgy and Metallic Materials, Montanuniversität Leoben (Austria). The microscope is equipped with backscattered (BSE) and secondary electron (SE) detectors as well as an energy-dispersive X-ray (EDX) detector (Oxford Instruments). In publication III the images were acquired in two steps. First, overview images of mechanically polished and uncoated samples were obtained at low electron beam energy (≤ 5 kV). For a detailed high-resolution imaging in the following step, sub-specimens were cut from these sample blocks in order to conduct cross-section milling of the sample surface by means of a Hitachi ArBlade 5000 broad ion beam (BIB) preparation system at 8 kV for 2 h. Subsequently, the samples were coated with few nm Au to prevent electron charging during high resolution imaging at 5 – 10 kV.

BIB surface preparation is recognized as non- or low-invasive method which enables the artefact free high-resolution characterization of fine-grained, organic matter-rich rock samples (Hackley et al., 2021; Klaver et al., 2012; Loucks et al., 2009; Misch et al., 2018).

4.5 Helium ion microscopy

The helium ion microscopy (HIM) characterization of organic matter particles in shale rocks from the Songliao Basin (publication III) was carried out using an Orion Plus microscope (Carl Zeiss) located at the Faculty of Physics, University of Bielefeld (Germany). HIM images were obtained at an acceleration voltage of 34.5 – 36.1 kV and a He beam current set at 0.3 – 2.9 pA. The samples were mechanically polished and the sample surface was not sputtered with a conductive layer in order to prevent artefacts that may result from coating (e.g., eventual clogging of pores). Charging of the surface during image acquisition was stabilized by using an electron flood gun. The resulting SE images offer great advantages to conventional SEM such as high surface sensitivity, an advantageous contrast formation, better depth of focus and far higher resolution, which is beneficial especially for carbon-based and biological materials (e.g., Frese et al., 2021; Joens et al., 2013).

Compared to SEM/BIB-SEM studies, HIM characterization of organic matter rich-rocks (e.g., Cavanaugh and Walls, 2016; Dong et al., 2019; Hackley et al., 2021; Huang et al., 2020; King et al., 2015; Wang et al., 2020) are not as common. Further theoretical background on imaging mechanism is given by excellent literature on HIM characterization (Bell, 2009; Hlawacek et al., 2014; Hlawacek and Gölzhäuser, 2016; Scipioni et al., 2009; Ward et al., 2006).

4.6 Raman spectroscopy

Raman spectroscopy was performed on a Horiba LabRAM HR Evolution spectrometer with a 532 nm Nd:Yag laser (100 mW; density-filtered down to 3.2 mW) for the characterization of vitrinite particles in Donbas coal (publication II). This facility is located at the Chair of Resource Mineralogy, Montanuniversität Leoben (Austria). The instrumental set-up also included a diffraction grating (1800 mm^{-1}), a CCD detector and a 10x microscope objective. Raman spectra were acquired from ablated vitrinite surfaces, in order to avoid influence of alteration effects caused by prior polishing (Henry et al., 2018; Lünsdorf, 2016). The evaluation of the spectra was performed using the Iterative Fitting of Raman Spectra (IFORS) approach, an iterative curve fitting method by Lünsdorf and Lünsdorf (2016). The structural parameters (based on the D and G band positions) were obtained to study the structural changes of vitrinite associated with thermal maturation (e.g., Potgieter-Vermaak et al., 2011).

4.7 Low-pressure adsorption

Low-pressure CO_2 as well as N_2 physisorption was conducted in order to study the pore-structural characteristics of vitrinite-rich Donbas bulk coals (publication II). Low-pressure CO_2 adsorption measurements were conducted at the Institute of Clay and Interface Mineralogy, RWTH Aachen University (Germany), while N_2 physisorption was provided by the Institute of Unconventional Oil and Gas, Northeast Petroleum University (China). Low-pressure CO_2 physisorption was performed on a Micromeritics Gemini VII 2390 t device. Approximately 0.2 g of the sieved 63 – 200 µm grain size fraction was analyzed per sample. All samples were dried and degassed for approximately 24 h at 383 K prior to measurements. The physisorption measurements were conducted at isothermal conditions (273) and further calculation of micropore volume and surface was based on the Dubinin-Astakhov equation (Dubinin, 1975). Low-pressure N_2 isotherms were acquired using a Micromeritics ASAP 2460 surface area and porosity analyzer at 77 K. Prior to measurements the samples (approximately 0.7 – 3 g of crushed 177 – 250 µm grain size fraction) were degassed and dried for 10 h at 383 K. Calculation of pore structural parameters such as specific mesopore volumes, mesopore size distributions as well as surface areas were based on the Barett-Joyner-Halenda (BJH) adsorption theory (Barrett et al., 1951).

4.8 High-pressure CH_4 sorption

High pressure CH_4 sorption experiments were conducted on at least 24 h dried and degassed (at 378 K) bulk coal samples from the Donets Basin (publication II). The high-pressure sorption measurements were conducted at Institute of Geology and Geochemistry of Petroleum and Coal, RWTH Aachen University (Germany). The crushed samples (<1 mm grain size) were analyzed using a manometric set-up. A detailed description of the experimental setup and device is given by Gasparik et al. (2014, 2013, 2012). The setup consists of volume calibrated steel sample cells (SC) and a reference cell (RC), including pressure and temperature transducers and two high-pressure valves (V1, V2) (figure 4). Before measuring the sorption isotherms, the system is leak-tested using He (leakage rate should not exceed 500 Pa/h). Subsequently, the void volume (V_{void}) of SC, filled with the sample powder, is determined by He expansion (RC into SC), under the assumption that He is not adsorbed by the sample. After removing He from the system via vacuum evacuation, the RC is repeatedly filled with CH_4 and successively expanded into the SC until a pressure of 10 MPa is reached.

Following Equation (4) the excess sorbed amount (n_{excess}) is calculated from the total amount of CH_4 transferred (n_{trans}) into the SC, subtracted by the amount of CH_4 that can be stored in the available void volume V_{void} (Gasparik et al., 2014):

$$n_{excess}(P,T) = n_{trans}(P,T) - \bar{\rho}_g(P,T)\, V_{void} \tag{4}$$

$\bar{\rho}_g$ denotes the molar gas density calculated as a function of the corresponding pressure (P) and temperature (T) by means of the GERG Equation of State (Kunz and Wagner, 2012). Parameterization of the resulting excess sorption isotherms was realized by a Langmuir-type function (Equation 5):

$$n_{excess} = n_L \frac{P}{P_L(T) + P} \tag{5}$$

Here, n_{excess} (mmol g^{-1}) is the excess amount of sorbed gas at given conditions (P and T) and n_L (mmol g^{-1}) denotes the maximum Langmuir capacity. The Langmuir pressure P_L (MPa) corresponds to the pressure where half of the sorption capacity is reached.

A general review on gas sorption processes (CH_4, CO_2) including different methods and set-ups for the sorption capacity determination is given by Busch and Gensterblum (2011).

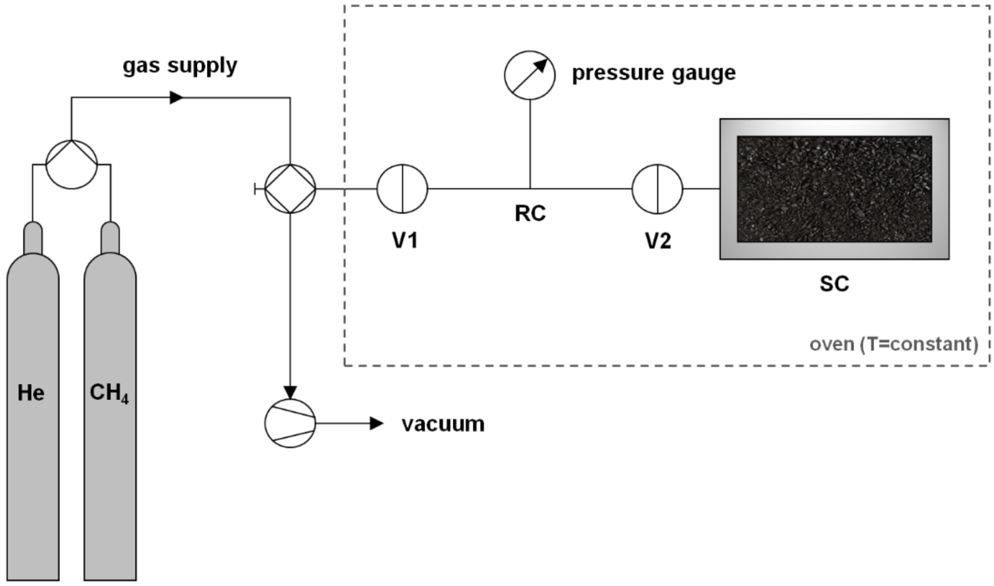

Figure 4: Illustrative representation of the manometric sorption set-up, modified after Gasparik et al. (2014).

5 Summary of publications

5.1 Publication I

Nanoindentation study of macerals in coals from the Ukrainian Donets Basin

Vranjes, S., Misch, D., Schöberl, T., Kiener, D., Gross, D., Sachsenhofer, R.F., 2018. Nanoindentation of macerals in coals from the Ukrainian Donets Basin. Adv Geosci. 45, 73–83. https://doi.org/10.5194/adgeo-45-73-2018

In this study, macerals within a maturity series of coals from the Ukrainian Donets Basin (0.62 – 1.47 %Rr) were micromechanically characterized via nanoindentation. Different thermal maturity trends were obtained for hardness H and reduced elastic modulus E_r of the three maceral groups (liptinite, vitrinite, inertinite). The E_r of liptinite followed a trend which is likely related to dehydration, progressing organization, decarboxylation and further transformation during thermal maturation. A low E_r value at ~0.7 %Rr could be linked to elevated organic sulphur contents reflecting a brackish depositional environment. The increased sulphur may have catalyzed organic matter transformation into hydrocarbons. H and E_r values of inertinite sub-macerals do not follow the vitrinite reflectance trend but correlate strongly with inertinite reflectance and hence paleo-wildfire conditions. This implies that the temperature exposure during these wildfire events might be the main controlling factor for inertinite brittleness. The mechanical parameters of vitrinite did not follow a clear maturity trend, probably due to the complex and interfering coalification processes active at bituminous coal rank. A relationship between mechanical behavior and pore-structural evolution of vitrinite could be proven by later highest-resolution imaging (see publication II).

5.2 Publication II

Nanoscale pore structure of Carboniferous coals from the Ukrainian Donets Basin: A combined HRTEM and gas sorption study

Vranjes-Wessely, S., Misch, D., Issa, I., Kiener, D., Fink, R., Seemann, T., Liu, B., Rantitsch, G., Sachsenhofer, R.F., 2020. Nanoscale pore structure of Carboniferous coals from the Ukrainian Donets Basin: A combined HRTEM and gas sorption study. Int. J. Coal Geol. 224, 103484. https://doi.org/10.1016/j.coal.2020.103484

This study combines TEM and HRTEM imaging, low-pressure adsorption (CO_2 and N_2), high-pressure CH_4 sorption experiments, and Raman spectroscopy to link chemical and structural changes of vitrinite macerals during progressing thermal maturation. The TEM-based investigations allowed the direct determination of pore size distributions and pore morphologies, and gave insight into ordering processes and nano-structural features such as aromatic fringes and semi-graphite-like domains. Furthermore, the elevated organic sulphur in these low-maturity vitrinite particles due to marine/brackish depositional conditions may have triggered early hydrocarbon generation and therefore development of secondary cracking pores. This is supported by the presence of semi-graphite-like domains, which is unusual at such low rank and may be the result of structural modifications catalyzed by the presence of sulphur. The presence of onion-like carbons at slightly higher vitrinite reflectance (0.82 %Rr) also indicates the formation of such well-ordered structures at temperatures lower than initially expected. A striking finding was the absence of TEM-visible microporosity (≤ 2 nm) and a lowered pore abundance at 0.93 and 1.10%Rr, probably indicating pore occlusion by bitumen. This phenomenon is supported by a small drop in CH_4 sorption capacity and a pronounced minimum in CO_2 micropore volume. Furthermore, a sudden increase in Raman spectral ordering and a sudden increase in mesopore (2 – 50 nm) volume and internal surface area obtained from low-pressure N_2 adsorption indicate significant thermally-induced changes at the transition from the peak oil to the early wet gas window. A maximum of micropore volume at the highest investigated rank (1.47 %Rr) documents the ongoing secondary cracking and/or expulsion of bitumen.

The pore size distributions obtained from HRTEM could be linked to the micromechanical properties. Average reduced elastic modulus values correlated well with average pore diameters in the size range ≤ 5 nm (pores not seen and hence not avoided during nanoindentation) obtained from HRTEM. Smaller mesopores are likely favorable for stiffness, as the applied load is shared more efficiently by a higher number of pores. This is an important insight for future micromechanical modelling of coal bed methane and other unconventional hydrocarbon production targets.

5.3 Publication III

High-speed nanoindentation mapping of organic matter-rich rocks: A critical evaluation by correlative imaging and machine learning data analysis

Vranjes-Wessely, S., Misch, D., Kiener, D., Cordill, M.J, Frese, N., Beyer, A., Horsfield, B., Wang, C., Sachsenhofer, R.F., under review. High-speed nanoindentation mapping of organic matter-rich rocks: A critical evaluation by correlative imaging and machine learning data analysis. Int. J. C Geol.

This paper focuses mainly on the fast and reliable acquisition of micromechanical data from dispersed organic matter in fine-grained rocks. For this, organic matter-rich shales from the Lower Cretaceous Shahezi Formation in the Songliao Basin were selected for a comprehensive imaging and high-speed nanoindentation mapping study. The correlative imaging by different microscopy techniques (optical microscopy, scanning electron microscopy, and helium ion microscopy) was facilitated by a novel femto-second laser preparation method. This allowed to mark the sample surfaces with a microscale grid without major thermally-induced damage. Features of interest could be identified reliably and investigated subsequently at different scales by the complementary characterization techniques. Secondary electron images obtained by HIM were found to be a great tool to identify nanoscale artefacts (e.g., cracks at mineral – organic matter interfaces, surface alteration caused by the testing procedure) due to the high topographic resolution provided by the helium ion beam. Data processing by the unsupervised machine learning algorithm *k*-means clustering was used to exclude grain boundary effects and heterogeneities related to structural variations (including artefacts). This allowed to derive representative E_r and H values from the nanoindentation property maps despite the small size of individual organic matter particles, and helped to refine the observed thermal maturity trends. The established nanoindentation testing and data processing routine successfully highlights the potential of nanoindentation mapping for future studies on fine-grained sedimentary rocks. The obtained material parameters are of utmost importance for future micromechanical modelling of shales as unconventional reservoir rocks and potential geological barriers.

5.4 List of conference contributions related to this thesis

Vranjes, S., Schöberl, T., Misch, D., Kiener, D., Sachsenhofer, R.F. (2018). Micromechanical properties of macerals in coals from the Ukrainian Donets Basin: maturity trends and implications for unconventional hydrocarbon production. EGU General Assembly 2018, Vienna, Austria, 8/04/18 - 13/04/18. *Poster presentation*.

Vranjes-Wessely, S., Misch, D., Schöberl, T., Kiener, D., Groß, D., Sachsenhofer, R.F. (2018). Mechanical properties of coal macerals: A nanoindentation study. Pangeo 2018, Vienna, Austria, 24/09/18 - 26/09/18. *Poster presentation*.

Vranjes-Wessely, S., Misch, D., Kiener, D., Rantitsch, G., Groß, D., Sachsenhofer, R.F. (2019). TEM characterisation and Raman spectroscopy of vitrinite. EMAS 2019 - 16th European Workshop on Modern Developments and Applications in Microbeam Analysis, Trondheim, Norway, 19/05/19 - 23/05/19. *Poster and oral presentation*.

Vranjes-Wessely, S., Misch, D., Issa, I., Kiener, D., Fink, R., Liu, B., Seemann, T., Rantitsch, G., Groß, D., Sachsenhofer, R.F. (2019). Pore-structural evolution of coals: Insights from high-resolution transmission electron microscopy and gas sorption. ICCS&T 2019-International Conference on Coal Science & Technology, Kraków, Poland, 24/11/19 - 28/11/19. *Poster presentation*.

Vranjes-Wessely, S., Misch, D., Cordill, M.J., Kiener, D., Horsfield, B., Wang, C., Sachsenhofer, R.F. (2020). Nanoindentation of gas shales – analytical potential and limitations. MSE Congress, online conference, 22/09/20 - 25/09/20. *Oral presentation*.

6 Concluding remarks

The results of this thesis highlight that acknowledging the scale-dependency of organic matter properties, as well as the countless primary and secondary influencing factors involved, are key requirements in order to obtain reliable structural and micromechanical characteristics. A comprehensive use of techniques that capture the inherent heterogeneity of geological samples, at the same time offering a maximum resolution sufficient to understand smallest-scale structural modifications, proved to be a successful approach that should be followed by future studies. Furthermore, spatial resolution is also significant when it comes to the micromechanical characterization of organic constituents in coal and fine-grained sedimentary rocks. Nanoindentation proved a valuable tool in this regard, and particularly high-speed nanoindentation mapping will enable the rapid acquisition of phase-specific properties which may be used in later numerical modelling approaches. The analytical results highlighted the multiple and competing influencing factors controlling the micromechanical property variations in a single sample. This implies that a) universal theories of pore-structural evolution and micromechanical behavior should be viewed critically and b) for a holistic understanding, it is important to combine traditional data from organic petrography, bulk geochemistry, and petrophysics with modern cutting-edge characterization techniques able to provide previously non-accessible phase-specific properties. The introduced workflows and methodological improvements considerably contribute to a faster and more reliable acquisition of spatially-resolved and representative material properties; however, great advancements due to a better accessibility of highest-resolution imaging and mechanical testing techniques – and the increasing development of such experiments towards in-situ conditions – are joyfully anticipated.

7 References

Abedi, S., Slim, M., Ulm, F.-J., 2016. Nanomechanics of organic-rich shales: the role of thermal maturity and organic matter content on texture. Acta Geotech. 11, 775–787. https://doi.org/10.1007/s11440-016-0476-2

Algeo, T.J., Heckel, P.H., 2008. The Late Pennsylvanian Midcontinent Sea of North America: A review. Palaeogeogr. Palaeoclimatol. Palaeoecol. 268, 205–221. https://doi.org/10.1016/j.palaeo.2008.03.049

Bauersachs, T., Schouten, S., Schwark, L., 2014. Characterization of the sedimentary organic matter preserved in Messel oil shale by bulk geochemistry and stable isotopes. Palaeogeogr. Palaeoclimatol. Palaeoecol. 410, 390–400. https://doi.org/10.1016/j.palaeo.2014.06.015

Bell, D.C., 2009. Contrast Mechanisms and Image Formation in Helium Ion Microscopy. Microsc. Microanal. 15, 147–153. https://doi.org/10.1017/S1431927609090138

Bennett, K.C., Berla, L.A., Nix, W.D., Borja, R.I., 2015. Instrumented nanoindentation and 3D mechanistic modeling of a shale at multiple scales. Acta Geotech. 10, 1–14. https://doi.org/10.1007/s11440-014-0363-7

Boggs, S., 2006. Principles of sedimentology and stratigraphy, 4th ed. ed. Pearson Prentice Hall, Upper Saddle River, N.J.

Borodich, F.M., Bull, S.J., Epshtein, S.A., 2015. Nanoindentation in studying mechanical properties of heterogeneous materials. J. Min. Sci. 51, 470–476. https://doi.org/10.1134/S1062739115030072

Bralower, T.J., Thierstein, H.R., 1987. Organic carbon and metal accumulation rates in Holocene and mid-Cretaceous sediments: palaeoceanographic significance. Geol. Soc. Lond. Spec. Publ. 26, 345–369. https://doi.org/10.1144/GSL.SP.1987.026.01.23

Browne, G.H., Adams, C.J., Campbell, H.J., Kennedy, E.M., Raine, J.I., Strogen, D.P., Sahoo, T.R., 2020. Fluvial and lacustrine successions in the youngest part of the Murihiku Supergroup, New Zealand. Gondwana Res. 78, 58–76. https://doi.org/10.1016/j.gr.2019.08.001

Busch, A., Gensterblum, Y., 2011. CBM and CO2-ECBM related sorption processes in coal: A review. Int. J. Coal Geol. 87, 49–71. https://doi.org/10.1016/j.coal.2011.04.011

Busch, A., Schweinar, K., Kampman, N., Coorn, A., Pipich, V., Feoktystov, A., Leu, L., Amann-Hildenbrand, A., Bertier, P., 2017. Determining the porosity of mudrocks using methodological pluralism. Geol. Soc. Lond. Spec. Publ. 454, 15–38. https://doi.org/10.1144/SP454.1

Cała, M., Cyran, K., Kawa, M., Kolano, M., Łydżba, D., Pachnicz, M., Rajczakowska, M., Różański, A., Sobótka, M., Stefaniuk, D., Stopkowicz, A., Wałach, D., 2017. Identification of Microstructural Properties of Shale by Combined Use of X-Ray Micro-CT and Nanoindentation Tests. Procedia Eng., ISRM European Rock Mechanics Symposium EUROCK 2017 191, 735–743. https://doi.org/10.1016/j.proeng.2017.05.239

Cardott, B.J., Curtis, M.E., 2018. Identification and nanoporosity of macerals in coal by scanning electron microscopy. Int. J. Coal Geol., SI:TSOP/AASP/ICCP Houston 190, 205–217. https://doi.org/10.1016/j.coal.2017.07.003

Cavanaugh, T., Walls, J., 2016. Multiresolution Imaging of Shales Using Electron and Helium Ion Microscopy, in: Olson, T. (Ed.), Imaging Unconventional Reservoir Pore Systems. American Association of Petroleum Geologists, pp. 65–76. https://doi.org/10.1306/13592017M1123693

Chalmers, G.R., Bustin, R.M., Power, I.M., 2012. Characterization of gas shale pore systems by porosimetry, pycnometry, surface area, and field emission scanning electron microscopy/transmission electron microscopy image analyses: Examples from the Barnett, Woodford, Haynesville, Marcellus, and Doig units. AAPG Bull. 96, 1099–1119. https://doi.org/10.1306/10171111052

Chalmers, G.R.L., Bustin, R.M., 2007. The organic matter distribution and methane capacity of the Lower Cretaceous strata of Northeastern British Columbia, Canada. Int. J. Coal Geol. 70, 223–239. https://doi.org/10.1016/j.coal.2006.05.001

Charlet, L., Alt-Epping, P., Wersin, P., Gilbert, B., 2017. Diffusive transport and reaction in clay rocks: A storage (nuclear waste, CO2, H2), energy (shale gas) and water quality issue. Adv. Water Resour. 106, 39–59. https://doi.org/10.1016/j.advwatres.2017.03.019

Clarkson, C.R., Bustin, R.M., 1999. The effect of pore structure and gas pressure upon the transport properties of coal: a laboratory and modeling study. 1. Isotherms and pore volume distributions. Fuel 78, 1333–1344. https://doi.org/10.1016/S0016-2361(99)00055-1

Clayton, J.L., 1993. Composition of Crude Oils Generated from Coals and Coaly Organic Matter in Shales: Chapter 8 180, 185–201.

Crosdale, P.J., Beamish, B.B., Valix, M., 1998. Coalbed methane sorption related to coal composition. Int. J. Coal Geol. 35, 147–158. https://doi.org/10.1016/S0166-5162(97)00015-3

Curiale, J.A., Gibling, M.R., 1994. Productivity control on oil shale formation—Mae Sot Basin, Thailand. Org. Geochem. 21, 67–89. https://doi.org/10.1016/0146-6380(94)90088-4

Dai, S., Bechtel, A., Eble, C.F., Flores, R.M., French, D., Graham, I.T., Hood, M.M., Hower, J.C., Korasidis, V.A., Moore, T.A., Püttmann, W., Wei, Q., Zhao, L., O'Keefe, J.M.K., 2020. Recognition of peat depositional environments in coal: A review. Int. J. Coal Geol. 219, 103383. https://doi.org/10.1016/j.coal.2019.103383

Arthur, D., Vassilvitskii, S., 2007. K-Means++: The Advantages of Careful Seeding. Proc. Eighteenth Annu. ACM-SIAM Symp. Discrete Algorithms 1027–1035.

Demaison, G.J., Moore, G.T., 1980. Anoxic environments and oil source bed genesis. Org. Geochem. 2, 9–31. https://doi.org/10.1016/0146-6380(80)90017-0

Desheng, L., Renqi, J., Katz, B.J., 1995. Petroleum Generation in the Nonmarine Qingshankou Formation (Lower Cretaceous), Songliao Basin, China, in: Katz, Barry J. (Ed.), Petroleum Source Rocks, Casebooks in Earth Sciences. Springer Berlin Heidelberg, Berlin, Heidelberg, pp. 131–148. https://doi.org/10.1007/978-3-642-78911-3_8

Diester-Haass, L., 1978. Sediments as Indicators of Upwelling, in: Boje, R., Tomczak, M. (Eds.), Upwelling Ecosystems. Springer Berlin Heidelberg, Berlin, Heidelberg, pp. 261–281. https://doi.org/10.1007/978-3-642-66985-9_19

Dong, T., Harris, N.B., McMillan, J.M., Twemlow, C.E., Nassichuk, B.R., Bish, D.L., 2019. A model for porosity evolution in shale reservoirs: An example from the Upper Devonian Duvernay Formation, Western Canada Sedimentary Basin. AAPG Bull. 103, 1017–1044. https://doi.org/10.1306/10261817272

Dubinin, M.M., 1975. Physical Adsorption of Gases and Vapors in Micropores, in: Cadenhead, D.A., Danielli, J.F., Rosenberg, M.D. (Eds.), Progress in Surface and Membrane Science. Elsevier, pp. 1–70. https://doi.org/10.1016/B978-0-12-571809-7.50006-1

Epshtein, S.A., Borodich, F.M., Bull, S.J., 2015. Evaluation of elastic modulus and hardness of highly inhomogeneous materials by nanoindentation. Appl. Phys. A 119, 325–335. https://doi.org/10.1007/s00339-014-8971-5

Fink, R., Amann-Hildenbrand, A., Bertier, P., Littke, R., 2018. Pore structure, gas storage and matrix transport characteristics of lacustrine Newark shale. Mar. Pet. Geol. 97, 525–539. https://doi.org/10.1016/j.marpetgeo.2018.06.035

Franzen, J.L., Michaelis, W. 1988. (eds.) Der eozäine Messelsee - Eocene Lake Messel. Cour. Forsch.-Inst. Senckenberg, 107, 452p.

Frese, N., Schmerer, P., Wortmann, M., Schürmann, M., König, M., Westphal, M., Weber, F., Sudhoff, H., Gölzhäuser, A., 2021. Imaging of SARS-CoV-2 infected Vero E6 cells by helium ion microscopy. Beilstein J. Nanotechnol. 12, 172–179. https://doi.org/10.3762/bjnano.12.13

Gasparik, M., Bertier, P., Gensterblum, Y., Ghanizadeh, A., Krooss, B.M., Littke, R., 2014. Geological controls on the methane storage capacity in organic-rich shales. Int. J. Coal Geol., Special issue: Adsorption and fluid transport phenomena in gas shales and their effects on production and storage 123, 34–51. https://doi.org/10.1016/j.coal.2013.06.010

Gasparik, M., Ghanizadeh, A., Bertier, P., Gensterblum, Y., Bouw, S., Krooss, B.M., 2012. High-Pressure Methane Sorption Isotherms of Black Shales from The Netherlands. Energy Fuels 26, 4995–5004. https://doi.org/10.1021/ef300405g

Gasparik, M., Ghanizadeh, A., Gensterblum, Y., Krooss, B.M., 2013. “Multi-temperature” method for high-pressure sorption measurements on moist shales. Rev. Sci. Instrum. 84, 085116. https://doi.org/10.1063/1.4817643

Graham, S.P., Rouainia, M., Aplin, A.C., Cubillas, P., Fender, T.D., Armitage, P.J., 2020. Geomechanical characterisation of organic-rich calcareous shale using AFM and nanoindentation. Rock Mech. Rock Eng. https://doi.org/10.1007/s00603-020-02261-6

Hackley, P.C., Jubb, A.M., McAleer, R.J., Valentine, B.J., Birdwell, J.E., 2021. A review of spatially resolved techniques and applications of organic petrography in shale petroleum systems. Int. J. Coal Geol. 103745. https://doi.org/10.1016/j.coal.2021.103745

Harris, L.A., Yust, C.S., 1976. Transmission electron microscope observations of porosity in coal. Fuel 55, 233–236. https://doi.org/10.1016/0016-2361(76)90094-6

Hartigan, J.A., Wong, M.A., 1979. Algorithm AS 136: A K-Means Clustering Algorithm. Appl. Stat. 28, 100. https://doi.org/10.2307/2346830

Heckel, P.H., 1991. Thin widespread Pennsylvanian black shales of Midcontinent North America: a record of a cyclic succession of widespread pycnoclines in a fluctuating epeiric sea. Geol. Soc. Lond. Spec. Publ. 58, 259–273. https://doi.org/10.1144/GSL.SP.1991.058.01.17

Henry, D.G., Jarvis, I., Gillmore, G., Stephenson, M., Emmings, J.F., 2018. Assessing low-maturity organic matter in shales using Raman spectroscopy: Effects of sample preparation and operating procedure. Int. J. Coal Geol. 191, 135–151. https://doi.org/10.1016/j.coal.2018.03.005

Hlawacek, G., Gölzhäuser, A. (Eds.), 2016. Helium Ion Microscopy, NanoScience and Technology. Springer International Publishing, Cham. https://doi.org/10.1007/978-3-319-41990-9

Hlawacek, G., Veligura, V., van Gastel, R., Poelsema, B., 2014. Helium ion microscopy. J. Vac. Sci. Technol. B Nanotechnol. Microelectron. Mater. Process. Meas. Phenom. 32, 020801. https://doi.org/10.1116/1.4863676

Hou, C., Jiang, B., Liu, H., Song, Y., Xu, S., 2020. The differences of nanoscale mechanical properties among coal maceral groups. J. Nat. Gas Sci. Eng. 80, 103394. https://doi.org/10.1016/j.jngse.2020.103394

Hou, D., Li, M., Huang, Q., 2000. Marine transgressional events in the gigantic freshwater lake Songliao: paleontological and geochemical evidence. Org. Geochem. 31, 763–768. https://doi.org/10.1016/S0146-6380(00)00065-6

Hou, H., Wang, C., Zhang, J., Ma, F., Fu, W., Wang, P., Huang, Y., Zou, C., Gao, You-feng, Gao, Yuan, Zhang, L., Yang, J., Guo, R., 2018. Deep Continental Scientific Drilling Engineering Project in Songliao Basin: progress in Earth Science research. China Geol. 1, 173–186. https://doi.org/10.31035/cg2018036

Hu, W., Cai, C., Wu, Z., Li, J., 1998. Structural style and its relation to hydrocarbon exploration in the Songliao basin, northeast China. Mar. Pet. Geol. 15, 41–55. https://doi.org/10.1016/S0264-8172(97)00054-8

Huang, C., Ju, Y., Zhu, H., Lash, G.G., Qi, Y., Yu, K., Feng, H., Ju, L., Qiao, P., 2020. Investigation of formation and evolution of organic matter pores in marine shale by helium ion microscope: An example from the Lower Silurian Longmaxi Shale, South China. Mar. Pet. Geol. 120, 104550. https://doi.org/10.1016/j.marpetgeo.2020.104550

Huang, Y., 2018. Sedimentary characteristics of turbidite fan and its implication for hydrocarbon exploration in Lower Congo Basin. Pet. Res. 3, 189–196. https://doi.org/10.1016/j.ptlrs.2018.02.001

International Committee for Coal and Organic Petrology (ICCP), 2001. The new inertinite classification (ICCP System 1994). Fuel 80, 459–471. https://doi.org/10.1016/S0016-2361(00)00102-2

International Committee for Coal and Organic Petrology (ICCP), 1998. The new vitrinite classification (ICCP System 1994). Fuel 77, 349–358. https://doi.org/10.1016/S0016-2361(98)80024-0

Jankowski, B., 1983. Die Geschichte der Sedimentation im Nördlinger Ries und Randecker Maar, Bochumer geologische und geotechnische Arbeiten. Institut für Geologie der Ruhr-Univ.

Jankowski, B., Littke, R., 1986. Das organische Material der Ölschiefer von Messel. Org. Mater. Ölschiefer Von Messel 4, 73–80.

Jasper, K., Krooss, B.M., Flajs, G., Hartkopf-Fröder, Chr., Littke, R., 2009. Characteristics of type III kerogen in coal-bearing strata from the Pennsylvanian (Upper Carboniferous) in the Ruhr Basin, Western Germany: Comparison of coals, dispersed organic matter, kerogen concentrates and coal–mineral mixtures. Int. J. Coal Geol. 80, 1–19. https://doi.org/10.1016/j.coal.2009.07.003

Joens, M.S., Huynh, C., Kasuboski, J.M., Ferranti, D., Sigal, Y.J., Zeitvogel, F., Obst, M., Burkhardt, C.J., Curran, K.P., Chalasani, S.H., Stern, L.A., Goetze, B., Fitzpatrick, J.A.J., 2013. Helium Ion Microscopy (HIM) for the imaging of biological samples at sub-nanometer resolution. Sci. Rep. 3, 3514. https://doi.org/10.1038/srep03514

Kelly, S., El-Sobky, H., Torres-Verdín, C., Balhoff, M.T., 2016. Assessing the utility of FIB-SEM images for shale digital rock physics. Adv. Water Resour., Pore scale modeling and experiments 95, 302–316. https://doi.org/10.1016/j.advwatres.2015.06.010

Kelts, K., 1988. Environments of deposition of lacustrine petroleum source rocks: an introduction. Geol. Soc. Lond. Spec. Publ. 40, 3. https://doi.org/10.1144/GSL.SP.1988.040.01.02

Kennicutt, M. C., Defreitas, D. A., Joyce, J. E., Brooks, J. M., 1986. Nonvolatile organic-matter in sediments from site-614 to site-623, deep-sea-drilling-project Leg-96, Initial Rep. Deep Sea Drill. Proj., 96, 747–756. https://doi.org/10.2973/dsdp.proc.96.145.1986

Khatibi, S., Aghajanpour, A., Ostadhassan, M., Ghanbari, E., Amirian, E., Mohammed, R., 2018. Evaluating the Impact of Mechanical Properties of Kerogen on Hydraulic Fracturing of Organic Rich Formations, in: SPE Canada Unconventional Resources Conference. Presented at the SPE Canada Unconventional Resources Conference, Society of Petroleum Engineers, Calgary, Alberta, Canada. https://doi.org/10.2118/189799-MS

Khosrokhavar, R., Griffiths, S., Wolf, K.-H., 2014. Shale Gas Formations and Their Potential for Carbon Storage: Opportunities and Outlook. Environ. Process. 1, 595–611. https://doi.org/10.1007/s40710-014-0036-4

King, H.E., Eberle, A.P.R., Walters, C.C., Kliewer, C.E., Ertas, D., Huynh, C., 2015. Pore Architecture and Connectivity in Gas Shale. Energy Fuels 29, 1375–1390. https://doi.org/10.1021/ef502402e

Klaver, J., Desbois, G., Urai, J.L., Littke, R., 2012. BIB-SEM study of the pore space morphology in early mature Posidonia Shale from the Hils area, Germany. Int. J. Coal Geol. 103, 12–25. https://doi.org/10.1016/j.coal.2012.06.012

Kossovich, E.L., Borodich, F.M., Epshtein, S.A., Galanov, B.A., Minin, M.G., Prosina, V.A., 2019. Mechanical, structural and scaling properties of coals: depth-sensing indentation studies. Appl. Phys. A 125, 1–15. https://doi.org/10.1007/s00339-018-2282-1

Kumar, V., Sondergeld, C., Rai, C.S., 2015. Effect of mineralogy and organic matter on mechanical properties of shale. Interpretation 3, SV9–SV15. https://doi.org/10.1190/INT-2014-0238.1

Kunz, O., Wagner, W., 2012. The GERG-2008 Wide-Range Equation of State for Natural Gases and Other Mixtures: An Expansion of GERG-2004. J. Chem. Eng. Data 57, 3032–3091. https://doi.org/10.1021/je300655b

Kwiecińska, B., Pusz, S., Valentine, B.J., 2019. Application of electron microscopy TEM and SEM for analysis of coals, organic-rich shales and carbonaceous matter. Int. J. Coal Geol. 211, 103203. https://doi.org/10.1016/j.coal.2019.05.010

Langrock, U., Stein, R., 2004. Origin of marine petroleum source rocks from the Late Jurassic to Early Cretaceous Norwegian Greenland Seaway—evidence for stagnation and upwelling. Mar. Pet. Geol. 21, 157–176. https://doi.org/10.1016/j.marpetgeo.2003.11.011

Levenshtein, M.L., Lagutina, V.V., Kaminsky, V.V., 1991. Explanations to the Maps of Thicknesses and Structure of Middle Carboniferous Coal Seams in the Donetsk Coal Basin. Ministry of Geology of the USSR, Kiev. 100 pp.

Li, C., Ostadhassan, M., Abarghani, A., Fogden, A., Kong, L., 2019. Multi-scale evaluation of mechanical properties of the Bakken shale. J. Mater. Sci. 54, 2133–2151. https://doi.org/10.1007/s10853-018-2946-4

Li, W., Zhang, Z., Li, Y., 2015. Some aspects of excellent marine source rock formation: implications on enrichment regularity of organic matter in continental margin basins. Chin. J. Geochem. 34, 47–54. https://doi.org/10.1007/s11631-014-0018-2

Li, X., Fang, Z., 2014. Current status and technical challenges of CO2 storage in coal seams and enhanced coalbed methane recovery: an overview. Int. J. Coal Sci. Technol. 1, 93–102. https://doi.org/10.1007/s40789-014-0002-9

Littke, R., 1993. Deposition, Diagenesis and Weathering of Organic Matter-Rich Sediments, Lecture Notes in Earth Sciences. Springer-Verlag, Berlin Heidelberg. https://doi.org/10.1007/BFb0009988

Littke, R., Sachsenhofer, R.F., 1994. Organic Petrology of Deep Sea Sediments: A Compilation of Results from the Ocean Drilling Program and the Deep Sea Drilling Project. Energy Fuels 8, 1498–1512. https://doi.org/10.1021/ef00048a041

Littke, R., Zieger, L., 2020. Formation of Organic-Rich Sediments and Sedimentary Rocks, in: Wilkes, H. (Ed.), Hydrocarbons, Oils and Lipids: Diversity, Origin, Chemistry and Fate. Springer International Publishing, Cham, pp. 475–492. https://doi.org/10.1007/978-3-319-90569-3_14

Liu, B., Song, Y., Zhu, K., Su, P., Ye, X., Zhao, W., 2020. Mineralogy and element geochemistry of salinized lacustrine organic-rich shale in the Middle Permian Santanghu Basin: Implications for paleoenvironment, provenance, tectonic setting and shale oil potential. Mar. Pet. Geol. 120, 104569. https://doi.org/10.1016/j.marpetgeo.2020.104569

Liu, K., Ostadhassan, M., Bubach, B., Ling, K., Tokhmechi, B., Robert, D., 2018. Statistical grid nanoindentation analysis to estimate macro-mechanical properties of the Bakken Shale. J. Nat. Gas Sci. Eng. 53, 181–190. https://doi.org/10.1016/j.jngse.2018.03.005

Liu, S., Sang, S., Wang, G., Ma, J., Wang, X., Wang, W., Du, Y., Wang, T., 2017. FIB-SEM and X-ray CT characterization of interconnected pores in high-rank coal formed from regional metamorphism. J. Pet. Sci. Eng. 148, 21–31. https://doi.org/10.1016/j.petrol.2016.10.006

Löhr, S.C., Baruch, E.T., Hall, P.A., Kennedy, M.J., 2015. Is organic pore development in gas shales influenced by the primary porosity and structure of thermally immature organic matter? Org. Geochem. 87, 119–132. https://doi.org/10.1016/j.orggeochem.2015.07.010

Loucks, R.G., Reed, R.M., Ruppel, S.C., Jarvie, D.M., 2009. Morphology, Genesis, and Distribution of Nanometer-Scale Pores in Siliceous Mudstones of the Mississippian Barnett Shale. J. Sediment. Res. 79, 848–861. https://doi.org/10.2110/jsr.2009.092

Lünsdorf, N.K., 2016. Raman spectroscopy of dispersed vitrinite — Methodical aspects and correlation with reflectance. Int. J. Coal Geol. 153, 75–86. https://doi.org/10.1016/j.coal.2015.11.010

Lünsdorf, N.K., Lünsdorf, J.O., 2016. Evaluating Raman spectra of carbonaceous matter by automated, iterative curve-fitting. Int. J. Coal Geol. 160–161, 51–62. https://doi.org/10.1016/j.coal.2016.04.008

Luo, S., Lu, Y., Wu, Y., Song, J., DeGroot, D.J., Jin, Y., Zhang, G., 2020. Cross-scale characterization of the elasticity of shales: Statistical nanoindentation and data analytics. J. Mech. Phys. Solids 140, 103945. https://doi.org/10.1016/j.jmps.2020.103945

Lutugin, L. I., Stepanov, P. I.:1913. Donets Coal Basin, Geological Committee, Coal Minings in Russia, St. Petersburg, Russia, 112–143.

Ma, Z., Pathegama Gamage, R., Zhang, C., 2020. Application of nanoindentation technology in rocks: a review. Geomech. Geophys. Geo-Energy Geo-Resour. 6, 60. https://doi.org/10.1007/s40948-020-00178-6

Manjunath, G.L., Jha, B., 2019. Nanoscale fracture mechanics of Gondwana coal. Int. J. Coal Geol. 204, 102–112. https://doi.org/10.1016/j.coal.2019.02.007

Maystrenko, Y., Stovba, S., Stephenson, R., Bayer, U., Menyoli, E., Gajewski, D., Huebscher, C., Rabbel, W., Saintot, A., Starostenko, V., Thybo, H., Tolkunov, A., 2003. Crustal-scale pop-up structure in cratonic lithosphere: DOBRE deep seismic reflection study of the Donbas fold belt, Ukraine. Geology 31, 733–736. https://doi.org/10.1130/G19329.1

Metz, B., Davidson, O., de Coninck, H., Loos, M., Meyer, L., 2005. IPCC Special Report on Carbon dioxide Capture and Storage. Policy Stud

Misch, D., Gross, D., Huang, Q., Zaccarini, F., Sachsenhofer, R.F., 2016. Light and trace element composition of Carboniferous coals from the Donets Basin (Ukraine): an electronmicroprobe study. Int. J. Coal Geol. 168, 108–118. https://doi.org/10.1016/j.coal.2016.06.004

Misch, D., Klaver, J., Gross, D., Rustamov, J., Sachsenhofer, R.F., Schmatz, J., Urai, J.L., 2018. Pore space characteristics of the Upper Visean ‘Rudov Beds’: insights from broad ion beam scanning electron microscopy and organic geochemical investigations. Geol. Soc. Lond. Spec. Publ. 484, 205–228. https://doi.org/10.1144/SP484.9

Misch, D., Mendez-Martin, F., Hawranek, G., Onuk, P., Gross, D., Sachsenhofer, R.F., 2016b. SEM and FIB-SEM investigations on potential gas shales in the Dniepr-Donets Basin (Ukraine): pore space evolution in organic matter during thermal maturation. IOP Conf. Ser. Mater. Sci. Eng. 109, 012010. https://doi.org/10.1088/1757-899X/109/1/012010

Misch, D., Riedl, F., Liu, B., Horsfield, B., Ziegs, V., Mendez-Martin, F., Vranjes-Wessely, S., Sachsenhofer, R.F., 2019. Petrographic and sorption-based characterization of bituminous organic matter in the Mandal Formation, Central Graben (Norway). Int. J. Coal Geol. 211, 103229. https://doi.org/10.1016/j.coal.2019.103229

Neuzil, C.E., 2013. Can Shale Safely Host U.S. Nuclear Waste? Eos Trans. Am. Geophys. Union 94, 261–262. https://doi.org/10.1002/2013EO300001

Noah, M., Horsfield, B., Han, S., Wang, C., 2020. Precise maturity assessment over a broad dynamic range using polycyclic and heterocyclic aromatic compounds. Org. Geochem. 148, 104099. https://doi.org/10.1016/j.orggeochem.2020.104099

O’Brien, N.R., 1987. The Effects of Bioturbation on the Fabric of Shale. SEPM J. Sediment. Res. Vol. 57. https://doi.org/10.1306/212F8B5C-2B24-11D7-8648000102C1865D

Okolo, G.N., Everson, R.C., Neomagus, H.W.J.P., Roberts, M.J., Sakurovs, R., 2015. Comparing the porosity and surface areas of coal as measured by gas adsorption, mercury intrusion and SAXS techniques. Fuel 141, 293–304. https://doi.org/10.1016/j.fuel.2014.10.046

Oliver, W.C., Pharr, G.M., 2010. Nanoindentation in materials research: Past, present, and future. MRS Bull. 35, 897–907. https://doi.org/10.1557/mrs2010.717

Oliver, W.C., Pharr, G.M., 1992. An improved technique for determining hardness and elastic modulus using load and displacement sensing indentation experiments. J. Mater. Res. 7, 1564–1583. https://doi.org/10.1557/JMR.1992.1564

Omura, A., Ikedzu, D., Hoyanagi, K., 2000. An implication of depositional environments with reference to maceral compositions from the Pliocene and Pleistocene sediments in the Higashikubiki Hills, Niigata Prefecture, central Japan. J. Sedimentol. Soc. Jpn. 52, 43–52. https://doi.org/10.4096/jssj1995.52.43

Parrish, J.T., 1982. Upwelling and Petroleum Source Beds, With Reference to Paleozoic. AAPG Bull. 66, 750–774.

Parrish, J.T., 1987. Palaeo-upwelling and the distribution of organic-rich rocks. Geol. Soc. Lond. Spec. Publ. 26, 199–205. https://doi.org/10.1144/GSL.SP.1987.026.01.12

Pfeifenberger, M.J., Mangang, M., Wurster, S., Reiser, J., Hohenwarter, A., Pfleging, W., Kiener, D., Pippan, R., 2017. The use of femtosecond laser ablation as a novel tool for rapid micro-mechanical sample preparation. Mater. Des. 121, 109–118. https://doi.org/10.1016/j.matdes.2017.02.012

Pickel, W., Kus, J., Flores, D., Kalaitzidis, S., Christanis, K., Cardott, B.J., Misz-Kennan, M., Rodrigues, S., Hentschel, A., Hamor-Vido, M., Crosdale, P., Wagner, N., 2017. Classification of liptinite – ICCP System 1994. Int. J. Coal Geol. 169, 40–61. https://doi.org/10.1016/j.coal.2016.11.004

Popov, V.S., 1963. Tectonics of the Donets Basin (in Russian) In: Kuznetzov, I.A. (ed.), Geology of Coal and Oil Shale Deposits of the USSR, 1. Nedra, Moscow, 103–151.

Potgieter-Vermaak, S., Maledi, N., Wagner, N., Heerden, J.H.P.V., Grieken, R.V., Potgieter, J.H., 2011. Raman spectroscopy for the analysis of coal: a review. J. Raman Spectrosc. 42, 123–129. https://doi.org/10.1002/jrs.2636

Powell, T.G., 1986. Petroleum geochemistry and depositional setting of lacustrine source rocks. Mar. Pet. Geol. 3, 200–219. https://doi.org/10.1016/0264-8172(86)90045-0

Privalov, V.A., Panova, E.A., Sachsenhofer, R.F., Izart, A., Antsiferov, A.V., Antsiferov, V.A., 2007. Delineation of Gas Prospective Sites in the Donets Basin, Ukraine, in: 69th EAGE Conference and Exhibition Incorporating SPE EUROPEC 2007, European Association of Geoscientists & Engineers, London, UK,. https://doi.org/10.3997/2214-4609.201401846

Ramanampisoa, L., Radke, M., Schaeffer, R.G., Littke, R., Rullkötter, J., Horsfield, B., 1990. Organic-geochemical characterisation of sediments from the Sakoa coalfield, Madagascar. Org. Geochem. 16, 235–246. https://doi.org/10.1016/0146-6380(90)90044-Z

Rullkötter, J., Littke, R., Hagedom-Götz, I., and Jankowski, B.,1988. Vorläufige Ergebnisse derorganisch-geochemischen und organisch-petrographischen Untersuchungen an Kernproben des Messeler Olschiefers. In: Franzen, J.L. and Micbaelis, W. (eds): Der eozäne Messelsee – Eocene Lake Messel, Cour. Forsch-lnst. Senckenberg, 107, 37-52.

Rullkötter, J., Littke, R., Schaefer, R.G., 1990. Characterization of Organic Matter in Sulfur-Rich Lacustrine Sediments of Miocene Age (Nördlinger Ries, Southern Germany), in: Geochemistry of Sulfur in Fossil Fuels, ACS Symposium Series. American Chemical Society, pp. 149–169. https://doi.org/10.1021/bk-1990-0429.ch008

Sachsenhofer, R.F., Privalov, V.A., Izart, A., Elie, M., Kortensky, J., Panova, E.A., Sotirov, A., Zhykalyak, M.V., 2003. Petrography and geochemistry of Carboniferous coal seams in the Donets Basin (Ukraine): implications for paleoecology. Int. J. Coal Geol. 55, 225–259. https://doi.org/10.1016/S0166-5162(03)00112-5

Sachsenhofer, R.F., Privalov, V.A., Panova, E.A., 2012. Basin evolution and coal geology of the Donets Basin (Ukraine, Russia): An overview. Int. J. Coal Geol., European Coal Conference 2010 89, 26–40. https://doi.org/10.1016/j.coal.2011.05.002

Sassani, D.C., Stone, C.M., Hansen, F.D., Hardin, E.L., Dewers, T.A., Martinez, M.J., Rechard, R.P., Sobolik, S.R., Freeze, G.A., Cygan, R.T., Gaither, K.N., Holland, J.F., Brady, P.V., 2010. Shale disposal of U.S. high-level radioactive waste. (No. SAND2010-2843, 992338). https://doi.org/10.2172/992338

Sayers, C.M., 2013. The effect of kerogen on the elastic anisotropy of organic-rich shales. Geophysics 78, D65–D74. https://doi.org/10.1190/geo2012-0309.1

Scheidt, G., Littke, R., 1989. Comparative organic petrology of interlayered sandstones, siltstones, mudstones and coals in the Upper Carboniferous Ruhr basin, Northwest Germany, and their thermal history and methane generation. Geol. Rundsch. 78, 375–390. https://doi.org/10.1007/BF01988371

Scheihing, M.H., Pfefferkorn, H.W., 1984. The taphonomy of land plants in the orinoco delta: A model for the incorporation of plant parts in clastic sediments of late carboniferous age of euramerica. Rev. Palaeobot. Palynol. 41, 205–240. https://doi.org/10.1016/0034-6667(84)90047-2

Schultz, R.B., Coveney, R.M., 1992. Time-dependent changes for Midcontinent Pennsylvania black shales, U.S.A. Chem. Geol. 99, 83–100. https://doi.org/10.1016/0009-2541(92)90032-Z

Scipioni, L., Sanford, C.A., Notte, J., Thompson, B., McVey, S., 2009. Understanding imaging modes in the helium ion microscope. J. Vac. Sci. Technol. B Microelectron. Nanometer Struct. 27, 3250. https://doi.org/10.1116/1.3258634

Shabani, M., Moallemi, S.A., Krooss, B.M., Amann-Hildenbrand, A., Zamani-Pozveh, Z., Ghalavand, H., Littke, R., 2018. Methane sorption and storage characteristics of organic-rich carbonaceous rocks, Lurestan province, southwest Iran. Int. J. Coal Geol. 186, 51–64. https://doi.org/10.1016/j.coal.2017.12.005

Shukla, P., Kumar, V., Curtis, M., Sondergeld, C.H., Rai, C.S., 2013. Nanoindentation Studies on Shales. 47th US Rock Mechanics / Geomechanics Symposium 2013. 2. 1194–1203.

Shukla, P., Taneja, S., Sondergeld, C., Rai, C., 2015. Nanoindentation Measurements on Rocks, in: Carroll, J., Daly, S. (Eds.), Fracture, Fatigue, Failure, and Damage Evolution, Volume 5, Conference Proceedings of the Society for Experimental Mechanics Series. Springer International Publishing, Cham, pp. 99–105. https://doi.org/10.1007/978-3-319-06977-7_13

Simmons, M.D., Tari, G.C., Okay, A.I., 2018. Petroleum geology of the Black Sea: introduction. Geol. Soc. Lond. Spec. Publ. 464, 1–18. https://doi.org/10.1144/SP464.15

Smyth, M., 1989. Organic petrology and clastic depositional environments with special reference to Australian coal basins. Int. J. Coal Geol. 12, 635–656. https://doi.org/10.1016/0166-5162(89)90067-0

Song, Y., Hu, S., Xu, J., Shen, C., Li, S., Su, P., Xie, W., 2020. Lacustrine environmental evolution and implications on source rock deposition in the Upper Cretaceous-Paleocene of the South Yellow Sea Basin, offshore eastern China. Mar. Pet. Geol. 113, 104135. https://doi.org/10.1016/j.marpetgeo.2019.104135

Stach, E., Mackowsky, M.T., Teichmüller, M., Taylor, G.H., Chandra, D., Teichmüller, R., 1982. Stach's Textbook of Coal Petrology. Gebrüder Bornträger, Berlin - Stuttgart.535 pp.

Stephenson, R.A., Stovba, S.M., Starostenko, V.I., Stephenson, R., 2001. Pripyat-Dniepr-Donets Basin: implications for dynamics of rifting and the tectonic history of the northern Peri-Tethyan Platform. Peri-Tethys Mem. 6 Peri-Tethyan Rift. Basins Passive Margins 186, 369–406.

Stephenson, R.A., Yegorova, T., Brunet, M.-F., Stovba, S., Wilson, M., Starostenko, V., Saintot, A., Kusznir, N., 2006. Late Palaeozoic intra- and pericratonic basins on the East European Craton and its margins. Geol. Soc. Lond. Mem. 32, 463–479. https://doi.org/10.1144/GSL.MEM.2006.032.01.29

Stovba, S., Stephenson, R.A., Kivshik, M., 1996. Structural features and evolution of the Dniepr-Donets Basin, Ukraine, from regional seismic reflection profiles. Tectonophysics 268, 127–147. https://doi.org/10.1016/S0040-1951(96)00222-3

Stovba, S.M., Stephenson, R.A., 2002. Style and timing of salt tectonics in the Dniepr-Donets Basin (Ukraine): implications for triggering and driving mechanisms of salt movement in sedimentary basins. Mar. Pet. Geol. 19, 1169–1189. https://doi.org/10.1016/S0264-8172(03)00023-0

Stovba, S.M., Stephenson, R.A., 1999. The Donbas Foldbelt: its relationships with the uninverted Donets segment of the Dniepr–Donets Basin, Ukraine. Tectonophysics 313, 59–83. https://doi.org/10.1016/S0040-1951(99)00190-0

Taylor, G.H., Teichmüller, M., Davis, A., Diessel, C.F.K., Littke, R., Robert, P., 1998. Organic Petrology, Gebr. Borntraeger. Berlin, pp. 704.

Totman Parrish, J., Curtis, R.L., 1982. Atmospheric circulation, upwelling, and organic-rich rocks in the Mesozoic and Cenozoic eras. Palaeogeogr. Palaeoclimatol. Palaeoecol., Paleogeography and Climate 40, 31–66. https://doi.org/10.1016/0031-0182(82)90084-0

Tourtelot, H.A., 1979. Black Shale—Its Deposition and Diagenesis. Clays Clay Miner. 27, 313–321. https://doi.org/10.1346/CCMN.1979.0270501

Ulm, F.-J., Abousleiman, Y., 2006. The nanogranular nature of shale. Acta Geotech. 1, 77–88. https://doi.org/10.1007/s11440-006-0009-5

Vandenbroucke, M., Largeau, C., 2007. Kerogen origin, evolution and structure. Org. Geochem. 38, 719–833. https://doi.org/10.1016/j.orggeochem.2007.01.001

Vernik, L., Nur, A., 1992. Ultrasonic velocity and anisotropy of hydrocarbon source rocks. GEOPHYSICS 57, 727–735. https://doi.org/10.1190/1.1443286

Wang, P., Liu, H., Ren, Y., Wan, X., Wang, S., Qu, X., Meng, Q., Huang, Y., Huang, Q., Gao, Y., Wang, C., 2017. How to choose a right drilling site for the ICDP Cretaceous Continental Scientific Drilling in the Songliao Basin (SK2), Northeast China. Earth Sci. Front. 24, 216–228. https://doi.org/10.13745/j.esf.2017.01.014

Wang, P., Zhang, C., Li, X., Zhang, K., Yuan, Y., Zang, X., Cui, W., Liu, S., Jiang, Z., 2020. Organic matter pores structure and evolution in shales based on the he ion microscopy (HIM): A case study from the Triassic Yanchang, Lower Silurian Longmaxi and Lower Cambrian Niutitang shales in China. J. Nat. Gas Sci. Eng. 84, 103682. https://doi.org/10.1016/j.jngse.2020.103682

Ward, B.W., Notte, J.A., Economou, N.P., 2006. Helium ion microscope: A new tool for nanoscale microscopy and metrology. J. Vac. Sci. Technol. B Microelectron. Nanometer Struct. 24, 2871. https://doi.org/10.1116/1.2357967

Welte, D.H., 1969. Organic Matter in Sediments, in: Eglinton, G., Murphy, M.T.J. (Eds.), Organic Geochemistry: Methods and Results. Springer, Berlin, Heidelberg, pp. 262–264. https://doi.org/10.1007/978-3-642-87734-6_12

Wenger, L.M., Baker, D.R., 1986. Variations in organic geochemistry of anoxic-oxic black shale-carbonate sequences in the Pennsylvanian of the Midcontinent, U.S.A. Org. Geochem. 10, 85–92. https://doi.org/10.1016/0146-6380(86)90011-2

Wenger, L.M., Baker, D.R., Chung, H.M., McCulloh, T.H., 1988. Environmental control of carbon isotope variations in Pennsylvania black-shale sequences, Midcontinent, U.S.A. Org. Geochem., Proceedings of the 13th International Meeting on Organic Geochemistry 13, 765–771. https://doi.org/10.1016/0146-6380(88)90099-X

Williams, D.B., Carter, C.B., 2009. Transmission Electron Microscopy. Springer US, Boston, MA. https://doi.org/10.1007/978-0-387-76501-3

Wu, Y., Li, Y., Luo, S., Lu, M., Zhou, N., Wang, D., Zhang, G., 2020. Multiscale elastic anisotropy of a shale characterized by cross-scale big data nanoindentation. Int. J. Rock Mech. Min. Sci. 134, 104458. https://doi.org/10.1016/j.ijrmms.2020.104458

Xu, Z., Xu, Q., Liu, A., Wang, N., Li, G., Peng, C., Yan, L., Su, Y., 2020. The Cretaceous stratigraphy, Songliao Basin, Northeast China: Constrains from drillings and geophysics. Open Geosci. 12, 1212–1223. https://doi.org/10.1515/geo-2020-0188

Yang, C., Xiong, Y., Wang, J., Li, Y., Jiang, W., 2020. Mechanical characterization of shale matrix minerals using phase-positioned nanoindentation and nano-dynamic mechanical analysis. Int. J. Coal Geol. 229, 103571. https://doi.org/10.1016/j.coal.2020.103571

Yu, H., Zhang, Y., Lebedev, M., Han, T., Verrall, M., Wang, Z., Al-Khdheeawi, E., Al-Yaseri, A., Iglauer, S., 2018. Nanoscale geomechanical properties of Western Australian coal. J. Pet. Sci. Eng. 162, 736–746. https://doi.org/10.1016/j.petrol.2017.11.001

Zhao, J., Zhang, W., Zhang, D., Wei, R., Wang, Y., 2020. Influence of Geochemical Features on the Mechanical Properties of Organic Matter in Shale. J. Geophys. Res. Solid Earth 125. https://doi.org/10.1029/2020JB019809

Zhao, Y., Sun, Y., Liu, S., Chen, Z., Yuan, L., 2018. Pore structure characterization of coal by synchrotron radiation nano-CT. Fuel 215, 102–110. https://doi.org/10.1016/j.fuel.2017.11.014

Journal publications

8 Publication I

Nanoindentation study of macerals in coals from the Ukrainian Donets Basin

Vranjes, S.[1,2], Misch, D.[1], Schöberl, T.[3], Kiener, D.[2], Gross, D.[1], Sachsenhofer, R.F.[1]

Adv. Geosci., 45, 73–83, 2018

1)Department Applied Geosciences and Geophysics, Montanuniversität Leoben, A-8700 Leoben, Austria
2)Department Materials Science, Montanuniversität Leoben, A-8700 Leoben, Austria
3)Erich Schmid Institute of Materials Science, Austrian Academy of Sciences, A-8700 Leoben, Austria

Abstract

This article discusses the mechanical properties of macerals in Carboniferous coals from the Ukrainian Donets Basin, covering a maturity range from 0.62 to 1.47 %Rr (vitrinite reflectance). The inherent inhomogeneity of geological samples requires characterization at the micro-/nanoscale, and hence material parameters, such as hardness H and reduced elastic modulus E_r were obtained from twelve coal specimens via nanoindentation tests. Different material properties and maturity trends were acquired for the individual maceral groups (vitrinite, inertinite, liptinite). The results indicate that apart from maturity, multiple factors like microstructural features and depositional environment control the mechanical properties of macerals in coals. H and E_r of vitrinites show a complex relationship with maturity due to additional influence of microstructural features such as nanoporosity or mineral inclusions and complex changes in the organic matter structure with increasing rank. The mechanical behaviour of inertinites is mainly controlled by the prevailing conditions (temperature, exposure) during paleo-wildfires. E_r and H of liptinites are strongly influenced by transformational processes related to devolatilization at low to medium rank, as well as later hydrocarbon generation. Variations in the depositional environment (e.g. increased organic S content due to marine influence) might play an additional role.

8.1 Introduction

Coal is still of particular importance as a natural resource today and remains one of the most important energy sources for the production of electricity or in various metallurgical processes. Moreover, it is considered a substantial source for methane which not only represents a mining hazard but can also be utilized by modern unconventional production techniques (e.g. coal bed methane; CBM). However, the producibility of coal bed methane depends on mechanical properties and fracture behaviour of the hosting coals. Coals are constituted by distinct organic components referred to as macerals (vitrinite, liptinite, inertinite), and obtaining the mechanical properties of individual maceral particles is challenging due to their usually small size (often micro-scaled). Nevertheless, knowledge of maceral-specific properties is critical for the understanding of controlling factors on the overall mechanical properties of a certain coal sample. Borodich et al. (2015) and Epshtein et al. (2015) proved the suitability of nanoindentation for the determination of mechanical properties of individual coal macerals. The great advantage of nanoindentation compared to other indentation testing approaches is the small required testing volume which allows analyses of material parameters like hardness (H) and reduced elastic modulus (E_r) in areas that are considered highly inhomogeneous at the micro-scale (Oliver and Pharr, 1992).

In an attempt to determine material parameters of individual macerals and to study maturity-related changes, nanoindentation tests were carried out on twelve Carboniferous coal samples from the Ukrainian Donets Basin (Fig.1). The Donets Basin hosts one of the most important coal fields worldwide and extends over an area of 60 000 km^2 (Sachsenhofer et al., 2012). The selected coals cover a broad maturity interval of 0.62–1.47 %Rr (vitrinite reflectance) and were intensively investigated regarding their depositional environment, paleoecology, geochemistry and petrography during previous studies (e.g. Stovba and Stephenson, 1999; Stephenson et al., 2001; Sachsenhofer et al., 2003; Izart et al., 2006; Misch et al., 2016). Hence, they offer a perfect opportunity to evaluate multiple influencing factors on coal stability and to develop a nanoindentation testing routine for inhomogeneous, organic matter-rich samples.

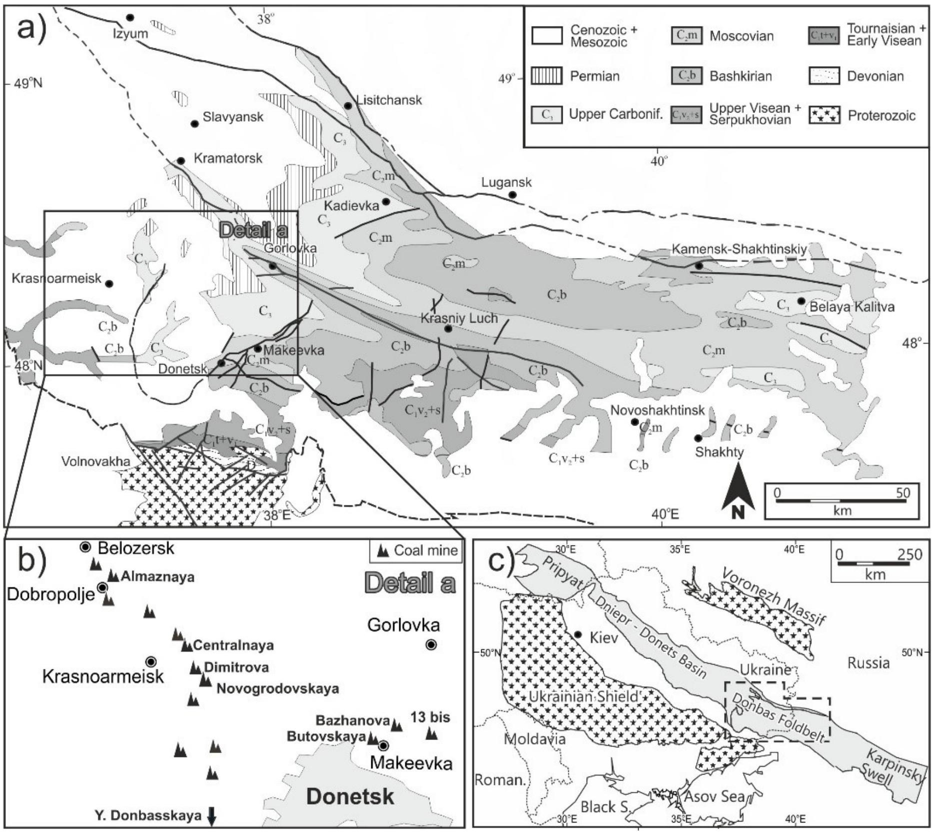

Figure 1. (a) Geological map of the Donets Basin (after Sachsenhofer et al., 2003). (b) Detail map showing an overview of the sampled coal mines. Locations of samples investigated during this study are marked in bold. (c) Regional overview of the Donets Basin in Europe.

8.2 Geological Setting

The Donets Basin (Fig. 1) is a Late Devonian rift structure and forms the south-eastern part of the Pripyat–Dniepr–Donets–Karpinsky Basin located within the eastern European craton (Stovba and Stephenson, 1999; Stephenson et al., 2001). A detailed chrono- and lithostratigraphic overview of the Donets Basin is given in Sachsenhofer et al. (2003) and Misch et al. (2016). Devonian pre- and syn-rift rocks with a thickness of 750 m form the margin of the basin, which reaches depths up to 5 km at its centre. The basement consists of Precambrian crystalline rocks of the eastern European craton, which are overlain by middle Devonian to Carboniferous rocks (Chekunov et al., 1993; Maystrenko et al., 2003). The Carboniferous succession is up to 14 km thick and subdivided into lithostratigraphic units named suites A, B, C, to P (Lutugin and Stepanov, 1913; Fig. 2). The coal-bearing sequence is formed by fluvial sandstone, marine limestone or mudstone, and deltaic mudstone and siltstone (Sachsenhofer et al., 2003). Marine deposits are more common in the eastern than in the western part of the basin. In general, coal seams and intercalations of coal exist throughout the Carboniferous succession. The lower Serpukhovian (suite C) and Moscovian successions (suites K to M) are particularly rich in coal (Levenshtein et al., 1991; see Fig. 2). Serpukhovian coal seams are concentrated in a narrow NW-SE trending zone along the southwestern basin margin (Shulga, 1981; Fig. 1) where accumulation occurred during a regressive–transgressive cycle in a roughly 10 km wide shore-zone dissected by several NE trending rivers discharging into a nearby shallow sea in the central Donets Basin (Sachsenhofer et al., 2012). The high amounts of inertinite and liptinite, as well as usually very low ash yields and low to moderate sulphur contents are characteristic for Serpukhovian coals (Sachsenhofer et al., 2003). In contrast, Moscovian seams are generally rich in vitrinite macerals and show high ash yields and variable sulphur contents, related to changing depositional systems with varying marine influence (Sachsenhofer et al., 2003).

The Carboniferous succession in the Donets Basin is of great economic importance; it hosts about 130 economic coal seams, each with a thickness between 0.45 and 2.5 m, summing up to a total net thickness of about 60 m (Ritenberg, 1972). Most coal fields of the Donets Basin contain high amounts of methane (from 8–10 to 25–37 m3 t−1; Sachsenhofer et al., 2003), which, apart from mine safety issues, constitute a high inherent potential for coal bed methane production (Privalov et al., 2007).

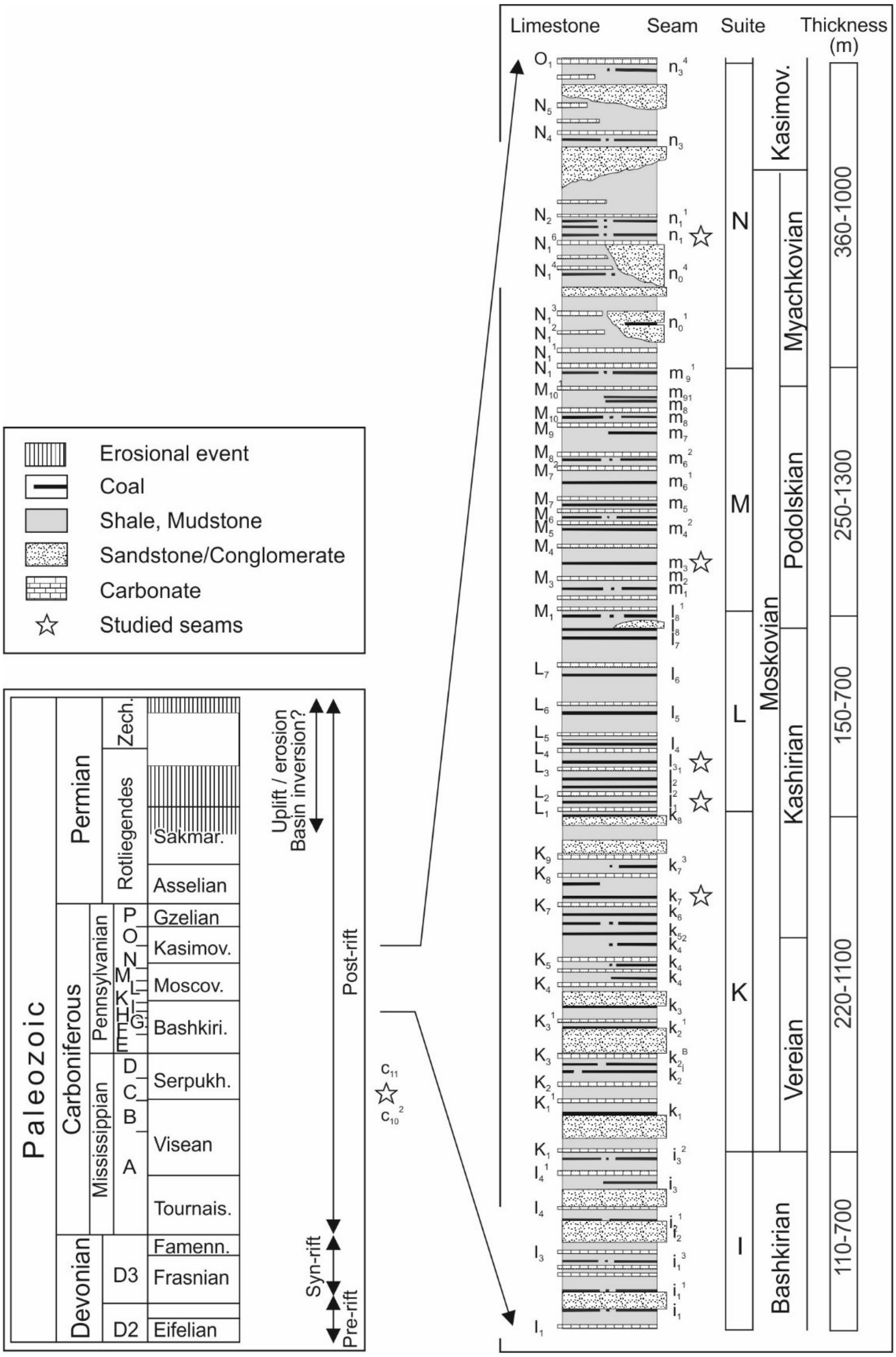

Figure 2. Chrono- and lithostratigraphy of the Donets Basin. Considerable magmatic and tectonic events are shown (Stovba and Stephenson, 1999). For the Moscovian sequence a detailed stratigraphic column is given (after Sachsenhofer et al., 2003, 2012). The studied seams are marked with star symbols.

8.3 Experimental

8.3.1 Coal Samples

The investigated coal samples were collected from well-studied seam profiles in the (south-)western part of the Donets Basin (Table 1; sampling locations are shown in Fig. 1, for stratigraphic assignment see Fig. 2). Twelve coal samples from Moscovian (11) and Serpukhovian (1) seams were selected based on their vitrinite reflectance (VR) obtained by Sachsenhofer et al. (2003). The selected coals cover a maturity range from 0.62 to 1.47 %Rr (Table 1). The coal specimen were embedded in epoxy resin and prepared as polished sections (final polishing steps with 9, 3, 1 µm diamond polishing suspension and 0.05 µm micropolish powder). Individual macerals were identified in an optical microscope under white reflected light (no oil immersion), and color-marked to ensure the correct identification during the nanoindentation procedure. No oil immersion was used to enable color-marking.

Table 1. List of samples including information on stratigraphic assignment, measured vitrinite reflectance (VR) and indented maceral groups (v = Vitrinite; i = Inertinite; l = Liptinite).

Sample	Mine	Stratigraphy	VR [%Rr]	Indented
n1_2	Butovskaya	Moscovian	0.83	v, i, l
m3_4	Bazhanova	Moscovian	1.10	v, i
m3_5	Bazhanova	Moscovian	1.21	v
m3_8	Bazhanova	Moscovian	1.23	v
l3_11	Almaznaya	Moscovian	0.87	l
l1_2	Dimitrova	Moscovian	0.76	v
l1_4	Dimitrova	Moscovian	0.76	v, l
l1_9	Dimitrova	Moscovian	0.71	v, l
l1_4	Novogrodovskaya	Moscovian	0.69	v, l
l1_2	13_bis	Moscovian	1.47	v
k7_3	Centralnaya	Moscovian	0.93	v, l
c10_2	Yuzho-Donbasskaya	Serpukhovian	0.62	v, i, l

8.3.2 Nanoindentation

The nanoindentation tests were performed using a Hysitron (now Bruker) Triboscope system with the transducer being mounted on the scanner head of a Digital Instruments (now Bruker) D3100 atomic force microscope, allowing for surface scans. A Cube Corner diamond tip with a tip radius of approximately 200 nm was used as indenter. Surface scans generated with the Cube Corner tip provided sufficient information to identify suitably flat areas without scratches or other disturbing topography features that might influence the obtained material parameters. The area function of the Cube Corner was calibrated using a fused silica standard following the Oliver-Pharr method (1992). All indentation tests were performed in load control mode with a trapezoidal loading profile to a maximum load of 1000 μN held for 10 s and loading/unloading rates of 500 μN s^{-1}. To reduce the influence of thermal instrumental drift, fast loading and unloading sequences were selected, while the holding time of 10 s at maximum load was chosen to minimize the influence of creep during unloading (Fig. 3). To exclude surface effects or other measurement bias (e.g. due to unintentional indentation of mineral grains embedded in organic matter), all results were quality-checked based on the obtained load-displacement curves that can be regarded as material-characteristic finger prints. Hardness (H) and reduced elastic modulus (E_r) were determined using the method proposed by Oliver and Pharr (1992). H is defined as the resistance of a material against external force. It is calculated following Eq. (1):

$$H = \frac{P_{max}}{A} \tag{1}$$

where P_{max} is the maximum load applied on the projected contact area (A) between indenter and material. A is calculated from the tip area function and the indentation depth (h) into the sample surface at maximal load. E_r is obtained by evaluation of the load-displacement curves according to Eq. (2). Therein, the contact stiffness S describes the slope of a tangent that is fitted to the elastic unloading curve segment.

$$E_r = \frac{\sqrt{\pi}}{2} \frac{S}{\sqrt{A}} \tag{2}$$

During the indentation procedure the diamond tip is also elastically deformed, as it is not entirely rigid. This effect is considered trough Eq. (3):

$$\frac{1}{E_r} = \frac{1-\nu^2}{E} + \frac{1-\nu_i^2}{E_i} \tag{3}$$

where E is the Young's modulus of the sample and ν denominates its Poisson's ratio. E_i and ν_i are the known material properties of the indenter tip. However, for soft materials E and E_r are almost equal, as the deformation of the indenter tip can be neglected in this case. Therefore, and because the Poisson's ratios of macerals are not known, this study utilizes E_r as material parameter.

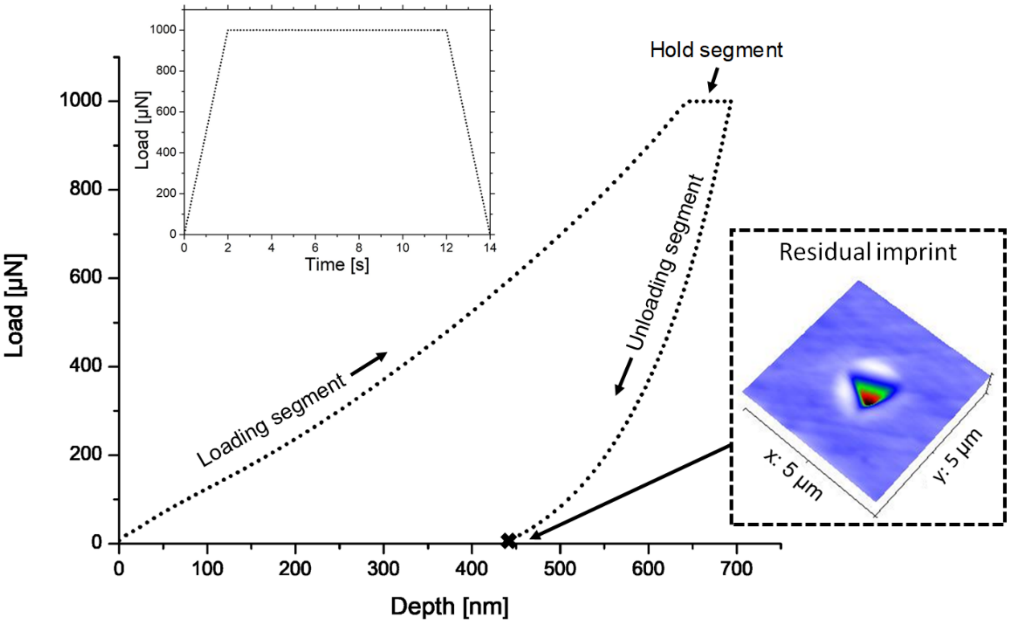

Figure 3. Example of a load-displacement curve, its trapezoidal loading profile and a 3-D-view of the resulting indent.

8.3.3 Inertinite reflectance measurements

Three coal samples with different ranks (Table 1) were selected for inertinite reflectance measurements. The measurement of random inertinite reflectance in oil (IR) was performed using a magnification of 100× in non-polarized light at a wavelength of 546 nm (Taylor et al., 1998). Inertinite reflectance measurements were compared to nanoindentation results to investigate the relationship between IR, H and E_r for various inertinite sub-macerals.

8.4 Results

8.4.1 Vitrinite

The indentation results indicate that the obtained average H and E_r values of vitrinites do not follow a clear maturity trend (Fig. 4; Table 2). The lowest H and E_r averages are observed in the low rank coals (0.62 %Rr), with values of 0.43 ± 0.03 and 4.91 ± 0.37 GPa, respectively. Both parameters vary considerably at 0.62 %Rr. Medium rank coals (0.69–0.76 %Rr) show the highest H and E_r averages. The obtained average H and E_r values at 1.47 %Rr are 0.48 ± 0.01 and 5.06 ± 0.2 GPa, respectively, and hence comparatively lower compared to samples of medium rank. Generally, vitrinites show elasto-plastic behavior at all maturity levels (Fig. 5).

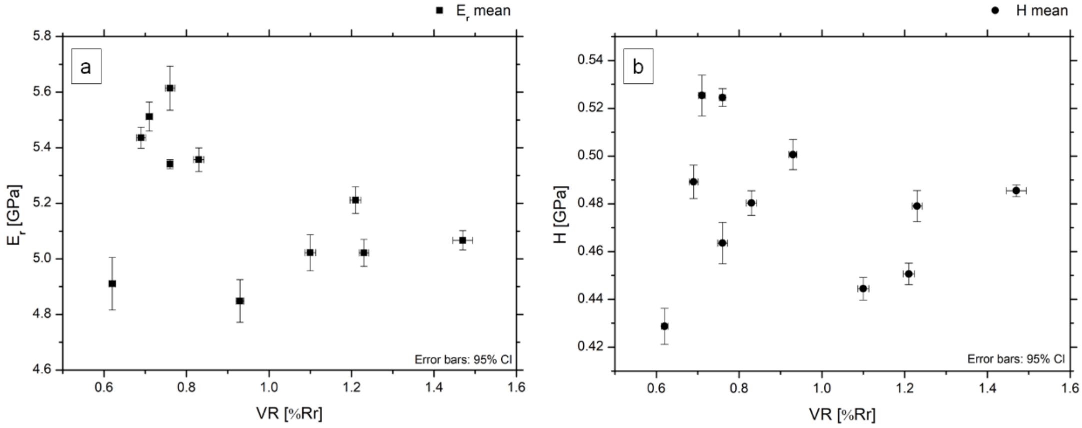

Figure 4. E_r (a) and H (b) obtained for vitrinites from 11 samples with varying maturity (0.62 to 1.47 %Rr). (CI = Confidence interval).

Table 2. Obtained *H* and E_r averages for vitrinite, including standard deviations (SD) calculated from the respective number of measurements (*n*).

Sample	Mine	VR [%Rr]	E_r [GPa]	SD [GPa]	*H* [GPa]	SD [GPa]	*n*
n1_2	Butovskaya	0.83	5.36	0.13	0.48	0.02	36
m3_4	Bazhanova	1.10	5.02	0.23	0.44	0.02	52
m3_5	Bazhanova	1.21	5.21	0.13	0.45	0.01	30
m3_8	Bazhanova	1.23	5.02	0.13	0.48	0.02	30
l1_2	Dimitrova	0.76	5.34	0.05	0.52	0.01	34
l1_4	Dimitrova	0.76	5.61	0.19	0.46	0.02	25
l1_9	Dimitrova	0.71	5.51	0.14	0.53	0.02	30
l1_4	Novogrodovskaya	0.69	5.44	0.09	0.49	0.02	26
l1_2	13_bis	1.47	5.07	0.2	0.49	0.01	34
k7_3	Centralnaya	0.93	4.85	0.27	0.5	0.02	48
c10_2	Yuzho-Donbasskaya	0.62	4.91	0.37	0.43	0.03	62

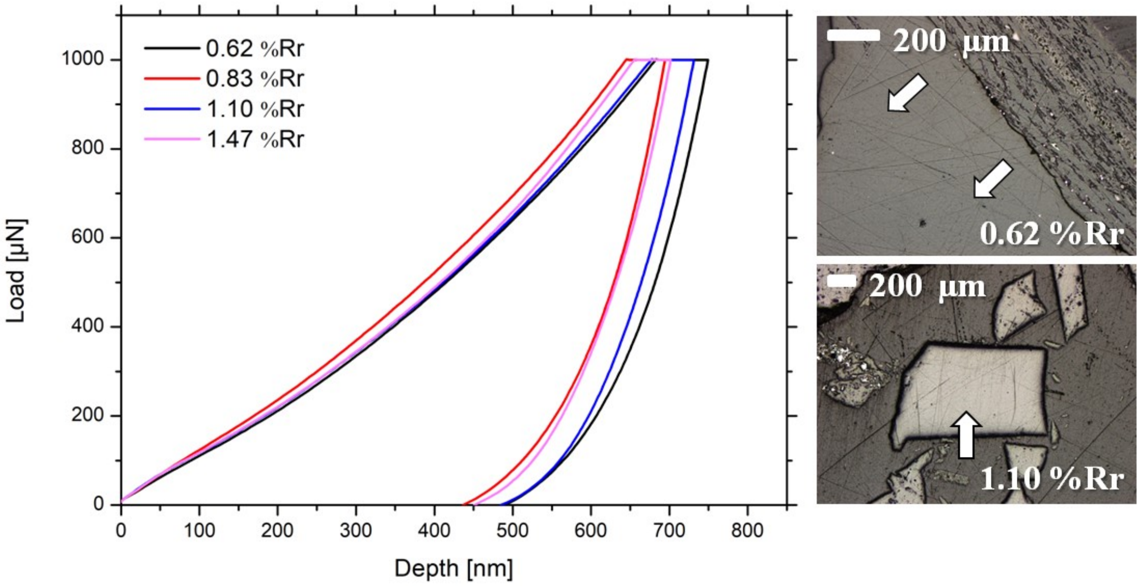

Figure 5. Averaged load-displacement curves for vitrinites at different coal rank. Slightly differing deformation behaviour is indicated by the individual curve shapes. However, a general elasto-plastic behaviour dominates at all maturity ranges. The insets show micrographs of typical indentation spots.

8.4.2 Inertinite

H and E_r values obtained from inertinites do not follow a maturity trend (Table 3). However, a linear correlation between the obtained material parameters and measured inertinite reflectance (1.67–3.76 %Rr) is observed (Fig. 6). IR is mainly dependent on the investigated sub-maceral type. Semifusinite shows the lowest reflectance values, while macrinite shows intermediate reflectance. Inertodetrinite and pyrofusinite exhibit the highest reflectance values. Variable shapes of the load-displacement curves illustrate that the deformation behaviour changes from elasto-plastic to mainly elastic with increasing IR (Fig. 7).

Table 3. Table 3. H and E_r averages determined for various inertinite sub-macerals, including standard deviations (SD) calculated from the respective number of measurements (n). Vitrinite reflectance (VR), indicative for the thermal maturity of the whole coal sample, was adopted from Sachsenhofer et al. (2003). Inertinite reflectance values (IR) of investigated inertinite macerals were measured during this study and reflect the conditions during pre-depositional wildfires, rather than thermal maturity related to burial. Note that inertinite reflectance refers to the actually indented macerals.

Sample	Mine	VR [%Rr]	Sub-maceral	IR [%Rr]	E_r [GPa]	SD [GPa]	H [GPa]	SD [GPa]	n
n1_2	Butovskaya	0.83	Inertodetrinite	3.13	14.55	0.21	3.84	0.18	4
m3_4	Bazhanova	1.10	Semifusinite	1.86	7.81	0.3	1.64	0.06	7
m3_4	Bazhanova	1.10	Inertodetrinite	3.04	11.95	0.56	3.29	0.15	6
m3_4	Bazhanova	1.10	Makrinite	1.70	6.68	0.54	1.19	0.21	9
m3_4	Bazhanova	1.10	Semifusinite	1.70	5.55	0.07	0.84	0.02	5
c10_2	Yuzho-Donbasskaya	0.62	Semifusinite	1.90	7.15	0.08	1.94	0.09	5
c10_2	Yuzho-Donbasskaya	0.62	Makrinite	1.69	5.46	0.05	0.92	0.06	9
c10_2	Yuzho-Donbasskaya	0.62	Pyrofusinite	3.74	20.03	0.08	4.83	0.15	4
c10_2	Yuzho-Donbasskaya	0.62	Pyrofusinite	2.44	9.31	0.64	2.86	0.2	7
c10_2	Yuzho-Donbasskaya	0.62	Semifusinite	1.67	6.96	0.21	1.60	0.08	5

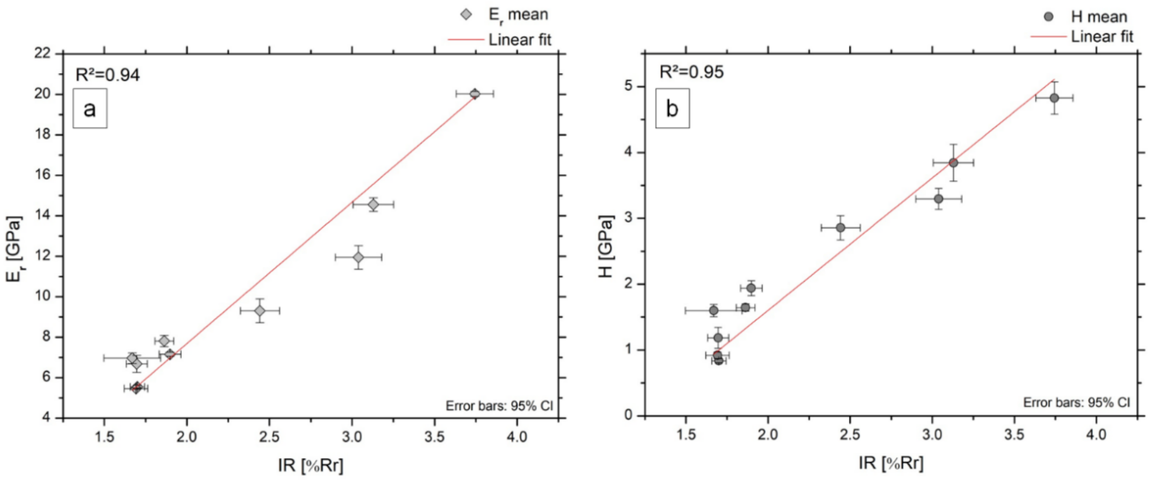

Figure 6. E_r (a) and H (b) obtained for inertinites with varying IR (inertinite reflectance). (CI = Confidence interval).

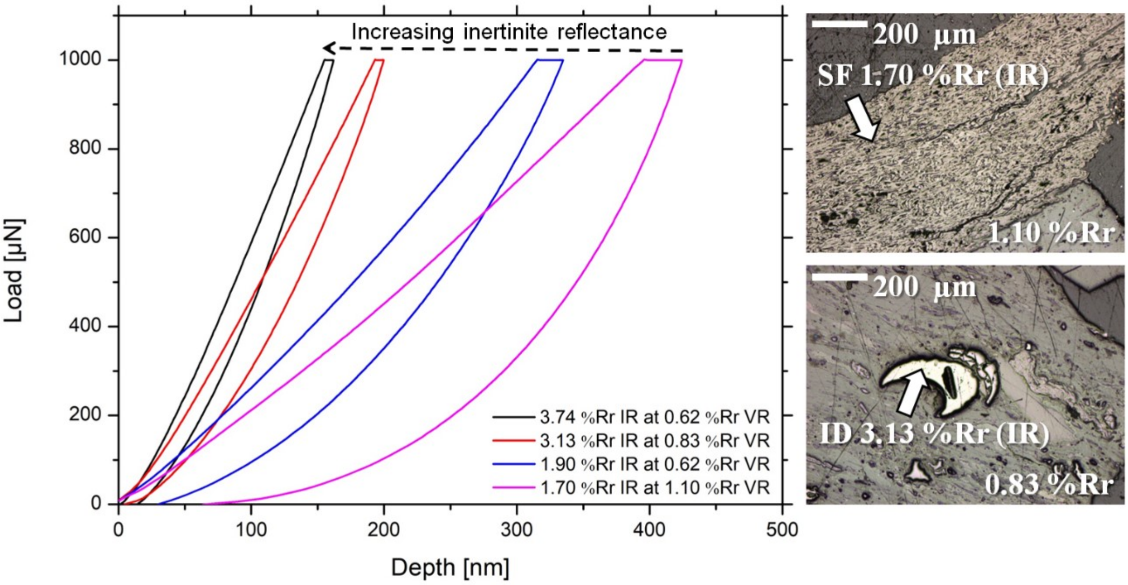

Figure 7. Averaged load-displacement curves for inertinites at different coal ranks. The deformation behaviour changes rapidly with increasing IR, as indicated by the dashed arrow. Insets show different investigated inertinite sub-macerals (SF = semifusinite; ID = inertodetrinite).

8.4.3 Liptinite

Sporinite is the most abundant liptinite maceral in the selected coals and hence indentation tests were mainly conducted on sporinites. The lowest value for H was determined for the least mature sample (0.62 %Rr), whereas the highest values for both H and E_r occur at 0.71 %Rr. After the peak, a decrease in the values of E_r and (to a lesser degree) H is observed. E_r and H averages at 0.83 and 0.92 %Rr are comparably low (Table 4; Fig. 8). At 0.93 %Rr, the obtained E_r and (to a lesser degree) H values show a multimodal frequency distribution (Fig. 9). The material behavior of liptinites can be described as elasto-plastic with dominance of the plastic deformation part at all maturity-levels (Fig. 10). Load-displacement curves of liptinites exhibit the largest amount of energy dissipation and highest indentation depths of all maceral groups.

Table 4. H and E_r averages obtained from sporinites, including standard deviations (SD) calculated from the respective number of measurements (n).

Sample	Mine	VR [%Rr]	E_r [GPa]	SD [GPa]	H [GPa]	SD [GPa]	n
n1_2	Butovskaya	0.83	6.09	0.27	0.39	0.02	18
l3_11	Almaznaya	0.87	4.39	0.34	0.41	0.03	25
l1_4	Dimitrova	0.76	6.25	0.43	0.42	0.02	36
l1_9	Dimitrova	0.71	6.31	0.29	0.43	0.02	27
l1_4	Novogrodovskaya	0.69	4.28	0.14	0.38	0.01	25
k7_3	Centralnaya	0.93	3.69	0.30	0.38	0.03	41
c10_2	Yuzho-Donbasskaya	0.62	5.73	0.70	0.35	0.05	45

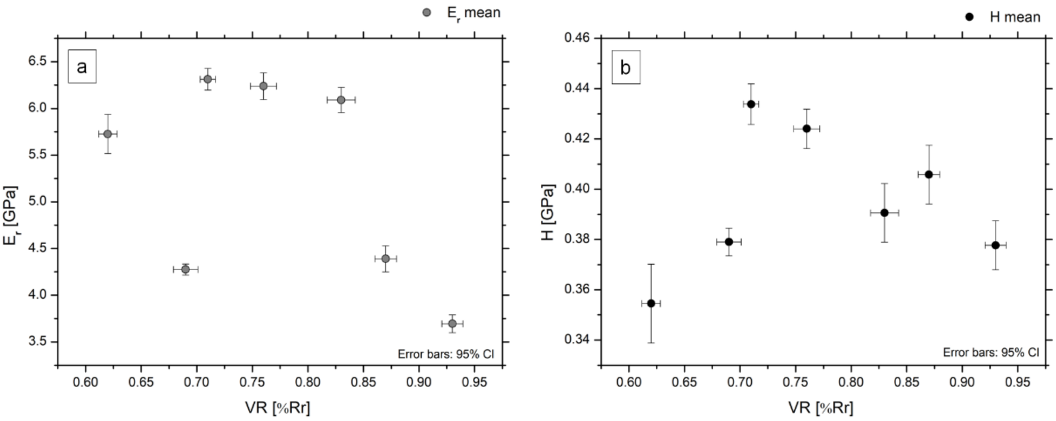

Figure 8. E_r (a) and H (b) obtained for sporinites at varying maturity (0.62 to 0.93 %Rr). (CI = Confidence interval).

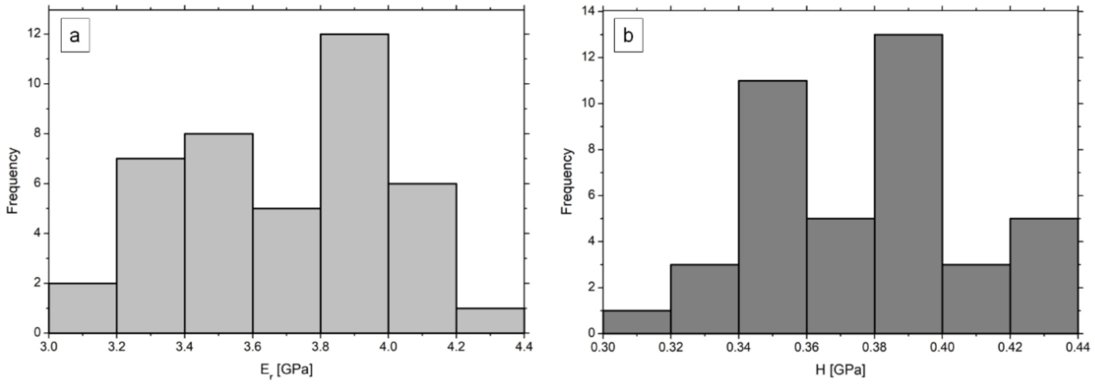

Figure 9. The frequency distribution of the obtained E_r (a) and H (b) values at 0.93 %Rr.

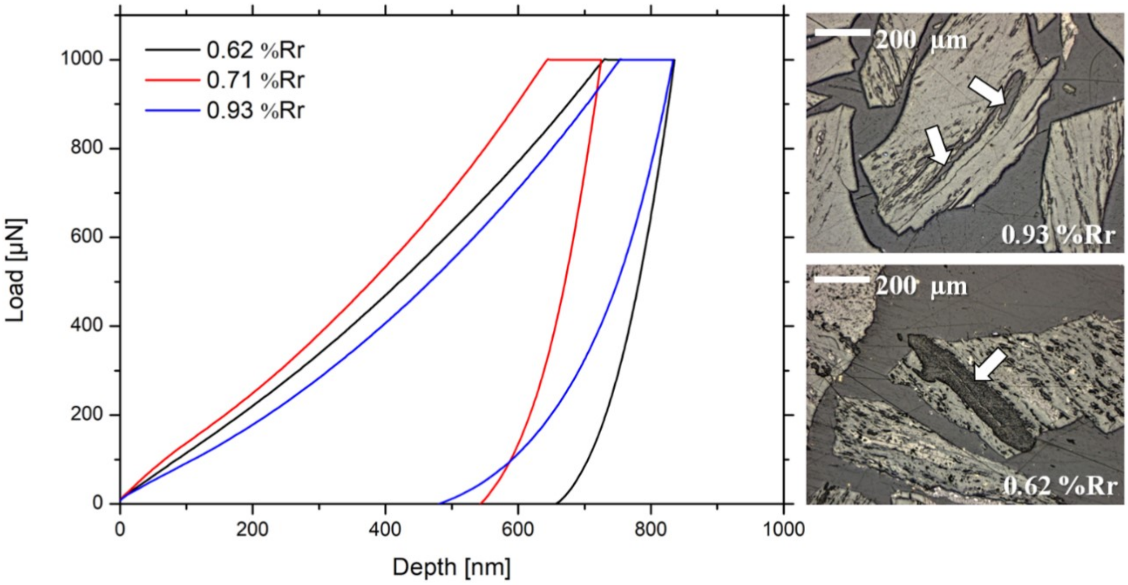

Figure 10. Averaged load-displacement curves for sporinites at different coal ranks. The insets show micrographs of sporinites at low-medium (0.62 %Rr) and high rank (0.93 %Rr).

8.5 Discussion

8.5.1 Vitrinite

In general, the coalification process of vitrinites at the bituminous rank is characterized by various changing parameters, including loss of hydrogen- and oxygen-bearing functional groups and volatile matter, increasing aromaticity, decreasing primary porosity and increasing density, which leads to generally increasing organic carbon contents and increased homogenization (e.g. Taylor et al., 1998; Tissot and Welte, 1984). However, the density of vitrinites does not change linearly with ongoing thermal maturation. At the boundary between sub-bituminous to bituminous coal rank, the true density decreases with rank as a result of the devolatilization of mainly heavy oxygen-rich compounds. The density increases again at advanced maturity because hydrogen-rich components are transformed during hydrocarbon generation and the increase of aromatic units leads to a tighter packing of the polymer structure (Taylor et al., 1998; Van Krevelen, 1961). Nevertheless, it might decrease again due to the generation of secondary (nano-)porosity. The mechanical properties of vitrinite macerals investigated during this study reflect the complex effects described above, rather than a linear maturity trend (Fig. 4a, b). Samples at low to medium rank show largely varying mechanical properties, whereas less scattering results at advanced maturity (>1.0 %Rr) point to increasing homogeneity of the organic matter structure at this stage, reflected also by a more uniform geochemical composition (e.g. Misch et al., 2016). Apart from maturation-related processes such as devolatilization (decreases primary porosity) and hydrocarbon generation (increases secondary porosity), changing mineral matter contents, best approximated by the ash yield, might affect porosity and relative density of vitrinites especially at an early mature stage. The obtained E_r and (to a lesser degree) H values correlate with ash yields (Fig. 11a, b; ash yield data from Sachsenhofer et al., 2003) at low to medium rank. Hence, the depositional setting can be considered an equally important influencing factor for the mechanical properties of vitrinites at this maturity stage.

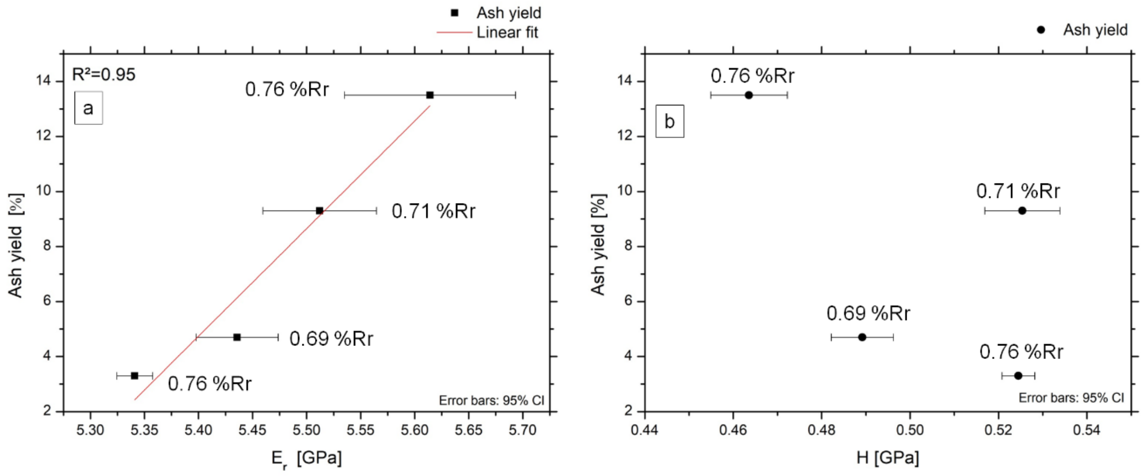

Figure 11. Correlation between ash yield (data from Sachsenhofer et al., 2003), E_r (a) and H (b) of vitrinite macerals. Note that samples of equal maturity (and hence chemical composition) are displayed for comparison. (CI = Confidence interval).

8.5.2 Inertinite

The highest average values for *H* and E_r were obtained from inertinites. Apparently, the mechanical properties of inertinites are not primarily controlled by the coal rank but correlate well with the measured inertinite reflectance. Reflectance studies of recent wildfire charcoals and experimental pyrolysis studies on charcoalified wood prove that inertinite reflectance increases with burning temperature, regardless of its morphology (Scott and Glasspool, 2007). A wildfire might produce a spectrum of different temperatures up to 1000 °C depending on the grade of exposition (Pyne et al., 1996). Zickler et al. (2006) studied the influence of artificial pyrolysis treatments on the mechanical properties of wood cells via nanoindendation. Between 500 and 900 °C they described a continuous rise of E_r. A continuous increase could also be observed in *H* at the pyrolysis temperature between 220 and 700 °C. Furthermore, a transition from elasto-plastic to mainly elastic material behaviour with rising temperature according to the load-displacement curves was described by the authors. These findings are reflected by the clear correlation of mechanical properties and deformation behaviour with the measured inertinite reflectance of the investigated samples. Zickler et al. (2006) interpreted this trend as an increase of covalent carbon-bonding and a glass-like structure characterized by randomly cross-linked aromatic carbon sheets. Hence, the main controlling factor for the material behaviour of inertinite is the temperature exposure during paleo-wildfire events.

8.5.3 Liptinite

The indentation results of liptinites indicate a non-linear relationship with maturity. Both *H* and E_r of sporinites increase with maturity from low to medium rank (up to ~0.7 %Rr; Fig. 8a, b). The sample at 0.71 %Rr exhibits a maximum of both parameters, likely related to progressing organization, dehydration and decarboxylation processes of the biopolymers, predominantly occurring at low to medium rank. A gradual decrease of both E_r and *H* occurs from 0.76 to 0.83 %Rr, and the lowest E_r value occurs at 0.93 %Rr (Fig. 8a). The sharp decrease in measured reduced elastic moduli might indicate the onset of thermal cracking related to hydrocarbon generation, associated with the loss of aliphatic chains and the formation of isolated aromatic rings (Yule et al., 2000). The multimodal distribution of measured E_r and *H* (Fig. 9a, b) values points to an anisotropic behaviour that is caused by structural reorganisation and polymerisation of the aromatic units that leads to the formation of sheets (Yule et al., 2000). The outlier of E_r at 0.69 %Rr is likely caused by changes in the depositional environment, as Misch et al. (2016) reported elevated organic S contents at the expense of C, related to an increased marine/brackish influence on the Novogrodovskaya seam during peat formation that agrees with findings from Sachsenhofer et al. (2003). Various authors (e.g. Orr, 1986; Tomić et al., 1995) postulated earlier hydrocarbon generation for coals high in organic sulphur. Therefore, the low E_r and H averages determined for the Novogrodovskaya sample can be interpreted as earlier onset of transformation reactions related to hydrocarbon generation.

8.6 Conclusion

The present results indicate that apart from maturity, multiple parameters control the mechanical properties of macerals. In case of inertinites, the prevailing conditions (temperature, exposure) during paleo-wildfires represent the main controlling factor for the mechanical properties. E_r and H of liptinites are strongly influenced by transformational processes related to devolatilization at low to medium rank, and later hydrocarbon generation. Furthermore, variations in the depositional environment (e.g. increased organic sulphur content due to brackish conditions) might play an additional role. The mechanical properties of vitrinites show no clear correlation with maturity, as a result of multiple influencing factors such as mineral matter inclusions, depositional conditions, and transformation of the organic matter structure and possibly the generation of nanoporosity at advanced maturity. In order to achieve a deeper understanding of the interdependency between mechanical properties and microstructural features (e.g. nanoporosity, mineral inclusions), advanced characterization techniques such as transmission electron microscopy (TEM) are required, which will be a focus of future research.

References

Borodich, F. M., Bull, S. J., and Epshtein, S. A.: Nanoindentation in studying mechanical properties of heterogeneous materials, J. Min. Sci.+, 51, 470–476, https://doi.org/10.1134/s1062739115030072, 2015.

Chekunov, A. V., Kaluzhnaya, L. T., and Ryabchun, L. I.: The Dniepr–Donets paleorift, Ukraine, deep structures and hydrocarbon accumulations, J. Petrol. Geol., 16, 183–196, https://doi.org/10.1111/j.1747-5457.1993.tb00105.x, 1993.

Epshtein, S. A., Borodich, F. M., and Bull, S. J.: Evaluation of elastic modulus and hardness of highly inhomogeneous materials by nanoindentation, S. J. Appl. Phys. A., 119, 325–335, https://doi.org/10.1007/s00339-014-8971-5, 2015.

Izart, A., Sachsenhofer, R. F., Privalov, V. A., Elie, M., Panova, E. A., Antsiferov, V. A., Alsaab, D., Rainer, T., Sotirov, A., Zdravkov, A., and Zhykalyak, M. V.: Stratigraphic distribution of macerals and biomarkers in the Donets Basin: implications for paleoecology, paleoclimatology and eustacy, Int. J. Coal Geol., 66, 69–107, https://doi.org/10.1016/j.coal.2005.07.002, 2006.

Levenshtein, M. L., Spirina, O. I., Nosova, K. B., and Dedov, V. S.: Map of Coal Metamorphism in the Donetsk Basin (Paleozoic Surface), 1 : 500 000, Ministry of Geology of the USSR, Kiev, Ukraine, 1991.

Lutugin, L. I. and Stepanov, P. I.: Donets Coal Basin, Geological Committee, Coal Minings in Russia, St. Petersburg, Russia, 112–143, 1913.

Maystrenko, Y., Stovba, S., Stephenson, R., Bayer, U., Menyoli, E., Gajewski, D., Huebscher, C., Rabbel,W., Saintot, A., Starostenko, V., Thybo, H., and Tolkunov, A.: Crustal-scale pop-up structure in cratonic lithosphere: DOBRE deep seismic reflection study of the Donbas fold belt, Ukraine, Geology, 31, 733–736, https://doi.org/10.1130/g19329.1, 2003.

Misch, D., Groß, D., Huang, Q., Zaccarini, F., and Sachsenhofer, R. F.: Light and trace element composition of Carboniferous coals from the Donets Basin (Ukraine): An electron microprobe study, Int. J. Coal Geol., 168, 108–118, https://doi.org/10.1016/j.coal.2016.06.004, 2016.

Oliver, W. C. and Pharr, G. M.: An improved technique for determining hardness and elastic modulus using load and displacement sensing indentation experiments, J. Mater. Res., 7, 1564–1583, https://doi.org/10.1557/jmr.1992.1564, 1992.

Orr, W. L.: Kerogen/asphaltene/sulfur relationships in sulfur-rich Monterey oils, Org. Geochem., 10, 499–516, https://doi.org/10.1016/0146-6380(86)90049-5, 1986.

Privalov, V. A., Panova, E. A., Sachsenhofer, R. F., Izart, A., Antsiferov, A. V., and Antsiferov, V. A.: Delineation of gas prospective sites in the Donets Basin, Ukraine, 69th EAGE Conference & Exhibition, London, UK, 11–14 June 2007, https://doi.org/10.3997/2214-4609.201401846, 2007.

Pyne, S. J., Andrews, P. L., and Laven, R. D.: Introduction to Wildland Fire, J. Wiley & Sons, New York, USA, 769 pp., 1996.

Ritenberg, M. I.: Method of the investigation of facies and cycles, edited by: Makedonov, A. V., Correlation of Coalbearing Sediments and Coal Seams in the Donets Basin, Nauka, Leningrad, Russia, 71–95, 1972.

Sachsenhofer, R. F., Privalov, V. A., Izart, A., Elie, M., Kortensky J., Panova E. A., Sotirov, A., and Zhykalyak, M. V.: Petrography and geochemistry of Carboniferous coal seams in the Donets Basin (Ukraine): implications for paleoecology, Int. J. Coal Geol., 55, 225–259, https://doi.org/10.1016/s0166-5162(03)00112-5, 2003.

Sachsenhofer, R. F., Privalov, V. A., and Panova E. A.: Basin evolution and coal geology of the Donets Basin (Ukraine, Russia): an overview, Int. J. Coal Geol., 89, 26–40, https://doi.org/10.1016/j.coal.2011.05.002, 2012.

Scott, A. C. and Glasspool, I. J.: Observations and experiments on the origin and formation of inertinite group macerals, Int. J. Coal Geol., 70, 53–66, https://doi.org/10.1016/j.coal.2006.02.009, 2007.

Shulga, V. F. (Ed.): Lower Carboniferous Coal Formations of the Donets Basin, Nauka, Moscow, Russia, 176 pp., 1981.

Stephenson, R. A., Stovba, S. M., and Starostenko, V. I.: Pripyat–Dniepr–Donets Basin: implications for dynamics of rifting and the tectonic history of the northern Peri-Tethyan platform, edited by: Ziegler, P. A., Cavazza, W., Robertson, A. H. F., and Crasquin-Soleau, S., Peri-Tethyan Rift/Wrench Basins and Passive Margins: Peri-Tethys Memoir, Paris, France, 6, 369–406, 2001.

Stovba, S. M. and Stephenson, R. A.: The Donbas Foldbelt: its relationships with the uninverted Donets segment of the Dniepr–Donets Basin, Ukraine, Tectonophysics, 313, 59–83, https://doi.org/10.1016/s0040-1951(99)00190-0, 1999.

Taylor, G. H., Teichmüller, M., Davis A., Diessel, C. F. K., Littke, R., and Robert, P.: Organic Petrology, Borntraeger, Berlin-Stuttgart, Germany, 704 pp., 1998.

Tissot, B. P. and Welte D. H.: Petroleum Formation and Occurrence, Springer, Berlin, Germany, 699 pp., 1984.

Tomić, J., Behar, F., Vandenbroucke, M., and Tang, Y.: Artificial maturation of a Monterey kerogen (Type II-S) in a closed system and comparison with Type II kerogen: Implications on the fate of sulfur, Org. Geochem., 23, 647–660, https://doi.org/10.1016/0146-6380(95)00043-e, 1995.

Van Krevelen, D. W.: Coal, Elsevier, Amsterdam, the Netherlands, 514 pp., 1961.

Yule, B. L., Roberts, S., and Marshall, J. E. A.: The thermal evolution of sporopollenin, Org. Geochem., 31, 859–870, https://doi.org/10.1016/S0146-6380(00)00058-9, 2000.

Zickler, G. A., Schöberl, T., and Paris, O.: Mechanical properties of pyrolysed wood: A nanoindentation study, Philos. Mag., 86, 1373–1386, https://doi.org/10.1080/14786430500431390, 2006.

9 Publication II

Nanoscale pore structure of Carboniferous coals from the Ukrainian Donets Basin: A combined HRTEM and gas sorption study

Vranjes-Wessely, S.[1,2], Misch, D.[1], Issa, I.[2], Kiener, D.[2], Fink, R.[3], Seemann, T.[4], Liu, B.[5], Rantitsch, G.[1], Sachsenhofer, R.F.[1]

Int. J. C Geol., 224, 103484, 2020

1)Department of Applied Geosciences and Geophysics, Montanuniversität Leoben, A-8700 Leoben, Austria

2)Department of Materials Science, Montanuniversität Leoben, A-8700 Leoben, Austria

3)Institute of Geology and Geochemistry of Petroleum and Coal, RWTH Aachen University, D-52056 Aachen, Germany

4)Institute of Clay and Interface Mineralogy, RWTH Aachen University, D-52072 Aachen, Germany

5)Institute of Unconventional Oil and Gas, Northeast Petroleum University, Daqing City, 163318, China

Abstract

Various compositional, depositional and maturity related influencing factors affect the complex pore structure of coal. To study the pore structural evolution at nanoscale, a well characterized sample set of vitrinite-rich Carboniferous coals from the Ukrainian Donets Basin, covering a maturity interval from 0.69 to 1.47%Rr, was selected. Conventional bright field transmission electron microscopy (BF TEM) and high-resolution TEM (HRTEM) imaging was used to directly determine pore size distributions, pore morphology, geometry factors and other structural features, while gas invasion techniques such as low-pressure gas adsorption (CO_2 and N_2) were used for the investigation of micro- and mesopore structural parameters. High-pressure CH_4 sorption experiments revealed changes in the methane storage capacity within the investigated maturity range, while associated structural changes of vitrinite were monitored by Raman spectroscopy. The results indicate pore occlusion in vitrinite mainly at peak oil window maturity, the sensibility of micro- and mesopore structure to thermal maturity and the importance of organic sulphur as a catalyst for kinetics of structural modification. Observed structural changes at 1.10%Rr were related to the onset of wet-gas generation.

A structural control on micromechanical properties of vitrinite is indicated by the correlation between reduced elastic moduli from a previous study and average nanopore diameters obtained by HRTEM. The applied comprehensive approach improved the understanding of depositional and maturity-related processes that may affect pore evolution and resulting gas storage capacity of coals.

9.1 Introduction

Coal is still the most abundant and affordable energy carrier globally, with a large portion of the world's fuel resources being stored in coal seams. Here, methane (CH4) is generated by biogenic or thermogenic processes during progressing coalification (Rice, 1993) and produced as coal bed methane (CBM). Rapid desorption and presence of free gas in fractures, cleats or caverns might represent a significant mining hazard (firedamp); on the other hand, the desorption behavior strongly influences production characteristics. Depending on the pressure at which the methane was adsorbed, the main percentage of the initial gas content is stored in coal matrix pores by physical sorption (e.g., Gray, 1987; Rice, 1993; Harpalani and Chen, 1997; Moore, 2012). The pore structure of coal is typically heterogeneous and hence, a proper characterization is of particular importance for the estimation of coal reservoir capacity and production performance. Following the IUPAC system (Sing et al., 1985) pores are subdivided into macropores (diameter ≥ 50 nm), mesopores (diameter between 2 and 50 nm) and micropores (diameter ≤ 2 nm). The size distribution of those nanopores controls the dominant pore adsorption mechanism. Macro- and mesopores are mainly filled by (multi-) layer gas adsorption at the gas-solid interface, whereas adsorption in micropores is described by volume filling (Dubinin and Radushkevich, 1947; Mahajan and Walker Jr., 1978; Jaroniec and Choma, 1989; Mastalerz et al., 2008). Adsorption in micropores is generally considered as the main control on total storage capacity (Clarkson and Bustin, 1999; Mastalerz et al., 2008; Moore, 2012). Their availability and accessibility is controlled by various factors, particularly by coal rank (e.g., Gan et al., 1972; Rodrigues and Lemos de Sousa, 2002; Prinz et al., 2004; Pan et al., 2015) and maceral composition (e.g., Lamberson and Bustin, 1993; Crosdale et al., 1998; Clarkson and Bustin, 1999; Mastalerz et al., 2008). It is commonly accepted that higher rank coals (bituminous coal and anthracite) show abundant microporosity, while low rank coals (lignites and sub-bituminous coals) predominantly host meso- and macroporosity. However, Parkash and Chakrabartty (1986) and Gürdal and Yalçın (2001) found an opposite microporosity trend with increasing rank, while Bustin and Clarkson (1998) did not observe any consistent correlation. Various studies postulate a higher CH_4 sorption capacity for vitrinite compared to liptinite and inertinite macerals (e.g., Crosdale et al., 1998; Chalmers and Bustin, 2007; Ziegs et al., 2017 and references therein). The primary maceral distribution therefore also controls the pore space evolution with coal rank, as the processes involved in thermal maturation (e.g., hydrocarbon generation and bituminous transformation products) differ strongly for the respective maceral groups (Lamberson and Bustin, 1993; Crosdale et al., 1998; Ziegs et al., 2017; Misch et al., 2019b). Furthermore, Mastalerz et al. (2008) described a changing pore structure for different vitrinite submacerals. They suggested a positive correlation of both micro- and mesopore volumes with the presence of collotelinite, which is not observed for collodetrinite. Other studies contradict a clear relationship between maceral distribution and total nanopore volume or sorption capacity (e.g., Faiz et al., 1992; Gürdal and Yalçın, 2001; Guo et al., 2019). Busch et al. (2019) concluded that the primary factor controlling gas sorption might rather be the period of coal deposition, while Sakurovs et al. (2018) showed that variations in gas sorption behavior, porosity and other physical properties cannot be assigned to the age of deposition. All of those controversial findings reflect the complexity of coal nanostructures, further complicated by the wide array of analytical techniques with different detectable pore size ranges, specimen type, accuracy etc. (Pan et al., 2015). Low-pressure CO_2 and N_2 physisorption are established tools for structural characterization in the micro- to mesopore range (e.g., Clarkson and Bustin, 1999; Okolo et al., 2015a). Nevertheless, the characterization of poorly ordered, structurally undefined and non-rigid nanoporous solids via physisorption remains challenging, since calculated pore size distributions and average pore throat diameters based on idealized pore models might show considerable inaccuracy in case of complex and heterogeneously distributed pore geometries (e.g., Marsh, 1986; Thommes et al., 2015). Physisorption analysis might further be affected by specific interactions between the sample surface and the adsorptive (Thommes et al., 2015).

In contrast, high-resolution image-based pore characterization techniques allow for a direct observation of pore morphology and structural features within individual coal macerals. Highest-resolution techniques such as HRTEM are commonly applied to micrometer-sized, ultrathin specimen (<100 nm), thereby achieving resolutions down to the atomic scale (~0.14 nm) At this scale, a direct quantification of structural parameters such as pore size distribution, spacing of aromatic layers, etc. possible (e.g., Sharma et al., 2000a, Sharma et al., 2000b; Niekerk and Mathews, 2010; Mathews and Sharma, 2012; Okolo et al., 2015b; Wang et al., 2017). However, the typically very limited applicable specimen-volume implies questionable representativeness.

This study aims at combining the advantages of traditional sorption-based characterization (representative for the bulk coal sample) and direct pore visualization in the micro-and mesopore range of selected vitrinite macerals by HRTEM imaging at highest resolution, to complement bulk information with direct structural observations on the primary sorption-active maceral. To do so, a set of vitrinite-rich Carboniferous coal samples from the

Ukrainian Donets Basin was chosen for investigation. Those samples are well characterized regarding depositional environment, paleoecology, geochemistry, petrography and micromechanical behavior (e.g., Sachsenhofer et al., 2003, Sachsenhofer et al., 2012; Izart et al., 2006; Misch et al., 2016; Vranjes et al., 2018). Thus, the influence of coal rank and depositional environment on structural evolution and resulting storage capacity can be ideally studied. Low-pressure gas adsorption (CO_2, N_2) was utilized for a bulk characterization of pores in the micro- and mesopore range, whereas sorptive gas storage capacity was directly measured by high-pressure CH_4 sorption. (HR)TEM were used for the direct visualization of pores down to the sub-nanometer scale, as well as a quantification of actual pore geometries. Microstructural evolution was further evaluated via Raman spectroscopy. Raman spectral parameters from coals yield information about the molecular reorganization of the carbon network and are therefore a valuable tool to understand coal properties at certain coal rank (e.g., Guedes et al., 2010; Potgieter-Vermaak et al., 2011; Henry et al., 2019). Overall, the introduced, comprehensive approach refines the understanding of nanopore evolution in response to depositional and diagenetic processes, thereby promoting the application of highest-resolution microscopy in future studies on gas storage in coals.

9.2 Experimental

9.2.1 Samples

In total, eight vitrinite-rich samples from five Moscovian coal seams in the south-western part of the Donets Basin were investigated (Table 1). A detailed geological and stratigraphic overview of this area is given in Sachsenhofer et al. (2003), Sachsenhofer et al. (2012). Samples were selected based on their vitrinite reflectance (%Rr) obtained by Sachsenhofer et al. (2003), as well as on the availability of bulk geochemical and petrographical data. The chosen samples cover a vitrinite reflectance range of 0.69–1.47%Rr and show vitrinite percentages mostly >80% (normalized to total macerals). Due to the limited availability of sample material from Novogrodovskaya l1–4 and 13-bis l1–2, gas sorption tests were conducted on two equivalent samples, collected from the same seams, which exhibit similar bulk characteristics and vitrinite reflectance (Novogrodovskaya l1–2 and 13-bis l1–1; see Table 1).

Table 1. Applied methods, geochemical and compositional bulk parameters of the sample set from Table 1 in Sachsenhofer et al. (2003). (VR – vitrinite reflectance, db – dry basis, TOC – total organic carbon, HC – hydrocarbon, S1 – free hydrocarbons, Tmax – Rock Eval temperature of maximum HC-generation, HI – hydrogen index, mmf – mineral matter free).

by Sachsenhofer et al. (2003)												this study				
Mine	Sample	VR	Ash yield	TOC	Sulphur	S1	T_{max}	HI	Vitrinite	Liptinite	Inertinite	HRTEM	CH_4	CO_2	N_2	Raman
		%Rr	% db	wt %	% db	mg HC/g	°C	mg HC/g TOC	%mmf	%mmf	%mmf					Analysis
l1 (Novogrodovskaya)	4	0.69	4.68	76.52	4.16	8.90	435	257	79.3	9.4	11.3	x		x	x	x
	2	0.72	4.94	76.88	5.34	5.60	432	231	79.5	9.4	11.1		x	x	x	
l3 (Belozerskaya)	12	0.81	7.39	78.68	2.01	7.20	444	209	81.9	6.0	12.1	x	x	x	x	x
k7 (Centralnaya)	3	0.93	1.30	82.96	1.10	9.60	448	200	87.6	10.4	2.0	x	x	x	x	x
m3 (Bazhanova)	4	1.10	8.68	78.01	7.34	9.60	477	155	84.1	0	15.9	x	x	x	x	x
	8	1.23	2.84	86.81	2.42	12.80	476	149	88.9	0	11.1	x	x	x	x	x
l1 (13 bis)	1	1.44	5.34	84.31	3.21	2.70	489	121	84.4	0	15.6		x	x	x	
	2	1.47	6.12	83.52	3.37	2.20	490	119	87.8	0	12.3	x				x

9.2.2 TEM characterization

Vitrinite macerals were identified by optical light microscopy prior to TEM preparation, and powder samples were extracted directly from polished sections. The recovered vitrinite powder was further diluted in isopropanol, dispersed by ultrasonication for 10 min and finally dropped on a copper TEM grid with a lacey carbon film. TEM imaging was performed on a 200 kV TEM JEOL 2100F equipped with a spherical aberration corrector (CEOS) and a Gatan Orius SC 1000 CCD camera. The acquired micrographs were further processed via ImageJ, in order to obtain pore size distributions and geometry factors (see detailed work flow in the supplemental material; appendix A fig. A1). Interlayer spacings between fringes/planes were determined by fast Fourier Transformation (FFT) based processing and analysis using Digital Micrograph. To ensure representativeness, TEM screening for visible pores was conducted on at least five different particles per bulk coal sample.

9.2.3 High-pressure CH_4 sorption

High-pressure CH_4 sorption experiments were performed at 45 °C on dried (for >24 h at 378 K and vacuum conditions) and crushed bulk coal samples (<1 mm grain size) (see Table 1) using a manometric device. The experimental set-up allows measurements to pressures of up to 20 MPa; a detailed description can be found in Gasparik et al., 2012, Gasparik et al., 2013, Gasparik et al., 2014.

The excess sorbed amount (n_{excess}; Gibbs surface excess) is calculated from the total amount of CH_4 transferred (n_{trans}) into the sample cell (pressure steps up 10 MPa) subtracted by the amount of CH4 that can be stored in the available void volume V_{void} (Gasparik et al., 2014):

$$n_{excess}(P,T) = n_{trans}(P,T) - \bar{\rho}_g(P,T)\, V_{void} \tag{1}$$

$\bar{\rho}_g$ is the molar gas density calculated as a function of pressure (*P*) and temperature (*T*) conditions using the GERG Equation of State (Kunz and Wagner, 2012). The resulting isotherms were parameterized by a Langmuir-type excess sorption function:

$$n_{excess} = n_L \frac{P}{P_L(T) + P} \tag{2}$$

In this function, n_{excess} (mmol g^{-1}) is the excess amount of sorbed gas at a given pressure *P* (Pa). n_L (mmol g^{-1}) is the maximum Langmuir capacity (Langmuir volume), denoting the maximum sorption capacity at full occupancy of all sorption sites. The Langmuir pressure P_L (MPa) corresponds to the pressure *P* where half of the sorption capacity is reached. Sorption results were corrected to an ash-free basis to correct for the diluting effects of non-sorbing minerals.

9.2.4 Low-pressure CO_2 physisorption

Low-pressure CO_2 physisorption analysis was performed using a Micromeritics Gemini VII 2390 t device. The sieved 63–200 µm grain size fraction of seven bulk coal (see Table 1) samples (~0.2 g) was subjected to analysis. Samples were dried and degassed for approximately 24 h at 383 K. Adsorption measurements were taken at 21 relative pressure steps (P/P_0) between <0.0001 and 0.0362 and at isothermal conditions (273 K). The micropore volume and surface area were calculated from the CO_2 adsorption isotherms based on the Dubinin-Astakhov equation (see Dubinin, 1975).

9.2.5 Low-pressure N_2 physisorption

Low-pressure N_2 isotherms were obtained using a Micromeritics ASAP 2460 surface area and porosity analyzer at an operating temperature of 77 K. The measurements were conducted on the crushed 177–250 µm grain size fraction from seven bulk coal (see Table 1) samples (~0.7–3 g) that were previously degassed and dried for 10 h at 383 K. Adsorption capacity was measured at 29 relative pressure steps (P/P_0) between 0.001 and 0.994 and the desorption rate was monitored at 26 relative pressure points between 0.994 and 0.1.

Specific equivalent surface areas, mesopore volumes and mesopore size distributions were calculated using the Barett-Joyner-Halenda (BJH) adsorption theory (Barrett et al., 1951) from the adsorption branch. It needs to be emphasized that pore structural data obtained by BJH evaluation should be interpreted with caution as various studies on engineered materials revealed that pore sizes for narrow mesopores (< 10 nm) are underestimated by up to 20–30% (Thommes et al., 2015; Bertier et al., 2016 and references therein). Therefore, BJH pore structural results in this study are used as semiquantitative parameters for relative comparison of mesopore characteristics.

9.2.6 Raman spectroscopy

Raman spectra were acquired from the identical grains used to extract TEM samples. A Horiba LabRAM HR Evolution spectrometer with a 532 nm Nd:Yag laser (100 mW; density-filtered down to 3.2 mW at the specimen surface) was used to analyze ablated vitrinite surfaces, excluding structural alteration effects caused by prior polishing (Lünsdorf, 2016; Henry et al., 2018). At least six spectra were measured per vitrinite grain.

The acquired Raman spectra were evaluated numerically by the Iterative Fitting of Raman Spectra (IFORS) approach, an operator independent and iterative curve fitting method developed by Lünsdorf and Lünsdorf (2016). The D and G band positions (D_{max} and G_{max}), difference between G and D band positions as Raman band separation (G - D), D/G band intensity ratios and the Scaled Total Area, normalized to the D_{max} band (D-STA), were obtained as structural parameters.

9.3 Results

9.3.1 TEM characterization

TEM imaging focused on vitrinite, since it is the most abundant maceral in the investigated coal seams (Table 1) and is assumed to contain the main fraction of sorption-active micropores in most coals (e.g., Gan et al., 1972; Lamberson and Bustin, 1993; Clarkson and Bustin, 1996, Clarkson and Bustin, 1999; Crosdale et al., 1998; Chalmers and Bustin, 2007). The most abundant vitrinite sub-maceral in the analyzed coals is telovitrinite; it shows little to no cellular structure.

Imaging-based pore evaluation obtained from six vitrinite samples at varying maturity (0.69–1.47%Rr) reveals the changes in pore size distribution (PSD) characteristics within a narrow maturity range. For a better overview of the results, the obtained pore sizes and pore structural parameters are divided in different pore size ranges (≤ 2 nm (total micropores); ≤ 5 nm (lower mesopore range including total micropores); 2–50 nm (total mesopores); ≤ 50 nm (total micro- and mesopore range) corresponding to their calculated pore-area based equivalent pore diameters (Table 2). As the obtained equivalent PSD (≤50 nm) follows an unknown distribution (not Gaussian distributed) and host varying pore populations, bootstrap confidence intervals (BCa CI) are given as a statistical uncertainty measure (see Efron, 1987).

Table 2. Average equivalent pore diameter obtained from different pore size ranges and their average geometry factors plus standard deviation (SD). (VR – vitrinite reflectance; Eq. diameter – equivalent pore diameter; BCa CI – bias-corrected and accelerated confidence interval).

				average	95% BCa CI		SD	average	SD	average	SD	average	SD	average	SD
					lower	upper									
	Mine	Sample	VR	Eq. diameter				Perimeter		Aspect ratio		Circularity		Roundness	
			%Rr	nm				nm							
≤2 nm	l1 (Novogrodovskaya)	4	0.69	1.24	1.16	1.32	0.33	4.40	1.40	1.67	0.55	0.77	0.13	0.65	0.19
	l3 (Belozerskaya)	12	0.81	1.46	1.32	1.57	0.33	5.34	1.52	1.68	0.62	0.76	0.12	0.65	0.17
	l1 (13 bis)	2	1.47	1.52	1.37	1.67	0.26	5.86	1.51	1.80	0.58	0.71	0.19	0.60	0.17
≤5 nm	l1 (Novogrodovskaya)	4	0.69	2.66	2.43	2.86	1.40	9.40	5.03	1.69	0.84	0.79	0.15	0.66	0.18
	l3 (Belozerskaya)	12	0.81	3.25	3.02	3.49	1.15	11.81	4.40	1.73	0.68	0.77	0.13	0.64	0.18
	k7 (Centralnaya)	3	0.93	3.90	3.71	4.08	0.82	13.88	3.47	1.75	0.68	0.80	0.12	0.63	0.17
	m3 (Bazhanova)	4	1.10	3.84	3.60	4.08	0.80	13.97	3.30	1.77	0.65	0.77	0.13	0.62	0.16
	l1 (13 bis)	2	1.47	3.54	3.41	3.66	0.86	12.29	3.27	1.53	0.51	0.83	0.13	0.70	0.17
2 – 50 nm	l1 (Novogrodovskaya)	4	0.69	10.19	9.65	10.76	6.24	35.83	22.47	1.60	0.69	0.81	0.12	0.68	0.16
	l3 (Belozerskaya)	12	0.81	7.46	6.67	8.32	5.72	26.99	20.61	1.72	0.64	0.77	0.13	0.64	0.18
	k7 (Centralnaya)	3	0.93	9.73	9.02	10.45	6.60	34.87	24.62	1.66	0.64	0.79	0.12	0.66	0.17
	m3 (Bazhanova)	4	1.10	8.12	7.36	9.02	5.53	29.85	21.92	1.69	0.77	0.77	0.13	0.66	0.17
	l1 (13 bis)	2	1.47	8.36	7.88	8.90	6.06	30.25	23.22	1.53	0.45	0.79	0.11	0.69	0.16
≤50 nm	l1 (Novogrodovskaya)	4	0.69	9.20	8.65	9.69	6.52	32.38	23.38	1.60	0.68	0.81	0.12	0.68	0.16
	l3 (Belozerskaya)	12	0.81	6.93	6.11	7.79	5.72	25.06	20.62	1.72	0.63	0.77	0.13	0.64	0.18
	k7 (Centralnaya)	3	0.93	9.73	9.02	10.45	6.60	34.87	24.62	1.66	0.64	0.79	0.12	0.66	0.17
	m3 (Bazhanova)	4	1.10	8.08	7.24	9.01	5.54	29.70	21.92	1.69	0.77	0.77	0.13	0.66	0.17
	l1 (13 bis)	2	1.47	8.25	7.76	8.78	6.07	29.84	23.23	1.54	0.45	0.79	0.12	0.69	0.16

0.69%Rr – Novogrodovskaya l1–4

Vitrinite micrographs at 0.69%Rr are characterized by a broad frequency distribution of equivalent pore diameters in the micro- and mesoporous range (Fig. 1). General structural heterogeneity within individual and between different vitrinite particles is reflected by spatially varying pore sizes and structural features such as aromatic fringes (edges of condensed aromatic layers) (Fig. 2a). Also, a semi-graphitic domain with d_{002} spacing of 0.38 nm, appearing randomly within an amorphous carbon-matrix (Fig. 2b), is observed. Different pore geometries are revealed; these include i) circular pores, ii) irregular/spongy micro- and mesopores (inset in Fig. 1), as well as iii) slit-shaped pores between the randomly distributed aromatic fringe stacks (Fig. 2a). Novogrodovskaya vitrinite particles exhibit the highest proportion of visible micropores (≤2 nm) and largest pore population (micro- and mesopore fraction from five particles; *n* = 618).

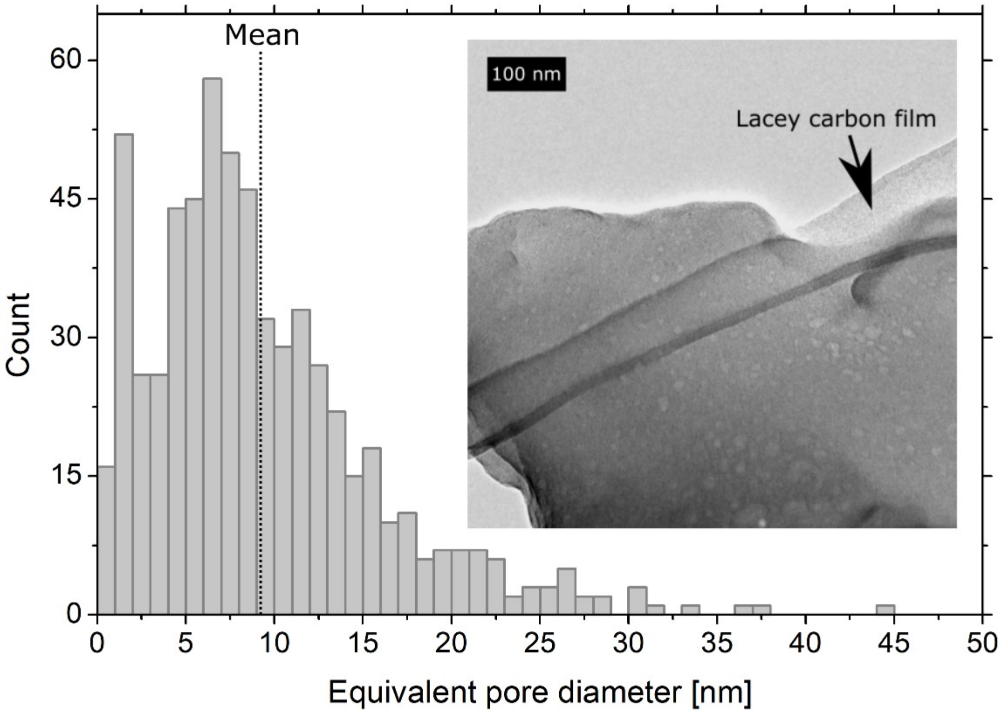

Fig. 1. Frequency distribution of equivalent pore diameters (*n* = 618) obtained from five telovitrinite particles at 0.69%Rr (l1–4). The inset shows a BF TEM image obtained from a telovitrinite particle displaying irregular/spongy pores. The particle is supported by a lacey carbon film.

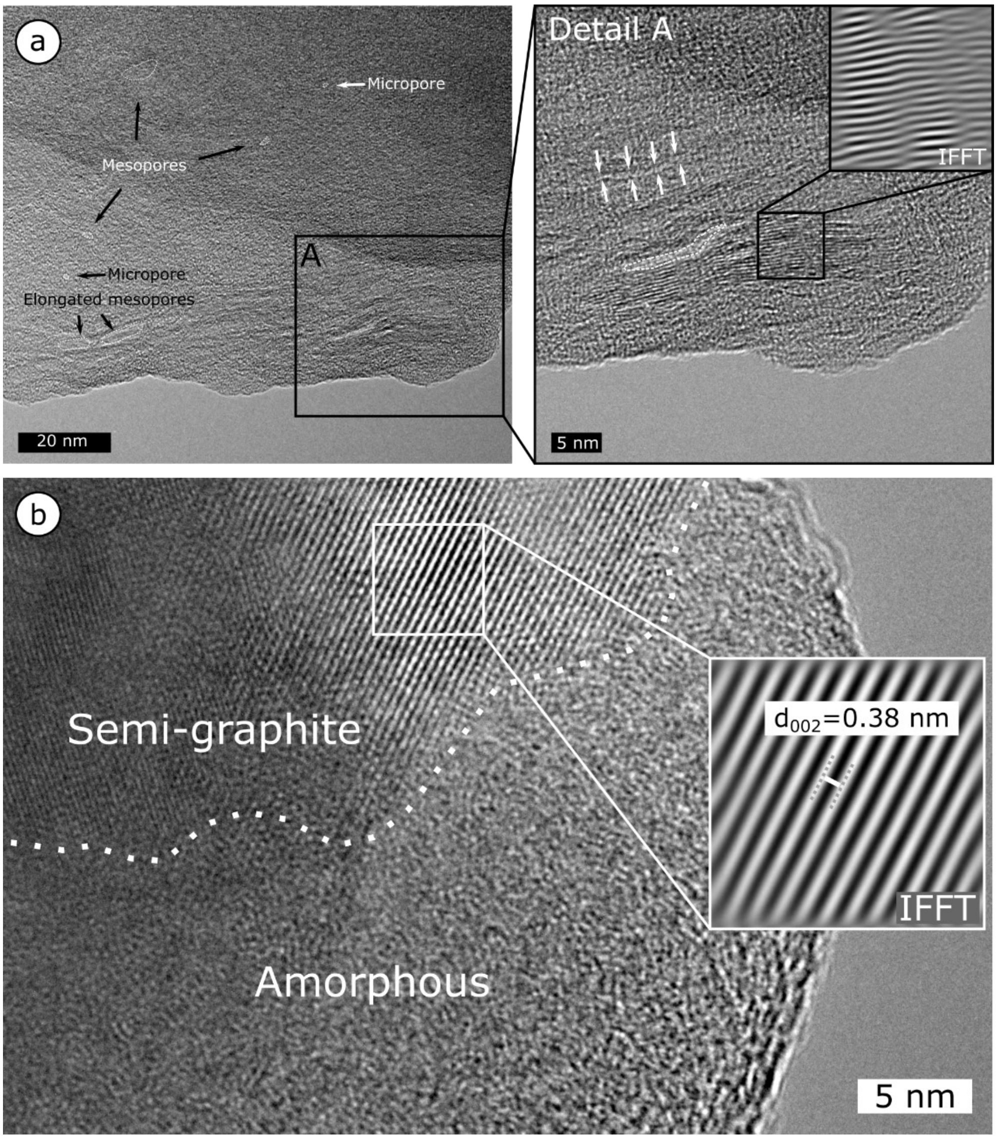

Fig. 2. (a) HRTEM image of telovitrinite at 0.69%Rr (l1–4) displaying different pore types and geometries. Detail A displays aromatic fringes and an inverse FFT (IFFT) obtained from a square framed area to show arrangements in detail. The boundary of a slit-shaped pore is highlighted in white; while white arrows indicate a channel-like pore structure. (b) HRTEM image showing a semi-graphitic domain observed in a telovitrinite particle. Inset shows the IFFT of the highlighted area.

0.81%Rr – Belozerskaya l3–12

Micro- and mesopores (Fig. 3) in Belozerskaya vitrinite are distributed heterogeneously. Large parts of the investigated particles appear non-porous. Additionally, onion-like carbons were found within a particle (Fig. 4). The onion-like carbon structures are hollow, partly deformed and show widths spanning between ~4 and 20 nm, with interlayer spacings ranging from 0.35 to 0.36 nm. The cores of the onion structures appear to be spherical or polyhedral mesopores, depending on the deformation grade.

Compared to the sample at 0.69%Rr, the mesopores at 0.81%Rr are more irregularly shaped (Table 2; circularity and aspect ratio) and the detected population of pores is relatively low (micro-and mesopore fraction from five particles; *n* = 191).

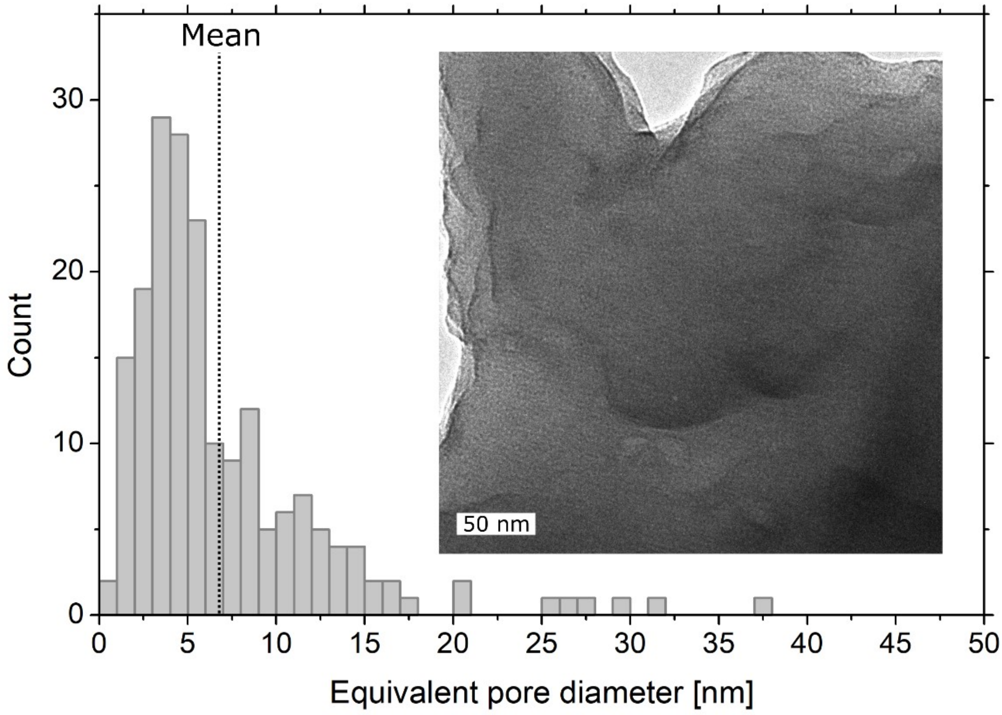

Fig. 3. (a) Frequency distribution of equivalent pore diameters (*n* = 191) obtained from five telovitrinite particles at 0.81%Rr (l3−12). Inset: BF TEM image showing telovitrinite with few visible pores.

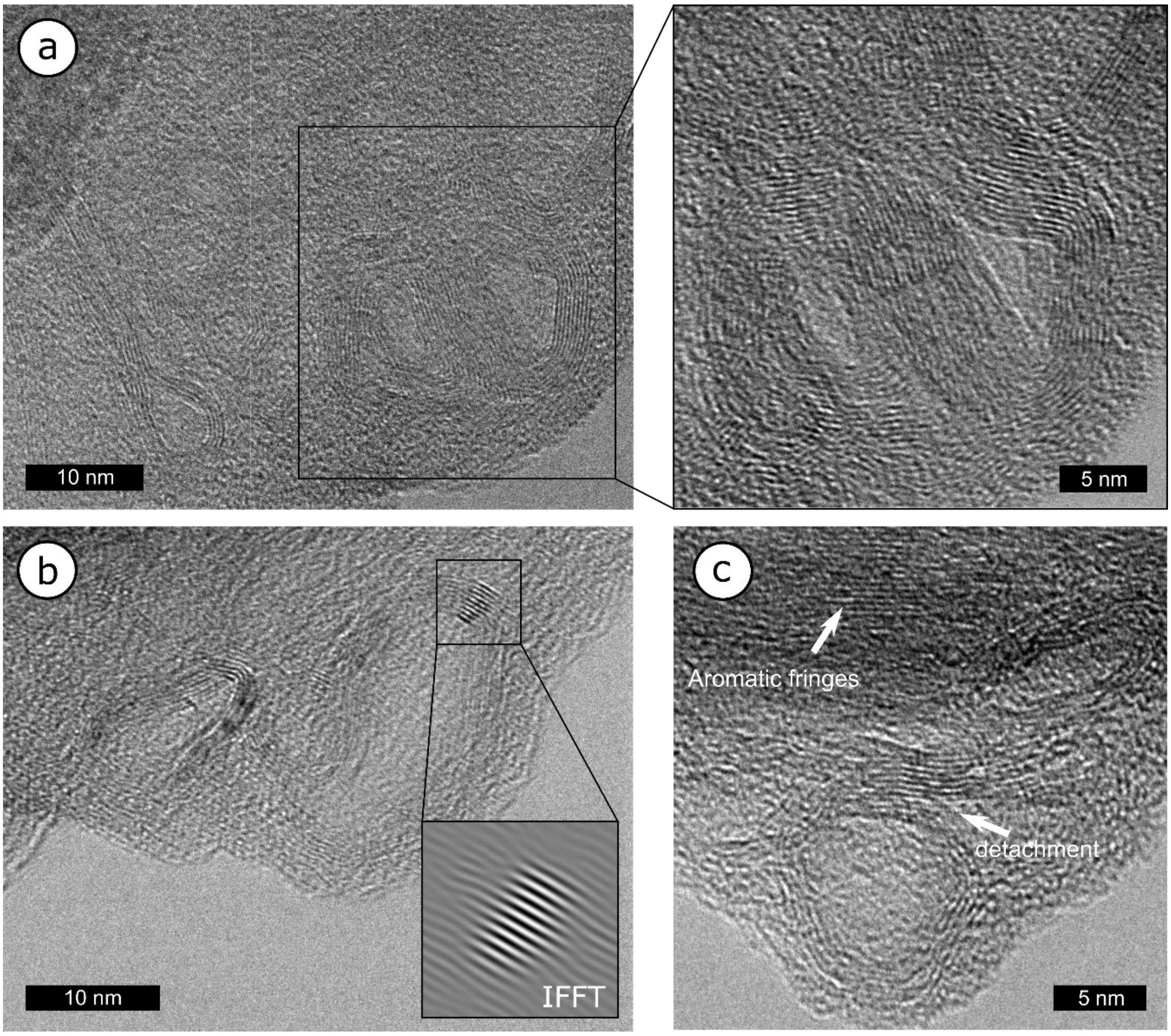

Fig. 4. HRTEM images of onion-like carbon rings within telovitrinite at 0.81%Rr (l3–12). The structures are either (a) irregularly deformed, (b) elongated or (c) well-rounded. The nanotexture of the layer stacking of (a) and (b) is well ordered (inset (b): IFFT). The texture of the roundly shaped und elongated onion-like carbon structure in (c) is characterized by distortion within the ring-structure and detachement of fringes in the upper part of the ring.

0.93%Rr – Centralnaya k7–3

At 0.93%Rr, no micropores could be visualized (Fig. 5a). The mesopores observed in five telovitrinite particles (*n* = 283) exhibit mostly irregular or elongated shapes and few channel structures (Fig. 5b). Large parts of the investigated vitrinite seem non-porous (Fig. 5c).

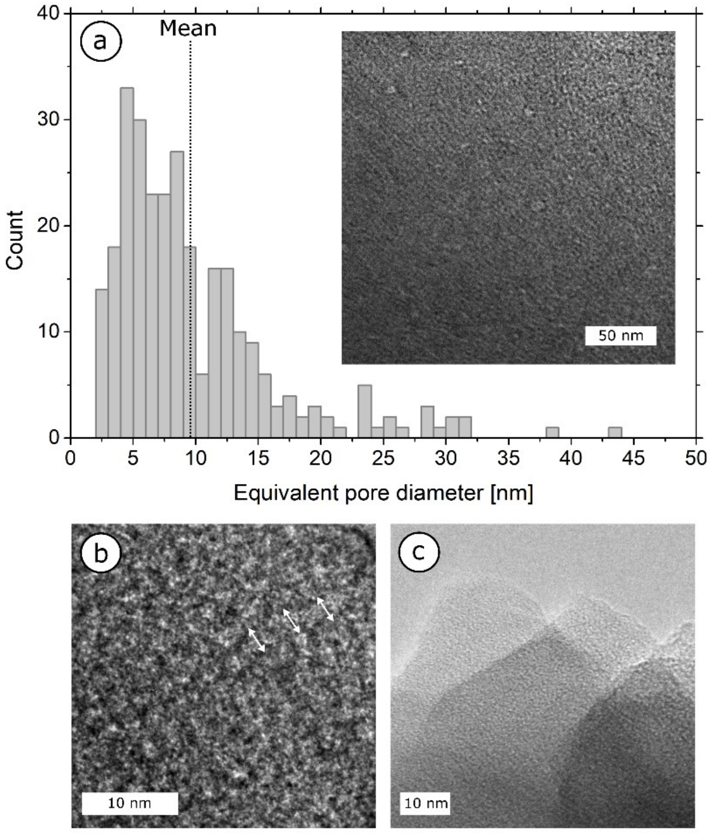

Fig. 5. (a) Frequency distribution of equivalent pore diameters (*n* = 283) obtained from five telovitrinite particles at 0.93%Rr (k7–3). Inset: BF TEM image showing a mesoporous telovitrinite particle. (b) Vitrinite with indicated channel-structure. (c) Non-porous telovitrinite displaying the characteristic layered structure of vitrinite.

1.10%Rr – Bazhanova m3–4

Compared to the remaining samples, the smallest number of pores was detected in Bazhanova vitrinite at 1.10%Rr (*n* = 150; Fig. 6a). The present pores show both irregular and circular shapes and fall into the mesopore size range (Fig. 6a, b). Moreover, some particles display channel-like pore structures (Fig. 6a, c), while no other structures were observed (aromatic stacks, semi-graphitic domains or onion-like carbons).

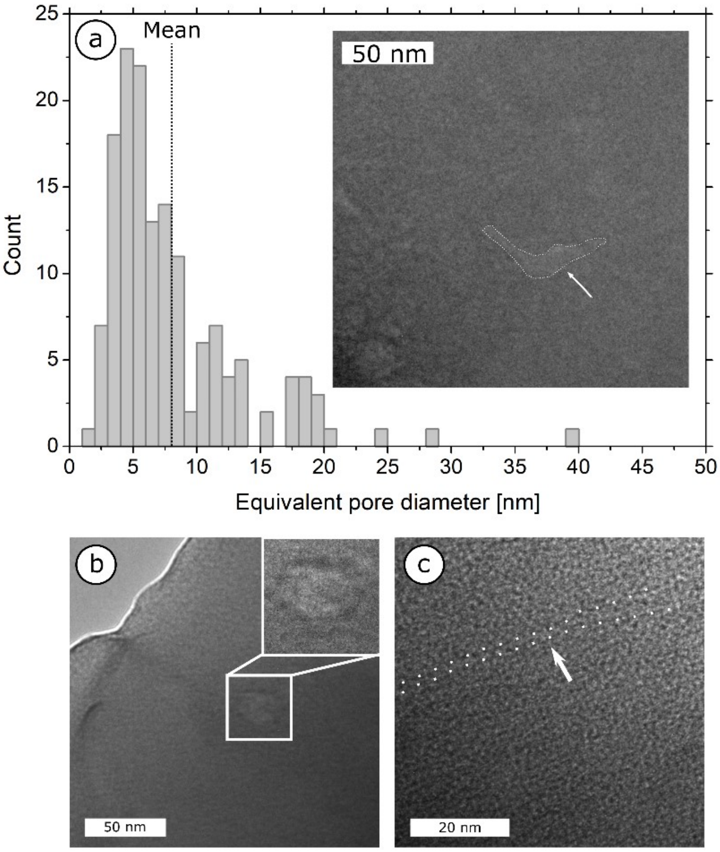

Fig. 6. (a) Frequency distribution of equivalent pore diameters (*n* = 150) obtained from five telovitrinite particles at 1.10%Rr (m3–4). Inset: BF TEM image showing a mesoporous telovitrinite particle with a highlighted channel structure in macropore size range (white arrow and dashed white border). (b) BF TEM image of telovitrinite at 1.10%Rr (m3–4) showing large mesopore. (c) Indicated channel-structure in vitrinite.

1.23%Rr – sample Bazhanova m3–8

At 1.23%Rr, a large fraction of the detected pores in telovitrinite particles expanded under electron beam irradiation (Fig. 7), indicating expansion of encapsulated gas. Therefore, a proper pore structure evaluation was not possible.

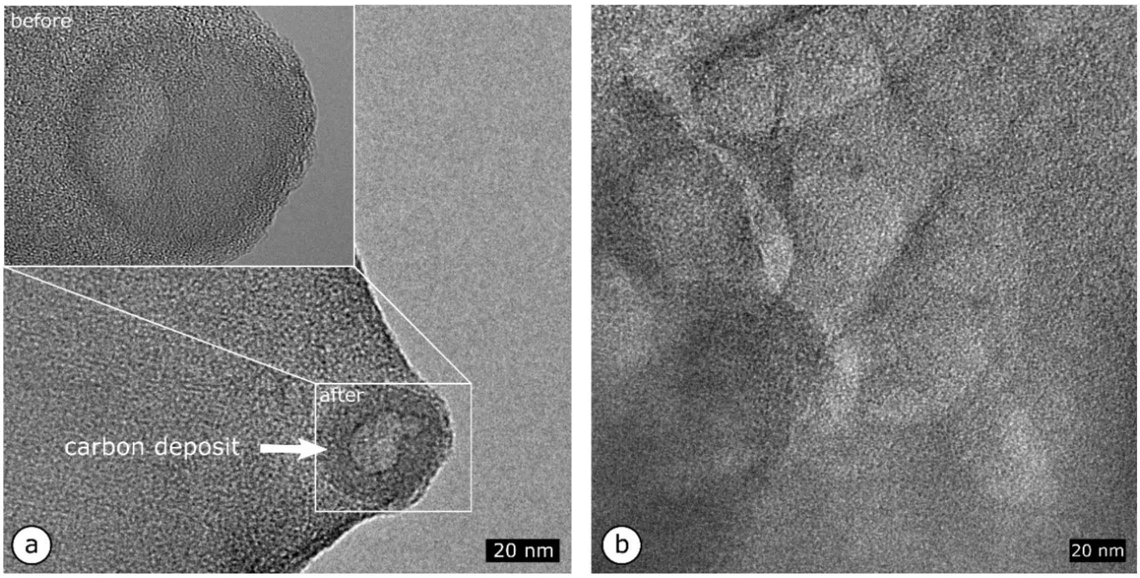

Fig. 7. (a) Micrographs documenting beam-induced pore growth in telovitrinite at 1.23%Rr (m3–8). Pore-growth occured within 2 to 3 min. With ongoing pore growth, the thickness of the area around the growing pores increases and apears darker due to carbon redeposition. (b) Pores exceed the mesopore size range with increasing electron beam-induced growth.

1.47%Rr – sample 13bis l1–2

Vitrinite particles at 1.47%Rr show a broad equivalent pore size distribution covering micro- and mesopores (Fig. 8) and a relatively large total population of detected pores (*n* = 594). No uniform spatial pore distribution regarding size and pore-to-pore distance could be observed. The particles are characterized by a pore structural heterogeneity and display various structures such as pore channels, pore clusters and various other pore geometries (Figs. 9). The most abundant pores are slightly irregular or spherically to elliptically shaped (Fig. 9e, f, g). All pore size ranges at 1.47%Rr, except micropore range (≤ 2 nm), exhibit the highest circularity and lowest aspect ratio compared to samples at lower maturity (Table 2). A minor number of unstable, bubble-like voids (see appendix B fig. B1) were observed in two particles. Those pores grow under electron beam irradiation, similar to the observations made at 1.23%Rr. Unstable pores are not considered in the processing of pore distributions.

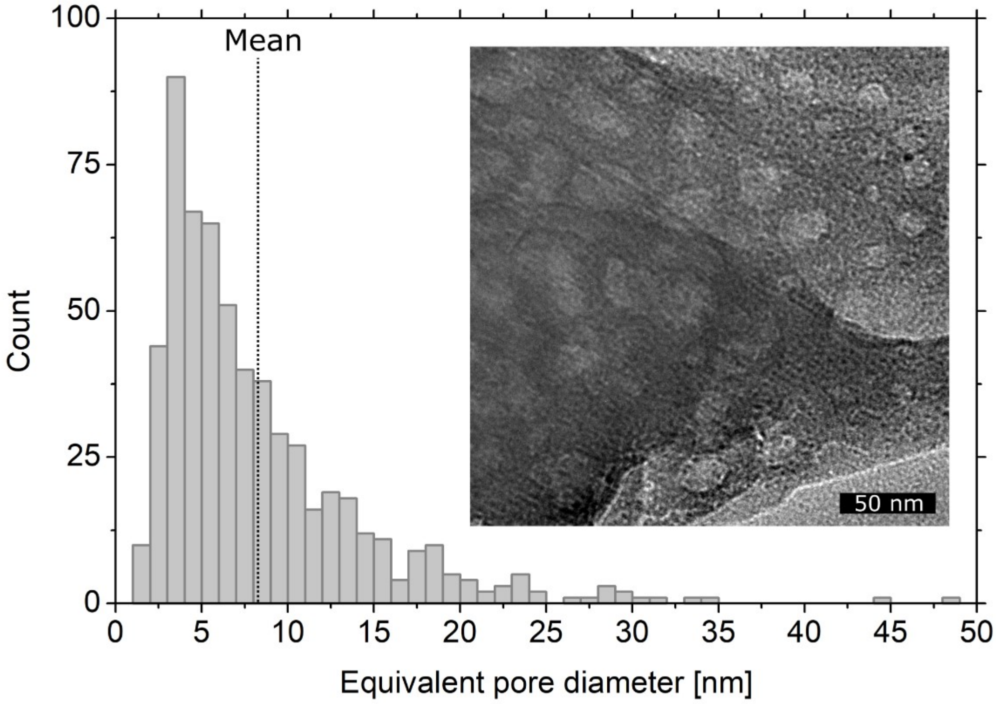

Fig. 8. Frequency distribution of equivalent pore diameters (*n* = 594) obtained from five telovitrinite particles at 1.47%Rr (l1−2). Inset: micrograph showing a mesoporous, layered telovitrinite particle.

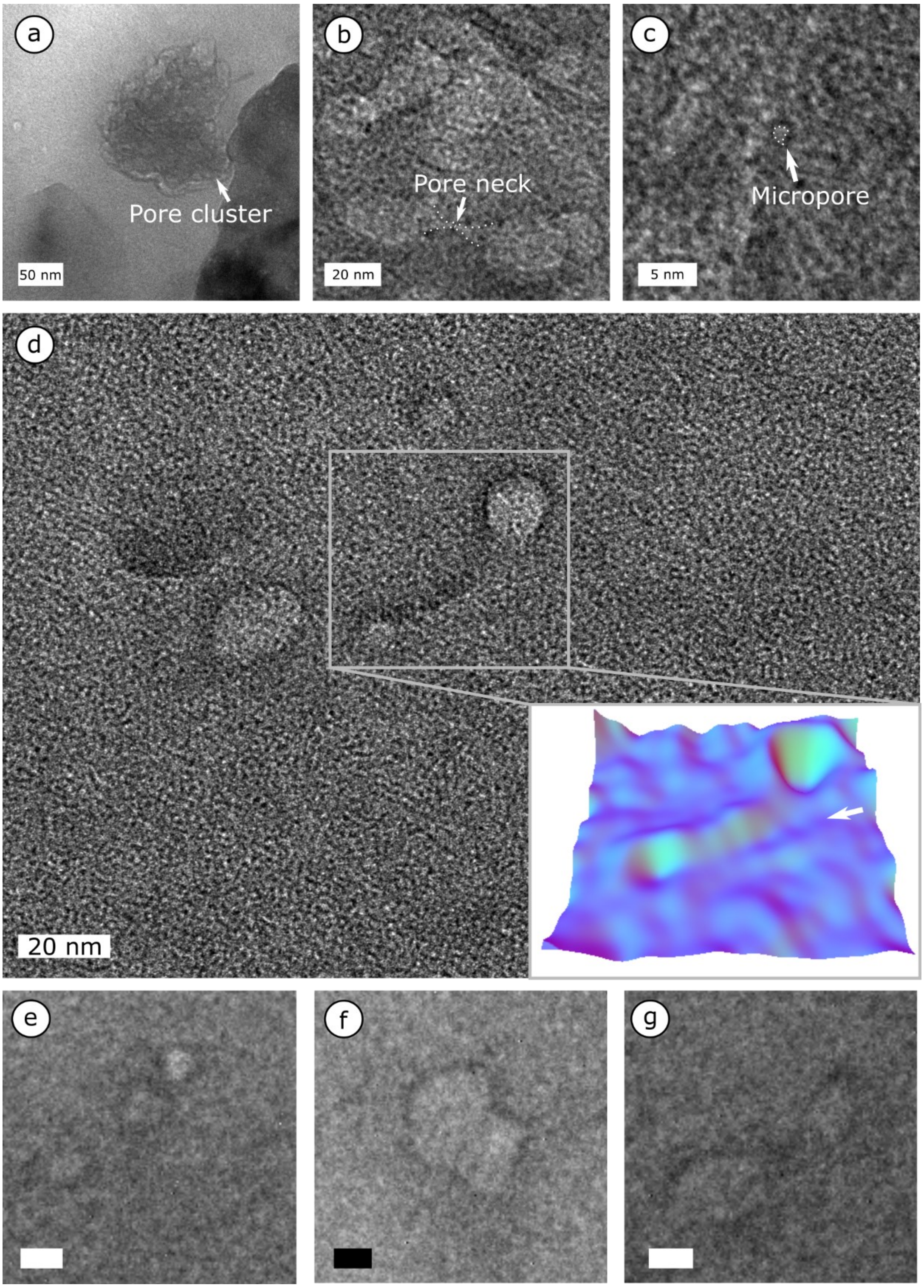

Fig. 9. Micrographs of various telovitrinite particles at 1.47%Rr (l1–2) displaying: (a) a pore cluster, (b) connected and irregular pores, as well as (c) micropores. (d) Circular and irregularly shaped mesopores and a channel-like structure connecting circular mesopores. Inset (d) shows a smoothed pseudo color 3D surface graph of the highlighted area, which helps to enhance the channel morphology (indicated with an arrow). Various pore geometries observed in a vitrinite particle; (e) circular, (f) angular and (g) elongated (scale bars in e, f, g: 10 nm).

9.3.2 High-pressure CH_4 sorption

High-pressure CH_4 excess sorption isotherms from six dry bulk coal samples (0.72–1.44%Rr) at 45 °C are shown in Fig. 10a. It was not possible to measure coal samples from Novogrodovskaya l1–4 (0.69%Rr) and 13-bis l1–2 (1.47%Rr) directly, due to lacking sample material. Instead, samples with similar bulk characteristics from the respective seams were used (see Table 1). Langmuir excess sorption capacity n_L increases with coal rank with values ranging from 0.68 to 0.81 mmol g^{-1} (Table 3). Novogrodskaya at 0.72%Rr exhibits the lowest sorption capacity n_L, whereas the highest value is observed at 1.44%Rr. At 1.10%Rr a drop in Langmuir sorption capacity n_L can be observed (Fig. 10b). This trend can equally be observed for maximum measured excess sorption capacities which vary from 0.52 to 0.70 mmol g^{-1} (Table 3). The Langmuir pressure P_L decreases linearly from lower to higher maturity, with values ranging from 2.90 to 1.56 MPa (Fig. 10b, Table 3).

Table 3. Maximum measured CH_4 excess sorption capacity (at 45 °C) and resulting Langmuir fitting parameters (Eq. 2) corrected to an ash-free basis. (VR – vitrinite reflectance).

			Measured	Fitting parameters	
Mine	Sample	VR	Max. CH_4 excess sorption	Langmuir volume n_L	Langmuir pressure P_L
		%Rr	mmol g^{-1}	mmol g^{-1}	MPa
l1 (Novogrodovskaya)	2	0.72	0.52	0.68	2.90
l3 (Belozerskaya)	12	0.81	0.56	0.71	2.72
k7 (Centralnaya)	3	0.93	0.63	0.76	2.31
m3 (Bazhanova)	4	1.10	0.59	0.71	1.98
	8	1.23	0.65	0.76	1.73
l1 (13 bis)	1	1.44	0.70	0.81	1.56

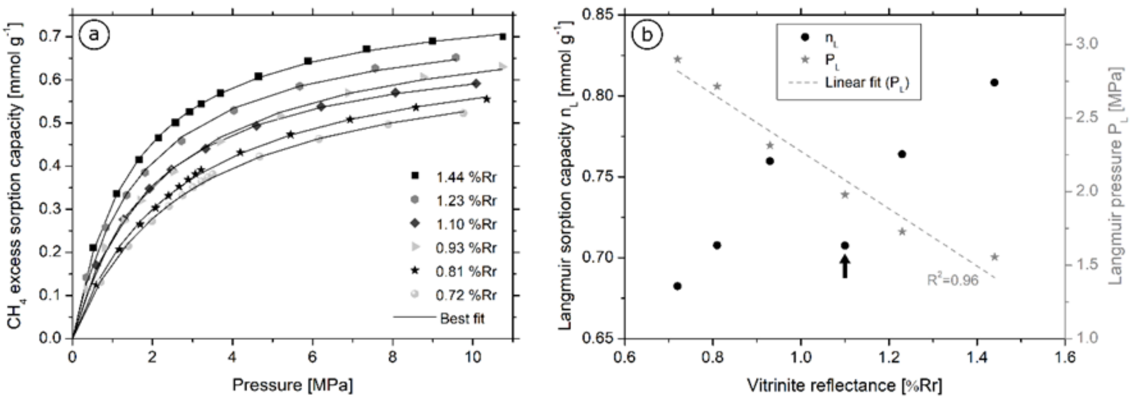

Fig. 10. (a) CH_4 excess sorption isotherms measured at 45 °C on dry samples, corrected to an ash-free basis. Best fit lines are results of the Langmuir-based model (Eq. 2). (b) Plot of Langmuir parameters versus vitrinite reflectance. At 1.10%Rr a drop in sorption capacity is observed (indicated with an arrow).

9.3.3 Low-pressure CO_2 physisorption

Low-pressure CO_2 physisorption isotherms were obtained from seven dry bulk coal samples (0.69–1.44%Rr) at 273 K and can be found in supplemental material (appendix C fig. C1). The adsorbed quantities of CO_2 at the highest pressure vary from 0.68 mmol g^{-1} for the coal at 1.44% to 0.51 mmol g^{-1} at 0.69%Rr. The micropore volume and equivalent surface area were calculated from the isotherms based on the Dubinin-Astakhov model (Table 4). The two samples exhibiting lowest coal rank (0.69 and 0.72%Rr, respectively) show micropore volumes of 0.0368 and 0.0377 cm^3/g. At low to intermediate maturity, the micropore volume decreases with a minimum at 0.93%Rr (0.0319 cm^3/g). The sample at 1.10%Rr shows a similarly low micropore volume (0.0329 cm^3/g). With ongoing maturation, the volume increases again and reaches its maximum at 1.44%Rr (0.0447 cm^3/g). A comparable trend with increasing coal rank can be also observed for the micropore equivalent surface areas with values ranging from 82.31 to 102.42 m^2/g.

Table 4. Micropore volume and equivalent surface area evaluated by the Dubinin-Astakhov model from CO_2 isotherms. (VR – vitrinite reflectance).

Mine	Sample	VR %Rr	Micropore volume cm^3/g	Error cm^3/g	Micropore surface area m^2/g
l1 (Novogrodovskaya)	4	0.69	0.0368	0.00012	91.45
	2	0.72	0.0377	0.00021	95.94
l3 (Belozerskaya)	12	0.81	0.0344	0.00014	89.35
k7 (Centralnaya)	3	0.93	0.0319	0.00025	82.31
m3 (Bazhanova)	4	1.10	0.0329	0.00016	84.46
	8	1.23	0.0397	0.00012	99.75
l1 (13 bis)	1	1.44	0.0447	0.00017	102.42

9.3.4 Low-pressure N_2 physisorption

Low-pressure N_2 adsorption isotherms have been determined for seven dry bulk coal samples (0.69–1.44%Rr). PSD were calculated based on the BJH model from the adsorption branches (Table 5). The BJH PSD (appendix D fig. D1) exhibits mostly broad, unimodal distributions with average mesopore sizes ranging from 14.8–29.8 nm. The highest mesopore volume is obtained from the sample at 1.10%Rr (0.0054 cm^3/g) (Table 5). BJH surface area varies from 0.23 to 1.44 m^2/g.

Table 5. BJH specific mesopore volume, surface area and average pore size obtained from the adsorption branches of low-pressure N_2 sorption isotherms. (VR – vitrinite reflectance).

Mine	Sample	VR	Mesopore volume	Mesopore surface area	Average mesopore size (4V/A)
		%Rr	cm^3/g	m^2/g	nm
l1 (Novogrodovskaya)	4	0.69	0.0025	0.369	26.8
	2	0.72	0.0027	0.579	18.6
l3 (Belozerskaya)	12	0.81	0.0017	0.226	29.8
k7 (Centralnaya)	3	0.93	0.0019	0.282	27.6
m3 (Bazhanova)	4	1.10	0.0054	1.444	14.8
	8	1.23	0.0022	0.429	20.8
l1 (13 bis)	1	1.44	0.0030	0.430	27.8

9.3.5 Raman spectroscopy

The collected Raman spectra for six samples at 0.69–1.47%Rr (Fig. 11) are characterized by interfering fluorescence signals but still exhibit distinct D and G bands. D_{max} and G_{max} positions shift from 1350 to 1333 cm^{-1} and 1580–1586 cm^{-1}, respectively. Mean D-STA, G - D band position differences and G-shape factor shift as well with ongoing maturation (Table 6; Fig. 12). D_{max}/G_{max} intensity ratios are only slightly increasing with higher measured vitrinite reflectance (Table 6). The shape of the D-band region changes significantly at 1.10%Rr compared to spectra collected from vitrinite at lower maturity which is a result of an evolving band separation in the D-band region (Fig. 11).

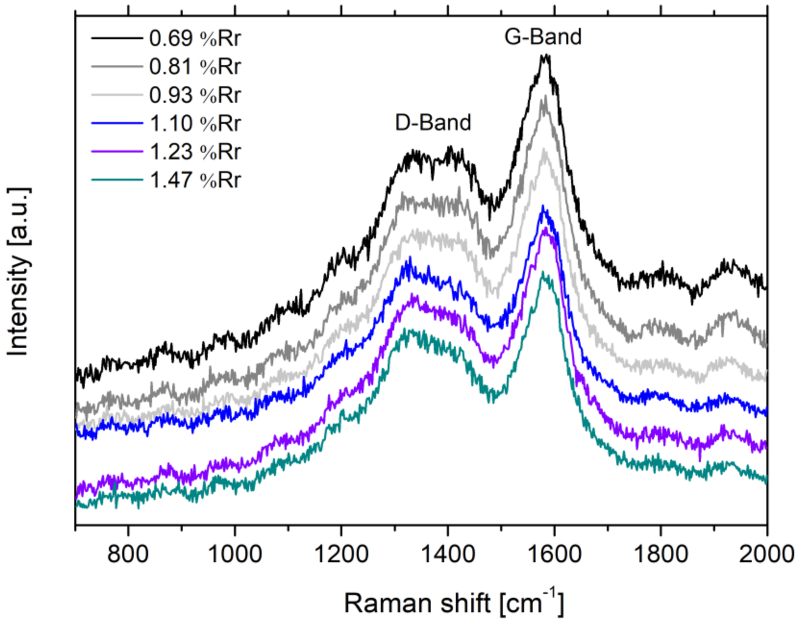

Fig. 11. Representative Raman spectra from telovitrinite grains at different maturity.

Table 6. Raman parameters (average values) obtained from the analyzed samples via IFORS (Lünsdorf and Lünsdorf, 2016). (VR – vitrinite reflectance, SD – standard deviation, D-STA – Scaled Total Area normalized to D_{max}).

Mine	Sample	VR %Rr	D_STA	SD	G shape factor	SD	D_{max} cm^{-1}	SD cm^{-1}	G_{max} cm^{-1}	SD cm^{-1}	D_{max}/G_{max} Intensity	SD	G-D cm^{-1}
l1 (Novogrodovskaya)	4	0.69	300.9	9.0	1.49	0.03	1350.5	34.8	1580.3	3.5	0.67	0.02	229.8
l3 (Belozerskaya)	12	0.81	293.3	8.2	1.50	0.03	1337.3	23.0	1581.5	3.9	0.70	0.02	244.2
k7 (Centralnaya)	3	0.93	288.6	6.1	1.51	0.04	1337.2	8.9	1582.8	3.3	0.70	0.01	245.6
m3 (Bazhanova)	4	1.10	278.6	7.1	1.56	0.03	1333.5	9.5	1583.7	5.1	0.72	0.02	250.2
	8	1.23	283.4	9.9	1.56	0.04	1332.3	13.3	1582.2	3.6	0.72	0.03	249.9
l1 (13 bis)	2	1.47	278.0	6.0	1.57	0.04	1333.0	5.9	1586.4	4.6	0.72	0.03	253.4

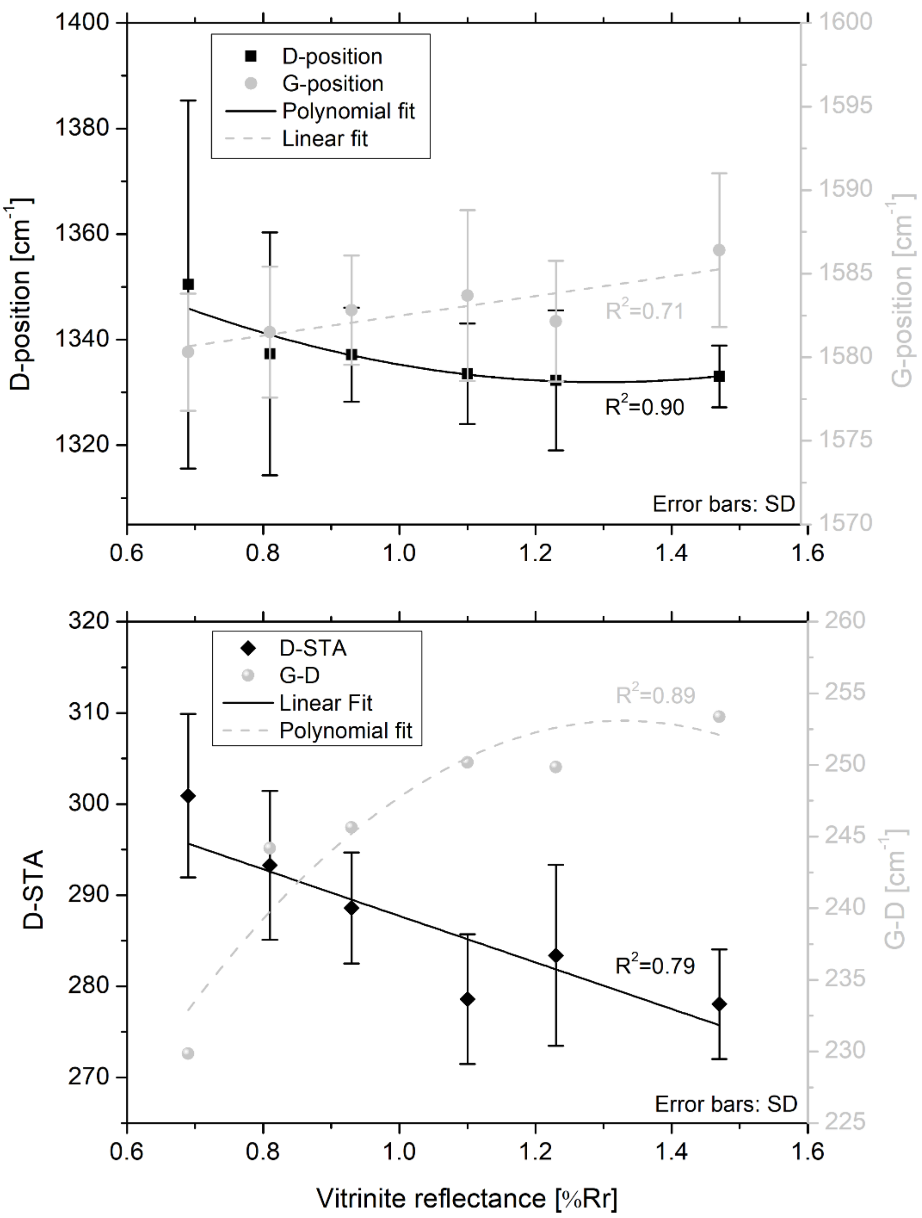

Fig. 12. Evaluated Raman parameters as a function of vitrinite reflectance. (SD – standard deviation).

9.4 Discussion

9.4.1 Structural response to thermal maturity and depositional environment

Raman spectroscopy is a viable tool to characterize the progressing modification of chemical bonding, particularly in semi- to well-ordered carbonaceous materials (e.g., Tuinstra and Koenig, 1970; Friedel and Carlson, 1972; Beny-Bassez and Rouzaud, 1985; Beyssac et al., 2003; Potgieter-Vermaak et al., 2011; Henry et al., 2019). Nevertheless, especially in the amorphous to low-ordering range, variability of Raman parameters often hinders structural interpretations. Parameters obtained in this study resulting from the collected spectra (Fig. 11) still exhibit certain trends despite the high statistical spread, which is generally due to low organic maturity. An increase of structural order of vitrinite is indicated with decreasing D_{max} band positions and a minor increase of G_{max} positions (Table 6; Fig. 12). The G_{max} band becomes subsequently narrower and develops toward higher asymmetry, which is pointed out by increasing G-shape-factors. Furthermore, the spectral changes are accompanied by a continuous decrease of D-STA and increasing G - D band position differences. According to Lünsdorf (2016) it is difficult to assign a certain process to the observable D_{max} shift for coal rank up to ~3%Rr, as different coalification processes such as the expulsion of aliphatic components, formation and rearrangement of basic structural units (BSU; Oberlin et al., 1974) and progressing growth of aromatic structures influence the Raman signal. Nevertheless, D-STA is still used as a confident maturity parameter for coals (Lünsdorf and Lünsdorf, 2016; Lünsdorf, 2016). The obtained D-STA and G - D band separation trends suggest a gradual increase in structural order or aromatization. The good correlation between D-STA and Langmuir pressure ($R^2 = 0.87$) supports the interpretation of Laxminarayana and Crosdale (1999), who concluded a strong relationship of decreasing Langmuir pressure and progressing homogenization of pore surfaces (subsequently increasing aromaticity). As seen in Fig. 11, a significant D band change occurs at 1.10%Rr, indicating a structural change. This is interpreted as the onset of peak gas conversion and associated repolymerization of the vitrinite structure (Levine, 1993).

The HRTEM evaluation of vitrinite particles revealed structural heterogeneities between maturity stages. The lowest rank vitrinite (Novogrodovskaya; 0.69%Rr) hosts semi-graphite-like domains within the amorphous vitrinite matrix (Fig. 2b). Misch et al. (2016) reported high organic sulphur contents for vitrinite particles from the respective seam, explained by a brackish depositional environment. The elevated organic sulphur might promote the accelerated transformation into a graphite-like structure due to the breaking up of weaker C-S bonds, triggering an intense reorganization of the carbon structure (Bonijoly et al., 1982; Oberlin, 1984; Bustin et al., 1995; Beyssac et al., 2002). It is well known that the formation and growth of graphite during metallurgical processes is enhanced by addition of high S proportions (Liu and Loper, 1991), and the presence of graphite-like nanoclusters and semi-ordered polycondensed aromatic layers in similar coals was documented by several XRD and HRTEM studies (e.g., Lu et al., 2001; Binoy et al., 2009; Manoj and Kunjomana, 2012; Mathews and Sharma, 2012; Manoj, 2014). The d_{002} spacing of the observed well-ordered domains (Fig. 2b) differs from perfectly ordered graphite d_{002} (0.38 nm versus 0.335 nm, respectively), indicating semi-graphite (Kwiecińska and Petersen, 2004; Rantitsch et al., 2016).

In Belozerskaya vitrinite at 0.81%Rr, hollow and deformed "onion-like" fullerene-related structures were observed (Fig. 4). Such structures were described in Sharma et al. (2000a) for natural bituminous coals, and are well documented for both natural and synthetic carbon-based materials (e.g., Beyssac et al., 2002; Xu, 2008; Romero-Sarmiento et al., 2014 and references therein). Beam-induced alteration of the onion-like carbon structures during HRTEM analysis was not observed. Romero-Sarmiento et al. (2014) interpreted the onion-like structure observed in organic matter particles from a gas mature shale sample as a result of secondary cracking of retained hydrocarbons. The finds at 0.81%Rr show that there must be alternative mechanisms that lead to formations of such structures at oil maturity, which are yet unknown.

The observed modifications already at early thermal maturity might superimpose the inherited primary vitrinite structure and likely represent an important influencing factor to the abundance of micropores for gas storage, as documented by pores associated with edges of aromatic stacks and onion-like structures (Figs. 2a, 4).

9.4.2 Maturity and compositional control on gas sorption data

Although the investigated bulk coal samples consist mainly of vitrinite (~79–87%mmf), varying inertinite and liptinite contents need to be considered with respect to their contribution to total microporosity (Table 1). Inertinite proportions are comparable for most of the samples (~11–16%mmf) except of Centralnaya k7–3 (~2%mmf). As most studies indicate, inertinite is mainly characterized by mesoporosity (Harris and Yust, 1976, Harris and Yust, 1979; Lamberson and Bustin, 1993). Chalmers and Bustin (2007) report microporosity as being mainly associated with "reactive" inertinite (e.g., semifusinite) which shows a structure similar to vitrinite; however, as reported in Sachsenhofer et al. (2003), the abundance of such sub-macerals in the inertinite fraction of the investigated coals is low.

Similarly, microporosity associated with liptinite (≤ 10%mmf) is likely negligible, as it occurs in an overall low quantity and is mostly characterized by a meso- to macroporous structure and comparably low adsorption capacity (Harris and Yust, 1976, Harris and Yust, 1979; Chalmers and Bustin, 2007; Ziegs et al., 2017; Misch et al., 2019b). The total micropore volume can therefore likely be attributed to the vitrinite portion (Harris and Yust, 1979; Gan et al., 1972; Lamberson and Bustin, 1993; Clarkson and Bustin, 1996, Clarkson and Bustin, 1999), albeit that minor microporosity might be contributed particularly by semi-inertinites (Chalmers and Bustin, 2007), and, to a lesser extent, liptinites.

The parabolic relation of CO_2 micropore volume and coal rank shown in Fig. 13a displays a minimum at 0.93 and 1.10%Rr (also observable for equivalent micropore surface area). This trend is in accordance with CO_2 micropore volumes obtained from Carboniferous coals from the Zonguldak Basin (Turkey) by Gürdal and Yalçın (2001). The decreasing micropore frequency between 0.69 and 0.93%Rr is interpreted as progressing occlusion of micropores at the onset of hydrocarbon generation. The subsequent increase in microporosity is therefore interpreted as a result of further thermal cracking of bituminous pore fillings, diminishing pore occlusion in vitrinite (e.g., Thomas Jr. and Damberger, 1976; Levine, 1991, Levine, 1993; Löhr et al., 2015). This process seems to mainly affect micropores, as low-pressure N_2 adsorption data does not show corresponding maturity trends (Table 5). Mesoporosity contributed by inertinite and liptinite macerals might affect the results obtained by low-pressure N_2 adsorption (which is mainly sensitive to the mesopore range) and might be at least partly responsible for discrepancies between N_2 (mesopore) and CO_2 (micropore) results. Nevertheless, as vitrinite is by far the dominant maceral group, and as samples of equal vitrinite percentages but from different thermal maturity stages exhibit considerably different mesoporosity, thermal maturation is proposed to be the main factor controlling porosity evolution for the investigated sample set. This is further supported by a strong trend of CH_4 sorption capacity (and particularly Langmuir pressure) with coal rank, and suggests that the N_2 adsorption data equally reflects mesoporosity in vitrinite, which likely observes greater structural changes (including pore occlusion and subsequent opening; Löhr et al., 2015; Misch et al., 2019a) with increasing maturation compared to inertinite (Levine, 1993).

9.4.3 Comparability of pore structural data from gas sorption and HRTEM

As shown in Fig. 13b, both the micropore and total mesopore fractions show maxima at relatively immature and highly mature stages, whereas pore counts in samples at peak oil window maturity are considerably lower.

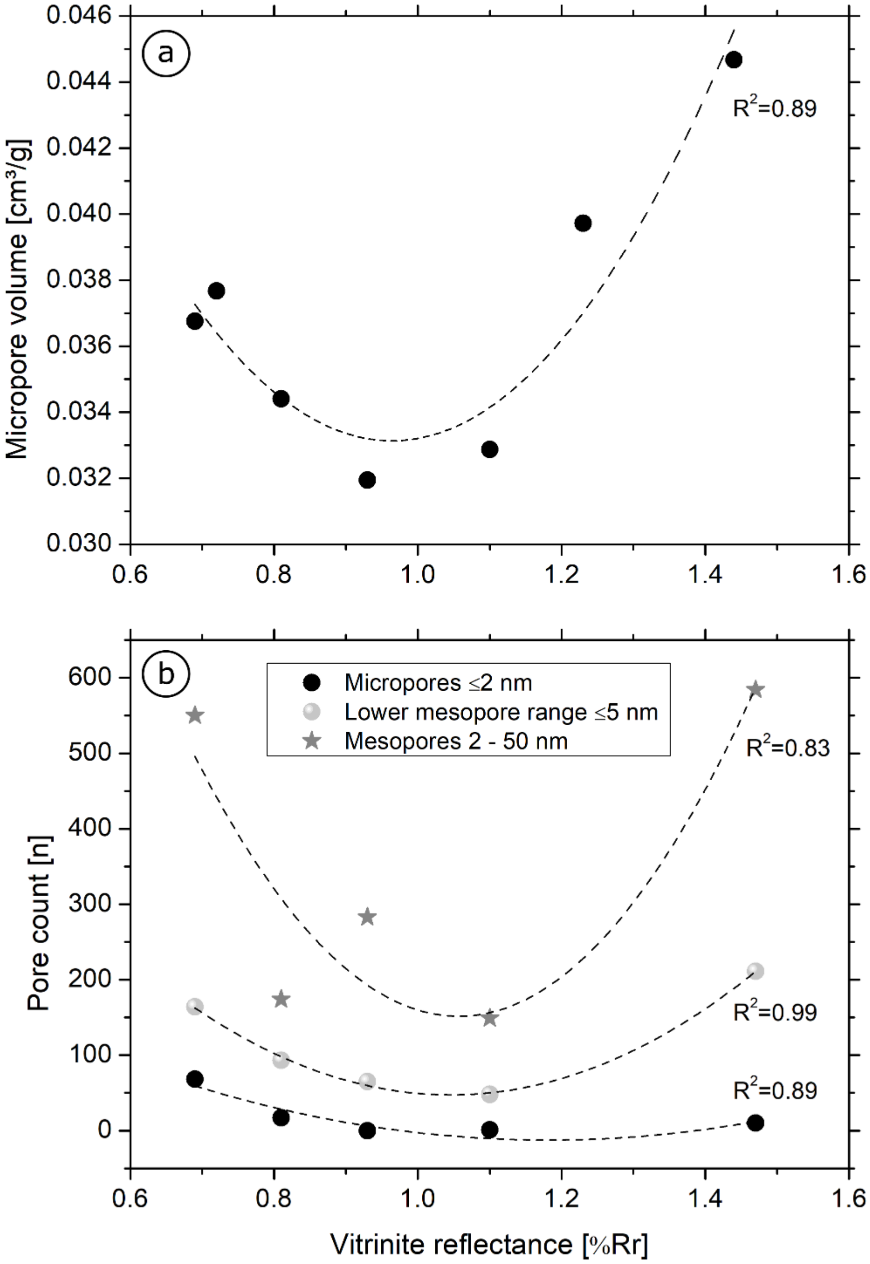

Fig. 13. (a) Dubinin-Astakhov CO_2 micropore volume plottet versus the vitrinite reflectance. (b) TEM pore counts obtained from different pore size ranges as a function of the vitrinite reflectance. Dashed lines: polynomial fit.

Therefore, pore occlusion might equally affect pore visibility in HRTEM experiments. Apart from this effect, various factors are generally responsible for the limiting comparability of sorption and imaging data, including i) the small vitrinite volumes examined via HRTEM compared to the relatively large bulk sample used for sorption experiments, ii) presence of a closed porosity fraction inaccessible to the adsorbate, iii) influence of varying maceral composition which is averaged out in the bulk sample, as well as iv) analytical limitations in the physisorption-based characterization of poorly ordered and heterogeneous materials (e.g., Marsh, 1986; Thommes et al., 2015).

HRTEM imaging of vitrinite particles revealed various pore structures and spatially heterogeneous pore distributions at all examined maturity stages. As mentioned above, the lowest rank vitrinite (Novogrodovskaya; 0.69%Rr) (Fig. 1) hosts the highest fraction of visible micropores (≤ 2 nm), despite growth of micropores being mainly attributed to gas generation during progressive coalification by many previous studies (Gan et al., 1972; Levine and Tang, 1989; Levine, 1993). Elevated organic S contents (Misch et al., 2016) and associated relatively weak C - S bonds (Orr, 1986; Sinninghe Damsté et al., 1990; Tomić et al., 1995) may have facilitated earlier onset of hydrocarbon generation and structural ordering, as indicated by semi-graphite-like nanoclusters (Fig. 2b). Areas with a spongy texture support an origin related to degasification (Misch et al., 2018a, Misch et al., 2018b, Misch et al., 2019a and references therein). The decreased frequency of visible micro- and mesopores in HRTEM images of vitrinite at 0.81–1.10%Rr might be due to the aforementioned occlusion of pores by early-formed bitumen (Fig. 13b; e.g., Thomas Jr. and Damberger, 1976; Mastalerz et al., 2018 and references therein). Solid bitumen and liquid hydrocarbons are not distinguishable from the surrounding vitrinite matrix by means of HRTEM due to the low material contrast.

Pore connectivity and the resulting ratio of connected vs. isolated pores cannot be easily determined by either petrophysical or imaging methods. Channel-like pores were visualized by HRTEM for several samples indicating presence of a connected matrix pore network with pore throats in the range of mostly <2 nm. Similar channel-like structures are documented by Zhao et al. (2014) for high- and low-volatile bituminous coals. However, pores growing under electron beam irradiation, observed mainly at 1.23%Rr (Bazhanova m3–8) and 1.47%Rr (13-bis l1–2), indicate a considerable proportion of isolated degasification pores. The pore growth might be induced by thermal expansion of a free gas phase (likely methane) under in-situ conditions in the TEM. This interpretation is supported by findings from Alexeev et al. (1999), who estimated ~60% of total pores in Donets Basin coals, which are prone to gas outbursts (Sachsenhofer et al., 2012), being isolated methane-filled degasification pores. The presence of such isolated, methane bearing pores would thus well explain the beam instability of the investigated high maturity samples. Sorption experiments utilizing CH_4 as adsorptive at high-pressure remain the paramount tool to predict the gas storage capacity of a coal seam. The total CH_4 sorption capacity results show a general increase from lower to higher rank, but a clear trend is lacking due to a relative minimum at 1.10%Rr (Fig. 10b), which agrees with the corresponding minima in CO_2 micropore volume and HRTEM pore counts (Fig. 13). The low sorption capacity of Bazhanova coal at 1.10%Rr is in good agreement with the virtual absence of micropores in HRTEM images, generally smaller pore populations obtained by HRTEM, as well as high bitumen index values (Izart et al., 2006), indicating a large fraction of occluded pores as described above. Remaining open pores are mainly in the larger mesopore range, as documented by high BJH mesopore volumes from low-pressure N_2 adsorption. Due to lower surface/area ratios, such relatively large pores are reportedly less relevant to methane storage in coals (Clarkson and Bustin, 1999; Mastalerz et al., 2008; Moore, 2012).

9.4.4 Pore structural impact on mechanical properties of vitrinite

Micromechanical parameters were determined by nanoindentation for most of the investigated samples in a previous study (Vranjes et al., 2018). The obtained maturity trends for reduced elastic modulus (E_r) and hardness (H) of vitrinite were not clear and rather indicated an influence of ash yield on E_r.

However, as displayed in Fig. 14, a clear relationship can be observed between E_r and the HRTEM-visible pore sizes in the ≤ 5 nm range. The polynomial trend suggests that E_r values rise with decreasing equivalent pore diameters. Unlike actual pore sizes, bulk porosity is commonly taken into account for mechanical models, as the relation between Young's modulus and porosity is well studied and given by Gibson and Ashby (1999) based on idealized, low density macroporous cell geometries. However, Esqué-de los Ojos et al. (2016) stated that the influence of pore sizes on mechanical parameters is often overlooked, and various studies show strong material-related dependencies of pore size correlations with Young's moduli, as stiffness and deformation mechanism are based on inherent sub-nanoscale properties and chemical bonding (e.g., Li et al., 2013; Esqué-de los Ojos et al., 2016; Dai et al., 2017; Torres-Sanchez et al., 2018). Smaller pore size enhances the number of pores that can share the load, which consequently leads to the load on a single pore being decreased, resulting in a higher resistance toward deformation during indentation (Li et al., 2013). Applying this concept to the observed E_r trend reveals that the presence of higher mesopore fractions in coals from the peak oil window onwards represent the main control on elastic behavior, while lower maturity coals with abundant micropores maintain a relatively higher E_r despite considerable frequency of pores (see Fig. 14).

However, effects of structural modification of the amorphous organic matrix, as well as the limitation to detect bitumen-occluded pores (which still contribute to mechanical behavior) in petrophysical and imaging studies cannot be easily predicted or accounted for.

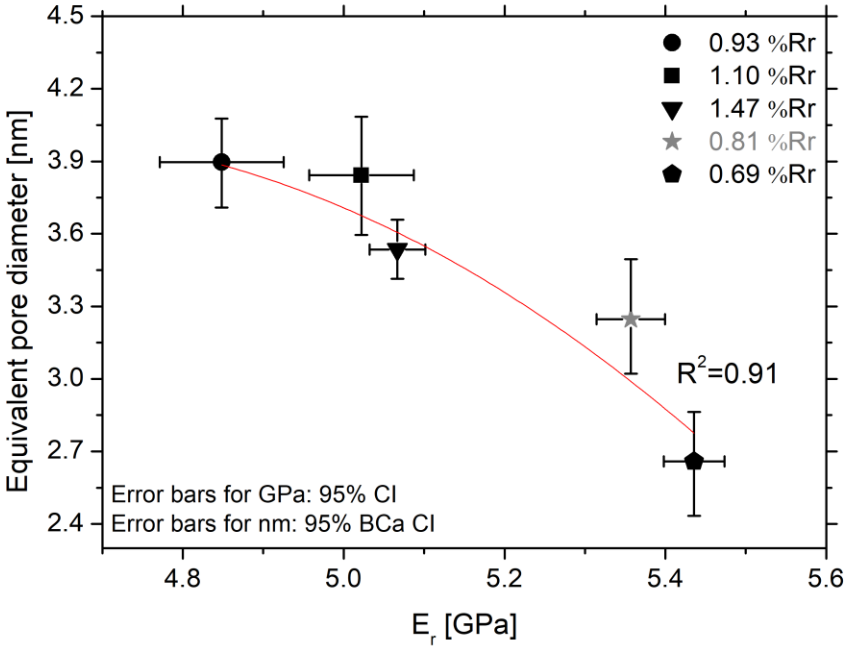

Fig. 14. Average equivalent pore diameter for the size range ≤ 5 nm (Table 2) plotted versus reduced elastic modulus (E_r) from Vranjes et al. (2018). All data were obtained from identical specimens, except for the sample at 0.81%Rr (seam l3–12; highlighted in gray), which was substituted by a comparably mature sample (0.83%Rr; seam n1–2) due to limited availability. (CI – confidence interval; BCa CI – bias-corrected and accelerated confidence interval).

9.5 Conclusion

The pore structure of vitrinite-rich Carboniferous coal samples from the Ukrainian Donets Basin with a maturity interval ranging from 0.69 to 1.47%Rr was investigated at the nanoscale using TEM imaging and gas sorption techniques (low-pressure CO_2 and N_2 adsorption). CH_4 sorption capacity was evaluated by high-pressure sorption experiments, while the structural evolution of organic matter was monitored by Raman spectroscopy. This multianalytical approach improved the understanding of depositional and maturity-related controls on pore characteristics and resulting gas storage capacity.

The key findings are summarized below:

1) The HRTEM evaluation of vitrinite particles at all maturity stages revealed heterogeneous pore characteristics regarding pore sizes, spatial pore distribution and pore morphologies. Absence of HRTEM-visible microporosity at 0.93 and 1.10%Rr indicates a large fraction of occluded pores, which is also supported by CO_2 micropore volumes, lower CH_4 sorption capacity at 1.10%Rr, as well as high bitumen index values.
2) A high micropore fraction observed in vitrinite at 0.69%Rr was interpreted as the result of earlier hydrocarbon generation and devolatilization due to abundant organic sulphur.
3) Higher ordering and presence of semi-graphite-like domains in the sample at 0.69%Rr support considerable influence of sulphur on the kinetics of structural modification.
4) The presence of onion-like carbons in vitrinite at 0.81%Rr indicates formation of these structures at lower temperature.
5) Bazhanova coal at 1.10%Rr is characterized by structural changes documented by Raman spectroscopy, a drop in CH_4 sorption capacity, and a relative minimum of CO_2 micropore volume despite the presence of larger mesopores documented by low-pressure N_2 adsorption. These characteristics are related to the complex superimposition of processes marking the transition from peak oil (maximum pore occlusion) to the early wet gas window (progressive structural ordering).
6) An influence of pore structure on micromechanical properties is documented by the clear correlation of average (HR)TEM pore diameters with previously acquired micromechanical properties. Reduced modulus values at smaller average nanopore diameter are likely a result of more efficient load distribution and resulting greater deformation resistance.

References

Alexeev, A.D., Vasilenko, T.A., Ulyanova, E.V., 1999. Closed porosity in fossil coals. Fuel 78, 635–638.

Barrett, E.P., Joyner, L.G., Halenda, P.P., 1951. The determination of pore volume and area distributions in porous substances. I. Computations from nitrogen isotherms. J. Am. Chem. Soc. 73, 373–380.

Beny-Bassez, C., Rouzaud, J.N., 1985. Characterization of carbonaceous materials by correlated electron and optical microscopy and Raman microspectrometry. Scan. Electron Microsc. 1, 119–132.

Bertier, P., Schweinar, K., Stanjek, H., Ghanizadeh, A., Clarkson, C.R., Busch, A., Kampman, N., Prinz, D., Amann-Hildenbrand, A., Krooss, B.M., Pipich, V., 2016. On the use and abuse of N_2 physisorption for the characterization of the pore structure of shales. In: Clay Minerals Society, Workshop Lectures Series. 21. pp. 151–161.

Beyssac, O., Rouzaud, J.N., Goffé, B., Brunet, F., Chopin, C., 2002. Graphitization in a high-pressure, low-temperature metamorphic gradient: a Raman microspectroscopy and HRTEM study. Contrib. Mineral. Petrol. 143, 19–31.

Beyssac, O., Goffé, B., Petitet, J.P., Froigneux, E., Moreau, M., Rouzaud, J.N., 2003. On the characterization of disordered and heterogeneous carbonaceous materials by Raman spectroscopy. Spectrochim. Acta A 59, 2267–2276.

Binoy, S., Boruah, R.K., Gogoi, P.R., 2009. A X-ray diffraction analysis on graphene layers of Assam coal. J. Chem. Sci. 121, 103–106.

Bonijoly, M., Oberlin, M., Oberlin, A., 1982. A possible mechanism for natural graphite formation. Int. J. Coal Geol. 1, 283–312.

Busch, A., Han, F., Magill, C.R., 2019. Paleofloral dependence of coal methane sorption capacity. Int. J. Coal Geol. 211, 2019.

Bustin, R.M., Clarkson, C.R., 1998. Geological controls on coalbed methane reservoir capacity and gas content. Int. J. Coal Geol. 38, 3–26.

Bustin, R.M., Ross, J.V., Rouzaud, J.N., 1995. Mechanisms of graphite formation from kerogen: experimental evidence. Int. J. Coal Geol. 28, 1–36.

Chalmers, G.R.L., Bustin, R.M., 2007. On the effects of petrographic composition on coalbed methane sorption. Int. J. Coal Geol. 69, 288–304.

Clarkson, C.R., Bustin, R.M., 1996. Variation in micropore capacity and size distribution with composition in bituminous coal of the Western Canadian Sedimentary Basin: implications for coalbed methane potential. Fuel 75, 1483–1498.

Clarkson, C.R., Bustin, R.M., 1999. The effect of pore structure and gas pressure upon the transport properties of coal: a laboratory and modeling study. 1. Isotherms and pore volume distributions. Fuel 78, 1333–1344.

Crosdale, P.J., Beamish, B.B., Valix, M., 1998. Coalbed methane sorption related to coal composition. Int. J. Coal Geol. 35, 147–158.

Dai, J., Singh, J., Yamamoto, N., 2017. The effect of nano pore size and porosity on deformation behaviors of anodic aluminum oxide membranes. In: SAMPE 2017 Conference and Exhibition, May 22–25, Seattle WA.

Dubinin, M.M., 1975. Physical adsorption of gases and vapors in micropores. Prog. Surf. Membr. Sci. 9, 1–70.

Dubinin, M.M., Radushkevich, L.V., 1947. The equation of the characteristic curve of the activated charcoal. In: Proceedings of the Academy of Sciences of the USSR. 55. pp. 331–337.

Efron, B., 1987. Better bootstrap confidence intervals. J. Am. Stat. Assoc. 82, 171–185.

Esqué-de los Ojos, D., Pellicer, E., Sort, J., 2016. The influence of pore size on the indentation behavior of metallic nanoporous materials: a molecular dynamics study. Materials 9, 355.

Faiz, M.M., Aziz, N.I., Hutton, A.C., Jones, B.G., 1992. Porosity and gas sorption capacity of some eastern Australian coals in relation to coal rank and composition. In: Proceedings of the Symposium Coalbed Methane Research and Development, Townsville, Australia, pp. 9–20.

Friedel, R.A., Carlson, G.L., 1972. Difficult carbonaceous materials and their infra-red and Raman spectra. Reassignments for coal spectra. Fuel 51, 194–198.

Gan, H., Nandi, S.P., Walter Jr., P.L., 1972. Nature of porosity in American coals. Fuel 51, 272–277.

Gasparik, M., Ghanizadeh, A., Bertier, P., Gensterblum, Y., Bouw, S., Krooss, B.M., 2012. High-pressure methane sorption isotherms of black shales from the Netherlands. Energy Fuel 26, 4995–5004.

Gasparik, M., Ghanizadeh, A., Gensterblum, Y., Krooss, B.M., 2013. “Multi-temperature” method for high-pressure sorption measurements on moist shales. Rev. Sci. Instrum. 84, 085116.

Gasparik, M., Bertier, P., Gensterblum, Y., Ghanizadeh, A., Krooss, B.M., Littke, R., 2014. Geological controls on the methane storage capacity in organic-rich shales. Int. J.Coal Geol. 123, 34–51.

Gibson, L.J., Ashby, M.F., 1999. Cellular Solids. Structures and Properties, 2nd ed. Cambridge University Press, Cambridge, UK (532 pp).

Gray, I., 1987. Reservoir engineering in coal seams. Part I. The physical process of gas storage and movement in coal seams. SPE Reserv. Eng. 2, 28–34.

Guedes, A., Valentim, B., Prieto, A.C., Rodrigues, S., Noronha, F., 2010. Micro-Raman spectroscopy of collotelinite, fusinite and macrinite. Int. J. Coal Geol. 83, 415–422.

Guo, Q., Fink, R., Littke, R., Zieger, L., 2019. Methane sorption behaviour of coals altered by igneous intrusion, South Sumatra Basin. Int. J. Coal Geol. 214, 103250.

Gürdal, G., Yalçın, N.M., 2001. Pore volume and surface area of Carboniferous coals from the Zonguldak basin (NW Turkey) and their variations with rank and maceral composition. Int. J. Coal Geol. 48, 133–144.

Harpalani, S., Chen, G., 1997. Influence of gas production induced volumetric strain on permeability of coal. Geotech. Geol. Eng. 15, 303–325.

Harris, L.A., Yust, C.S., 1976. Transmission electron microscope observations of porosity in coal. Fuel 55, 233–236.

Harris, L.A., Yust, C.S., 1979. The Ultrafine Structure of Coal Determined by Electron Microscopy. 24. American Chemical Society, Division of Fuel Chemistry Preprints, pp. 210–217.

Henry, D.G., Jarvis, I., Gillmore, G., Stephenson, M., Emmings, J., 2018. Assessing low-maturity organic matter in shales using Raman spectroscopy: effects of sample preparation and operating procedure. Int. J. Coal Geol. 191, 135–151.

Henry, D.G., Jarvis, I., Gillmore, G., Stephenson, M., 2019. Raman spectroscopy as a tool to determine the thermal maturity of organic matter: application to sedimentary, metamorphic and structural geology. Earth Sci. Rev. 198, 102936.

Izart, A., Sachsenhofer, R.F., Privalov, V.A., Elie, M., Panova, E.A., Antsiferov, V.A., Alsaab, D., Rainer, T., Sotirov, A., Zdravkov, A., Zhykalyak, M.V., 2006. Stratigraphic distribution of macerals and biomarkers in the Donets Basin: implications for paleoecology. Paleoclimatology and eustacy. Int. J. Coal Geol. 66, 69–107.

Jaroniec, M., Choma, J., 1989. Theory of gas adsorption on structurally heterogeneous solids and its implication for characterizing activated carbons. In: Thrower, P.A. (Ed.), Chemistry and Physics of Carbon. 22. pp. 197–243.

Kunz, O., Wagner, W., 2012. The GERG-2008 wide-range equation of state for natural gases and other mixtures: an expansion of GERG-2004. J. Chem. Eng. Data 57, 3032–3091.

Kwiecińska, B., Petersen, H.I., 2004. Graphite, semi-graphite, natural coke, and natural char classification—ICCP system. Int. J. Coal Geol. 57, 99–116.

Lamberson, M.N., Bustin, R.M., 1993. Coalbed methane characteristics of gates formation coals, northeastern British Columbia: effect of maceral composition. Am. Assoc. Pet. Geol. Bull. 77, 2062–2076.

Laxminarayana, C., Crosdale, P.J., 1999. Role of coal type and rank on methane sorption characteristics of Bowen Basin, Australia coals. Int. J. Coal Geol. 40, 309–325.

Levine, J.R., 1991. The impact of oil formed during coalification on generation and storage of natural gas in coalbed reservoir systems. In: Proceedings of 1991 Coalbed Methane Symposium, pp. 307–315.

Levine, J.R., 1993. Coalification: the evolution of coal as source rock and reservoir rock for oil and gas. In: Law, B.E., Rice, D.D. (Eds.), Studies in Geology, Hydrocarbons from Coal. 3. American Association of Petroleum Geologists, pp. 1–12.

Levine, J.R., Tang, Y., 1989. Secondary porosity in coal and its relationship to coal metamorphism (Abstract). In: Proceedings, Coal: Formation, Occurrence, and Related Properties, Orleans, France, Paper No. 42.

Li, Z., Yang, L., Li, Y., Yang, Y., Zhou, C., Ding, Y., Zhao, J., Li, Y., 2013. Effects of pore size on the mechanical properties of three-dimensionally ordered macroporous nickel. Mater. Des. 45, 52–55.

Liu, S., Loper, C.R., 1991. The formation of kish graphite. Carbon 29, 547–555. Löhr, S.C., Baruch, E.T., Hall, P.A., Kennedy, M.J., 2015. Is organic pore development in gas shales influenced by the primary porosity and structure of thermally immature organic matter? Org. Geochem. 87, 119–132.

Lu, L., Sahajwalla, V., Kong, C., Harris, D., 2001. Quantitative x-ray diffraction analysis and its application to various coals. Carbon 39, 1821–1833.

Lünsdorf, N.K., 2016. Raman spectroscopy of dispersed vitrinite - Methodical aspects and correlation with reflectance. Int. J. Coal Geol. 153, 75–86.

Lünsdorf, N.K., Lünsdorf, J.O., 2016. Evaluating Raman spectra of carbonaceous matter by automated iterative curve-fitting. Int. J. Coal Geol. 160–161, 51–62.

Mahajan, O.P., Walker Jr., P.L., 1978. Porosity of coal and coal products. In: Karr Jr.C. (Ed.), Analytical Methods for Coal and Coal Products. 1. pp. 125–162.

Manoj, B., 2014. Investigation of nanocrystalline structure in selected carbonaceous materials. Int. J. Miner. Metall. Mater. 21, 940–946.

Manoj, B., Kunjomana, A.G., 2012. Study of stacking structure of amorphous carbon by Xray diffraction technique. Int. J. Electrochem. Sci. 7, 3127–3134.

Marsh, H., 1986. Adsorption methods to study microporosity in coals and carbons – a Critique. Carbon 25, 49–58.

Mastalerz, M., Drobniak, A., Strąpoć, D., Acosta, W.S., Rupp, J., 2008. Variations in pore characteristics in high volatile bituminous coals: Implications for coal bed gas content. Int. J. Coal Geol. 76, 205–216.

Mastalerz, M., Drobniak, A., Stankiewicz, A.B., 2018. Origin, properties, and implications of solid bitumen in source-rock reservoirs: a review. Int. J. Coal Geol. 195, 14–36.

Mathews, J.P., Sharma, A., 2012. The structural alignment of coals and the analogous case of Argonne Upper Freeport. Fuel 95, 19–24.

Misch, D., Gross, D., Huang, Q., Zaccarini, F., Sachsenhofer, R.F., 2016. Light and trace element composition of Carboniferous coals from the Donets Basin (Ukraine): an electronmicroprobe study. Int. J. Coal Geol. 168, 108–118.

Misch, D., Klaver, J., Gross, D., Mayer-Kiener, V., Mendez-Martin, F., Schmatz, J., Sachsenhofer, R.F., 2018a. Factors controlling shale microstructure and porosity: a case study on Upper Visean Rudov Beds from the Ukrainian Dniepr-Donets Basin. AAPG Bull. 102, 2629–2654.

Misch, D., Klaver, J., Gross, D., Rustamov, J., Sachsenhofer, R.F., Schmatz, J., Urai, J.L., 2018b. Pore space characteristics of Upper Visean "Rudov Beds": insights from BIBSEM and organic geochemical investigations. Geol. Soc. Lond. Spec. Publ. 484.

Misch, D., Gross, D., Hawranek, G., Horsfield, B., Klaver, J., Mendez-Martin, F., Urai, J.L., Vranjes-Wessely, S., Sachsenhofer, R.F., Schmatz, J., Li, J., Zou, C., 2019a. Solid bitumen in shales: petrographic characteristics and implications for reservoir characterization. Int. J. Coal Geol. 205, 14–31.

Misch, D., Riedl, F., Liu, B., Horsfield, B., Ziegs, V., Mendez-Martin, F., Vranjes-Wessely, S., Sachsenhofer, R.F., 2019b. Petrographic and sorption-based characterization of bituminous organic matter in the Mandal Formation, Central Graben (Norway). Int. J. Coal Geol. 211, 103229.

Moore, T.A., 2012. Coalbed methane: a review. Int. J. Coal Geol. 101, 36–81.

Niekerk, D.V., Mathews, J.P., 2010. Molecular representations of Permian-aged vitrinite rich and inertinite-rich South African coals. Fuel 89, 73–82.

Oberlin, A., 1984. Carbonization and graphitization. Carbon 22, 521–541.

Oberlin, A., Boulmier, J.L., Durand, B., 1974. Electron microscope investigation of the structure of naturally and artificially metamorphosed kerogen. Geochim. Cosmochim. Acta 38, 647–650.

Okolo, G.N., Everson, R.C., Neomagus, H.W.J.P., Roberts, M.J., Sakurovs, R., 2015a. Comparing the porosity and surface areas of coal as measured by gas adsorption, mercury Intrusion and SAXS techniques. Fuel 141, 293–304.

Okolo, G.N., Neomagus, H.W.J.P., Everson, R.C., Roberts, M.J., Bunt, J.R., Sakurovs, R., Mathews, J.P., 2015b. Chemical-structural properties of South African bituminous coals: Insights from wide angle XRD-carbon fraction analysis. ATR-FTIR, solid state 13C NMR and HRTEM techniques. Fuel 158, 779–792.

Orr, W.L., 1986. Kerogen/asphaltene/sulfur relationships in sulfur-rich Monterey oils. Org. Geochem. 10, 499–516.

Pan, J., Zhao, Y., Hou, Q., Jin, Y., 2015. Nanoscale pores in coal related to coal rank and deformation structures. Transp. Porous Media 107, 543–554.

Parkash, S., Chakrabartty, S.K., 1986. Microporosity in Alberta Plains coals. Int. J. Coal Geol. 6, 55–70.

Potgieter-Vermaak, S., Maledi, N., Wagner, N., Van Heerden, J.H., Van Grieken, R., Potgieter, J.H., 2011. Raman spectroscopy for the analysis of coal: a review. J. Raman Spectrosc. 42, 123–129.

Prinz, D., Pyckhout-Hintzen, W., Littke, R., 2004. Development of the meso- and macroporous structure of coals with rank as analysed with small angle neutron scattering and adsorption experiments. Fuel 83, 547–556.

Rantitsch, G., Lämmerer, W., Fisslthaler, E., Mitsche, S., Kaltenböck, H., 2016. On the discrimination of semi-graphite and graphite by Raman spectroscopy. Int. J. Coal Geol. 159, 48–56.

Rice, D.D., 1993. Composition and origins of coalbed gas. In: Law, B.E., Rice, D.D. (Eds.), Studies in Geology, Hydrocarbons from Coal. 38. American Association of Petroleum Geologists, pp. 159–185.

Rodrigues, C.F., Lemos de Sousa, M.J., 2002. The measurement of coal porosity with different gases. Int. J. Coal Geol. 48, 245–251.

Romero-Sarmiento, M.-F., Rouzaud, J.N., Bernard, S., Deldicque, D., Thomas, M., Littke, R., 2014. Evolution of Barnett Shale organic carbon structure and nanostructure with increasing maturation. Org. Geochem. 71, 7–16.

Sachsenhofer, R.F., Privalov, V.A., Izart, A., Elie, M., Kortensky, J., Panova, E.A., Sotirov, A., Zhykalyak, M.V., 2003. Petrography and geochemistry of Carboniferous coal seams in the Donets Basin (Ukraine): implications for paleoecology. Int. J. Coal Geol. 55, 225–259.

Sachsenhofer, R.F., Privalov, V.A., Panova, E.A., 2012. Basin evolution and coal geology of the Donets Basin (Ukraine, Russia): an overview. Int. J. Coal Geol. 89, 26–40.

Sakurovs, R., Koval, L., Grigore, M., Sokolova, A., Ruppert, L.F., Melnichenko, Y.B., 2018. Nanometre-sized pores in coal: Variations between coal basins and coal origin. Int. J. Coal Geol. 186, 126–134.

Sharma, A., Kyotani, T., Tomita, A., 2000a. Direct observation of layered structure of coals by transmission electron microscope. Energy Fuel 14, 515–516.

Sharma, A., Kyotani, T., Tomita, A., 2000b. Direct observation of raw coals in lattice fringe mode using high-resolution transmission electron microscopy. Energy Fuel 14, 1219–1225.

Sing, K.S.W., Everett, D.H., Haul, R.A.W., Moscou, L., Pierotti, R.A., Rouquerol, J., Siemieniewska, T., 1985. Reporting physisorption data for gas/solid systems with special reference to the determination of surface area and porosity. Pure Appl. Chem. 57, 603–619.

Sinninghe Damsté, J.S., Eglinton, T.I., Rijpstra, W.I.C., de Leeuw, J.W., 1990. Characterization of organically bound sulfur in high-molecular-weight sedimentary organic matter using flash pyrolysis and Raney Ni desulfurization. In: Orr, W.L., White, C.M. (Eds.), Geochemistry of Sulfur in Fossil, Fuels, ACS Symposium Series. 429. pp. 486–528.

Thomas Jr., J., Damberger, H.H., 1976. Internal surface area, moisture content, and porosity of Illinois coals: Variations with coal rank. Illinois State Geological Survey 493 (38 p).

Thommes, M., Kaneko, K., Neimark, A.V., Olivier, J.P., Rodriguez-Reinoso, F., Rouquerol, J., Sing, K.S.W., 2015. Physisorption of gases. With special reference to the evaluation of surface area and pore size distribution (IUPAC Technical Report). Pure Appl. Chem. 87, 1051–1069.

Tomić, J., Behar, F., Vandenbroucke, M., Tang, Y., 1995. Artificial maturation of a Monterey kerogen (Type II-S) in a closed system and comparison with Type II kerogen: Implications on the fate of sulfur. Org. Geochem. 23, 647–660.

Torres-Sanchez, C., McLaughlin, J., Bonallo, R.J., 2018. Effect of pore size, morphology and orientation on the bulk stiffness of a porous Ti35Nb4Sn alloy. J. Mater. Eng. Perform. 27, 2899–2909.

Tuinstra, F., Koenig, J.L., 1970. Raman spectrum of graphite. J. Chem. Phys. 53, 1126–1130.

Vranjes, S., Misch, D., Schöberl, T., Kiener, D., Gross, D., Sachsenhofer, R.F., 2018. Nanoindentation study of macerals in coals from the Ukrainian Donets Basin. Adv. Geosci. 45, 73–83.

Wang, S., Pan, J., Ju, Y., Wang, K., Niu, Q., Wang, Z., 2017. The super-micropores in macromolecular structure of tectonically deformed coal using high-resolution transmission electron microscopy. J. Nanosci. Nanotechnol. 17, 6982–6990.

Xu, B., 2008. Prospects and research progress in nano onion-like fullerenes. New Carbon Mater. 23, 289–301.

Zhao, Y., Liu, S., Elsworth, D., Jiang, Y., Zhu, J., 2014. Pore structure characterization of coal by synchrotron small-angle x-ray scattering and transmission electron. Energy Fuel 28, 3704–3711.

Ziegs, V., Horsfield, B., Skeie, J.E., Rinna, J., 2017. Petroleum retention in the Mandal Formation, Central Graben, Norway. Mar. Pet. Geol. 83, 195–214.

Appendix

Supplementary files included with publication II

Appendix A:

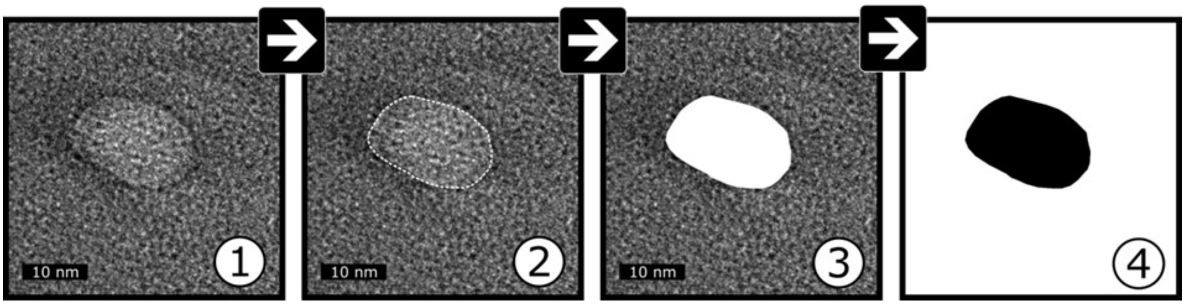

Fig. A1: Work flow for pore structure evaluation via ImageJ: (1) Pore identification based on contrast difference and/or the detection of sharp pore edges. (2) Tracing of pore edges via the polygon selection tool. (3) Highlighting of pore areas. (4) Binarisation by grey-scale thresholding and further calculation of pore structural parameters.

Appendix B:

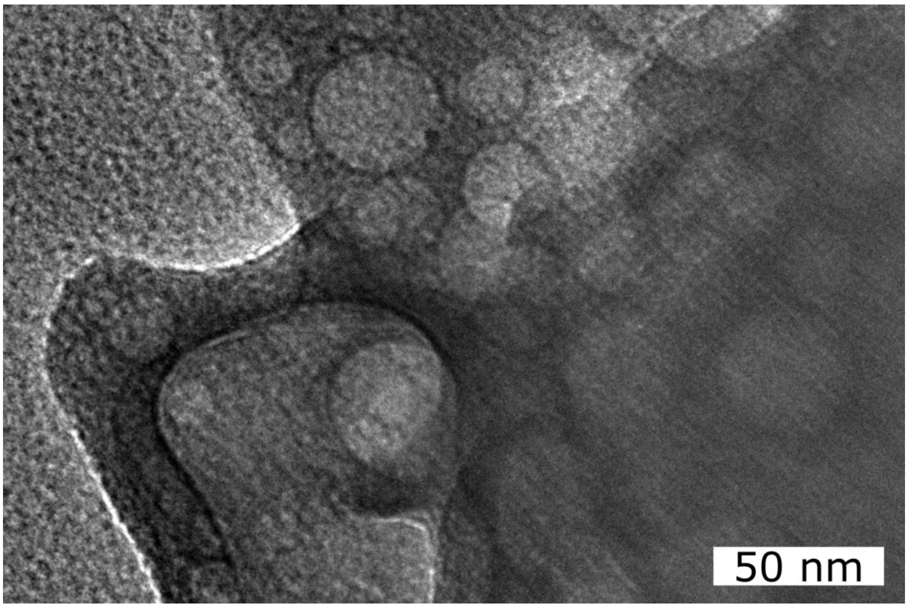

Fig. B1: Growing bubble-like pores in a telovitrinite particle at 1.47 %Rr (13bis l1-2). The growth starts within seconds under electron beam irradiation. The pores merge to form larger, irregular macropore structures with progressing growth.

Appendix C:

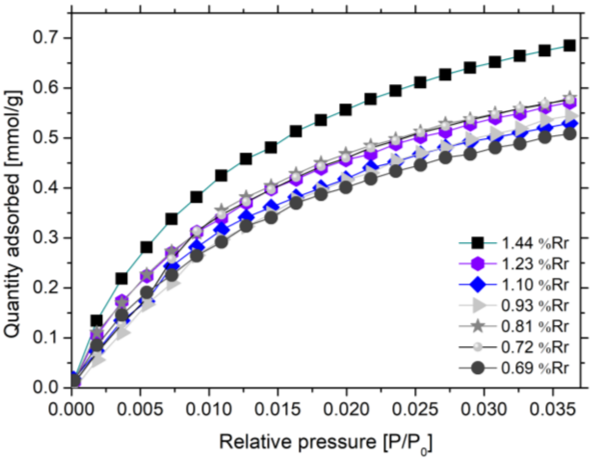

Fig. C1: Low pressure CO$_2$ physisorption isotherms from coal samples at different maturity.

Appendix D:

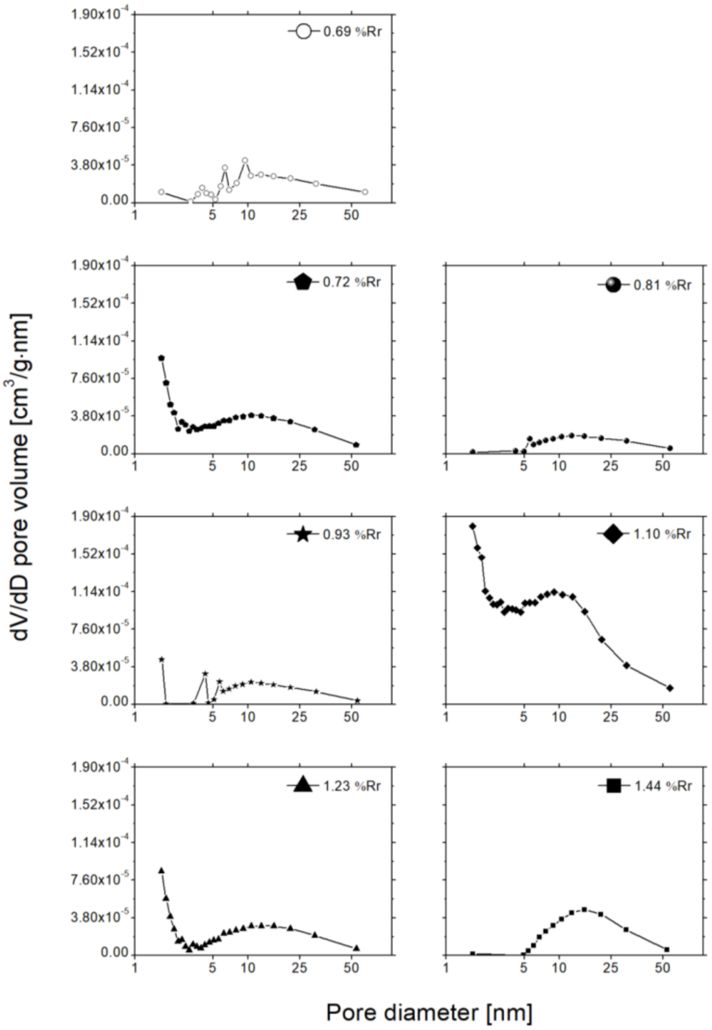

Fig. D1: BJH mesopore size distribution obtained from N$_2$ adsorption branches.

10 Publication III

High-speed nanoindentation mapping of organic matter-rich rocks: A critical evaluation by correlative imaging and machine learning data analysis

Vranjes-Wessely, S.[1, 2], Misch, D.[1], Kiener, D.[2], Cordill, M.J.[3], Frese, N.[4], Beyer, A.[4], Horsfield, B.[5], Wang, C.[6], Sachsenhofer, R.F.[1]

Int. J. Coal Geol., under review

1)Department of Applied Geosciences and Geophysics, Montanuniversität Leoben, A-8700 Leoben, Austria

2)Department of Materials Science, Montanuniversität Leoben, A-8700 Leoben, Austria

3)Erich Schmid Institute of Materials Science, Austrian Academy of Sciences, A-8700 Leoben, Austria

4)Faculty of Physics, Bielefeld University, D-33615 Bielefeld, Germany

5)GEOS4 GmbH, D-14552 Michendorf, Germany

6)State Key Laboratory of Biogeology and Environmental Geology, China University of Geosciences, Beijing, China

Abstract

Nanoindentation is a valuable tool, which enables insights into the material properties of natural, highly inhomogeneous composite materials such as shales and organic matter-rich rocks. However, the inherent complexity of these rocks and its constituents complicates the extraction of representative material parameters such as the reduced elastic modulus (E_r) and hardness (H) for organic matter (OM) via nanoindentation. The present study aims to extract the representative H and E_r values for OM within an over-mature sample set from the Chinese Songliao Basin and evaluate influencing factors of the resulting parameters. This was realized by means of high-speed nanoindentation mapping in combination with comprehensive optical and high resolution-imaging methods. Further, the results were processed by the unsupervised machine learning algorithm *k*-means clustering in order to evaluate representative E_r and H results. These indicate that the main impacting factor on the mechanical properties is inherently present in such heterogeneous matter. In fact, surrounding, underlying and inherent mineral matter lead to confinement effects and enhanced E_r values, whereas cracks and pores are responsible for a lowered stiffness. The enhanced accuracy archived by a large data set facilitated machine learning approach not only improves further modeling attempts but also allows insights of impacting geological processes on the material parameter and general understanding of mechanical behavior of OM in rock formations. Thus, the presented multimethod approach promotes a fast and reliable assessment of representative material parameters from organic rock constituents.

10.1 Introduction

In 1992, Oliver and Pharr developed an instrumented nanoindentation method which enables local mechanical material characterization at the micro- and nanometer scales (Oliver and Pharr, 2004, 1992). Since then, this technique has been continuously developed for use with a wide range of engineering (Hay, 2009; Oliver and Pharr, 2010, 2004) and biological materials (Ebenstein and Pruitt, 2006; Oyen, 2013). In recent years, nanoindentation also caught the attention of geoscientists, as the small, required testing volume allows the small-scale analysis of highly inhomogeneous rock samples with complex composition and microstructure (e.g., Goldsby et al., 2004; Kranjc et al., 2016; Ma et al., 2020; Shukla et al., 2015; Thom and Goldsby, 2019; Yin and Zhang, 2011; Zhu et al., 2007). These include for example fine-grained and OM-rich sedimentary rocks (e.g., shales) (e.g., Abedi et al., 2016; Bennett et al., 2015; Bobko and Ulm, 2008; Kumar et al., 2012b, 2015; Liu et al., 2016, 2018; Luo et al., 2020; Ma et al., 2020; Misch et al., 2018; Shukla et al., 2013; Ulm and Abousleiman, 2006; Yang et al., 2020), which not only play a vital role as fossil energy carriers given sufficient thermal maturity, but also represent potential disposal sites for nuclear waste material and may act as geological barriers in the attempt to store anthropogenic CO_2 or H_2 in abandoned hydrocarbon fields (Charlet et al., 2017).

Generally, the mechanical parameters (hardness *H*, elastic modulus *E*) of shales are measured by static or dynamic macro-scaled experiments on drill cores or core plugs. However, while drill core material from exploration wells is generally limited, shale intervals are rarely cored and typically show a poor core recovery and preservation (Kumar et al., 2012b; Liu et al., 2016). Furthermore, the standard macroscopic testing routines often exhibit low precision and inconsistency of results in case of shales, and material properties for the individual constituents (e.g., the organic fraction) cannot be derived either. OM occurs as finely dispersed, layered or network-like varieties and often fills intergranular voids within the rock matrix. This reportedly has a large influence on the mechanical and fracture behavior of the overall rock (Khatibi et al., 2018; Kumar et al., 2015; Sayers, 2013), and therefore on the hydrocarbon producibility and wellbore stability. As a consequence, various studies targeted the nanomechanical characterization of OM in shales using atomic force microscopy (AFM) (Ahmadov et al., 2009; Eliyahu et al., 2015; Emmanuel et al., 2016; Yang et al., 2017) or nanoindentation (Alstadt et al., 2016; Kumar et al., 2012a; Mashhadian et al., 2018; Zeszotarski et al., 2004; Zhao et al., 2020). The large discrepancies between results from both techniques highlight the difficulties in the acquisition of representative material parameters for different OM types. Eliyahu et. al (2015) concluded in their AFM study that the elastic modulus of OM is heterogenous at the nanoscale and that the spatial resolution is a key factor for a full mechanical characterization. However, even at the nanoscale, a precise determination is challenging due to the complex nature of OM particles embedded within the mineral matrix. Individual indents are not sufficient for a holistic mechanical characterization of OM, since the individual particles are restrained by the surrounding fine grained matrix minerals, which affects the nanoindentation response and complicates the mechanical characterization. In contrast, the nanoindentation mapping technique (Bobko and Ulm, 2008; Constantinides et al., 2006; Liu et al., 2018; Luo et al., 2020; Ulm and Abousleiman, 2006) offers great advantages compared to the traditional, individual point measurements. In nanoindentation mapping, material parameters can be obtained statistically from defined equal-distance grids placed on the selected surface areas of interest (e.g., Constantinides et al., 2006; Liu et al., 2018; Ulm and Abousleiman, 2006). By doing so, inherent property variations are captured and interface effects are visualized.

In order to test the suitability of high-speed nanoindentation mapping for the determination of phase-specific micromechanical properties in shales and other OM-rich rocks, various types of OM within a set of samples from a deep exploration well (Songke-2 Well; SK-2) in the Chinese Songliao Basin were characterized. As the OM fraction in shales is acceptably the most challenging for mechanical testing (Vranjes et al., 2018 and references therein), this study is intended as a proof-of-concept for nanoindentation mapping of organic matter in fine-grained rocks of any kind. In order to study the influence of microstructural heterogeneities (e.g., pore structure, surface features, micro-texture) on the accuracy of micromechanical data, complementary high-resolution imaging by means of scanning electron microscopy (SEM) and helium ion microscopy (HIM) was conducted. In addition, traditional optical petrography was performed for a clear identification of OM types (kerogen vs. solid bitumen). Cross-correlation between different characterization techniques is a challenge often encountered in shale studies (Hackley et al., 2017). To even enable a spatially-resolved, correlative analysis between the mechanical property maps and the obtained optical and high-resolution SEM and HIM images, a novel, high-precision marking tool was utilized. Analysis grids were applied by a thermally non-invasive femtosecond laser (Pfeifenberger et al., 2017). This approach vastly improved data correlation and interpretation. Finally, the micromechanical testing results were further processed by the unsupervised machine learning algorithm *k*-means clustering (Hartigan and Wong, 1979). The implementation of the *k*-means clustering served to evaluate phase heterogeneities and grain boundary effects and to identify outliers caused by unavoidable measurement errors in heterogeneous structures. Various material science studies already demonstrated the potential of machine learning application for material characterization as *k*-means proved to be a successful tool for data deconvolution and analysis of nanoindentation results (e.g., Konstantopoulos et al., 2020; Koumoulos et al., 2019; Vignesh et al., 2019). The established work flow for a reliable determination of phase-specific micromechanical properties should improve the quality of input data in digital rock modelling and prediction of rock mechanical changes during subsurface processes such as hydraulic fracturing. Furthermore, using this procedure thermal maturity effects on OM properties are discussed.

10.2 Material and Methods

10.2.1 Sample material

The examined samples (table 1) were recovered from the SK-2 well drilled during the Deep Continental Scientific Drilling Engineering Project in the Songliao Basin of Northeastern China. The Songliao Basin covers an area of 260 000 km2 and is known as one of the most productive oil and gas provinces worldwide (Desheng et al., 1995). Remarkably, the SK-2 well was the deepest continental scientific drilling project accomplished by any Asian nation (Hou et al., 2018). A focus of the project was the exploration of deep unconventional gas resources within the Cretaceous succession. The studied samples were recovered from the Lower Cretaceous Shahezi Formation. These rocks are characterized by a high total organic carbon content (TOC) and extensive occurrences of shale gas (Hou et al., 2018). As the samples originate from great burial depths (3376 – 4426 m), the present OM is thermally mature. The vitrinite reflectance values range between 1.33 and 2.23 %Rr corresponding to the oil phase-out to dry gas transition (Noah et al., 2020). A detailed regional geological overview is given in Hou et al. (2018).

Table 1: Overview of burial depths, vitrinite reflectance values and geochemical bulk parameters (by Noah et al. (2020) for the studied samples. (*VR* – vitrinite reflectance, *TOC* – total organic carbon, *S1* – free hydrocarbons (HC), T_{max} – Rock Eval temperature of maximum HC-generation, *HI* – hydrogen index).

		by Noah et al. (2020)				
Name	Depth m	*VR* %Rr	*TOC* wt%	*S1* mg *HC*/g	T_{max} °C	*HI* mg *HC*/g *TOC*
SK2	3376	1.33	20.4	0.55	510	56
SK5	3466	1.68	2.42	0.06	533	22
SK9	3586	1.96	7.37	0.05	552	25
SK10	3616	1.89	1.85	0.02	557	17
SK12	3676	2.00	1.31	0.01	555	16
SK18	3866	2.23	4.43	0.02	579	11
SK37	4426	2.21	1.10	0.03	597	5

10.2.2 Sample preparation and laser-marking

Prior to experiments, the selected SK-2 samples were embedded into epoxy resin perpendicular to their bedding plane and mechanically polished (final polishing step: 0.05 µm). The OM within the polished sections were then examined and defined by optical microscopy using Leica DM 4500P and DM 4P microscopes, both under oil immersion (DM 4P) and at air in dry state (DM 4500P). Representative areas of interest were selected and subsequently marked with a femtosecond laser-machined grid in order to facilitate nanoindentation and subsequent correlated examination of the OM particles (figure 1). The suitability of this ultrashort pulsed laser ablation technique for use with heat-sensitive specimen such as biomaterials is well documented and the thermal overprint is considered negligible (Jakob et al., 2017; Pfeifenberger et al., 2019, 2017). The parameter set used during grid preparation with the Auriga Laser platform (Carl Zeiss) is summarized in table 2.

Table 2: Femtosecond laser parameter set for grid preparation (E_f – fluence, *f* – pulse repetition rate, *D* – divisor, *vs* – scan speed, λ – Laser wavelength, *L* – line repetitions, *S* – scan repetitions, for further information see Pfeifenberger et al. (2017).

E_f J cm^{-2}	*f* kHz	*D*	*vs* mm/s	λ nm	*L*	*S*
0.49 – 1.15	50	15 – 50	1	515	1	15 – 25

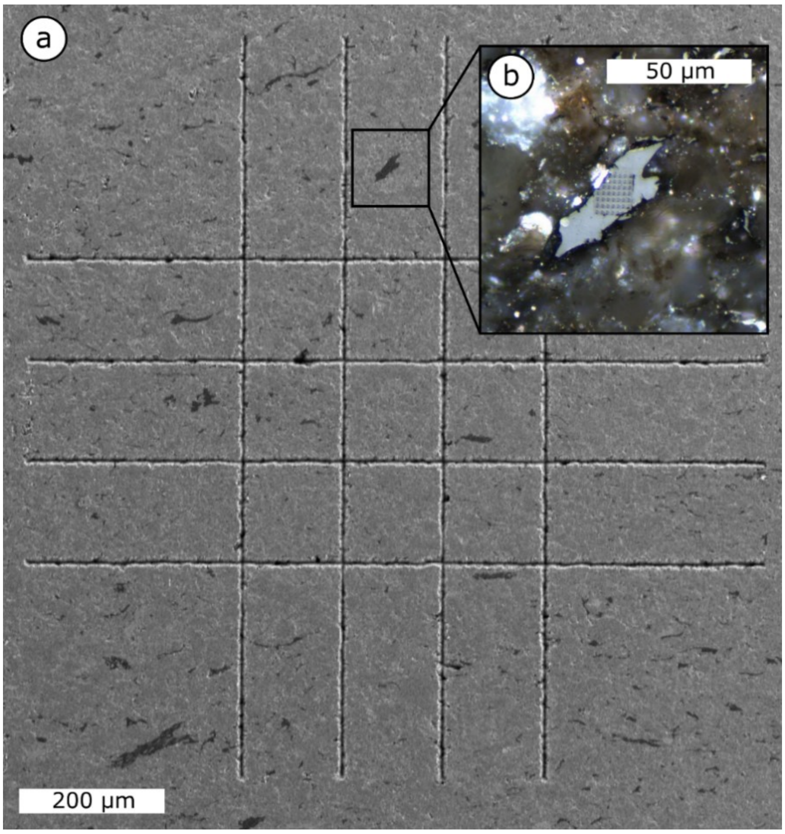

Figure 1: (a) SEM overview image of a femtosecond laser marked surface of sample SK10, facilitating the (b) optical examination of specific OM particles as well as the nanoindentation mapping of the latter (nanoindentation grid is visible on the surface of the OM particle).

10.2.3 High-speed nanoindentation mapping

The nanoindentation property mapping was performed using a Hysitron TS 77 Select (Bruker) equipped with a Cube Corner diamond tip. A fused silica standard was used for the calibration of the Cube Corner area function following the Oliver-Pharr method (Oliver and Pharr, 1992). Prior and subsequently to property mapping, scanning probe microscopy (SPM) was performed to identify and document undisturbed areas for representative measurements (all SPM images visualized with Gwyddion; see Nečas and Klapetek, (2012)). The individual indents were performed in load-controlled mode with a trapezoidal loading profile (0.5 s loading, 1 s hold, 0.5 s unloading) and a maximum load of 800 µN. Equivalent to conventional nanoindentation tests, hardness (*H*) and reduced elastic modulus (E_r) are calculated based on the evaluation of the resulting load-displacement curves after the Oliver-Pharr method (Oliver and Pharr, 1992). The elastic Young´s modulus differs from the reduced elastic modulus mainly in that the deformation of the diamond tip during the testing procedure is considered. For soft material such as OM, the Young´s modulus and reduced elastic modulus values are alike, as the deformation of the Cube Corner tip by the soft substrate is negligible. Consequently, in this study Er will be used as mechanical parameter of OM. For each sample, at least five maps with variable arrays (up to 9 x 9 indents) were placed on OM particles visible within the femtosecond laser grids. The array spacing was 2 – 3 µm between the individual measurement spots in order to fully resolve property heterogeneities while still avoiding interference between the indents. An indent-depth ratio of 10 was recommended for a wide variety of materials (Sudharshan Phani and Oliver, 2019). Due to the ductile nature of OM resulting in indentation depths of ~700 nm, this ratio is not reached for the studied samples, as such a wide spacing would hinder the correct acquisition of true property heterogeneities. A careful examination of all load-displacement curves for unwanted effects of plastic pre-deformation did not reveal any signs of measurement-induced bias.

10.2.4 Scanning electron microscopy

Scanning electron microscopy was performed using a Tescan Clara field emission (FE)-SEM equipped with backscattered (BSE) and secondary electron (SE) detectors as well as an energy-dispersive X-ray (EDX) detector (Oxford Instruments). For the correlative study, SEM images were acquired in two steps. At first, imaging was done on the mechanically polished and laser-marked blocks for an overview of measurement spots. These investigations were performed on the uncoated specimen surfaces at low electron energy (< 5 kV) in order to maintain the undisturbed state for further introduced HIM imaging. In the second stage (after nanoindentation and HIM), representative sub-specimens were cut from the mechanically polished blocks and further prepared with a Hitachi ArBlade 5000 broad ion beam (BIB) preparation system with an Ar beam at 8 kV for 2 h. BIB-SEM is nowadays a standard technique in the characterization of OM nanostructures, allowing for the investigation of artefact-free microstructures and particularly porosity associated with OM at high resolution (Hackley et al., 2020, 2021).

10.2.5 Helium ion microscopy

HIM was carried out using an Orion Plus microscope (Carl Zeiss). HIM images were acquired at an acceleration voltage of 34.5 – 36.1 kV and a beam current set at 0.3 – 2.9 pA. The sample surface was not sputtered with a conductive layer to prevent artifacts that may result from such coating. Thus, an electron flood gun was used during imaging in order to stabilize charging of the specimen surface. HIM has the capability to provide SE images at ultra-high resolution, and offers a surface sensitivity and contrast superior to conventional

FE-SEM. Furthermore, it is particularly efficient in the use with materials constituted of low-mass elements such as carbon, as the helium ion beam has a lower interaction volume compared to an electron beam (Bell, 2009; Hlawacek et al., 2014; Scipioni et al., 2009; Sijbrandij et al., 2010; Ward et al., 2006). Due to the very limited availability of such microscopes, relatively few studies have used HIM for the characterization of OM in mudstones and shales (Cavanaugh and Walls, 2016; Hackley et al., 2021; Huang et al., 2020; King et al., 2015; Wang et al., 2020; Wu et al., 2020). Nevertheless, HIM proved to be a valuable complementary method in this study due to its ability to achieve highest resolutions on mechanically polished and native samples, as well as to better resolve topographic features compared to SEM (Cavanaugh and Walls, 2016; King et al., 2015).

10.2.6 *k*-means clustering

k-means is a machine learning algorithm for cluster analysis. It identifies the local means of a given number of cluster subsets *k* within a larger dataset. After predefinition of the number of clusters *k*, the algorithm optimizes the clustering by assigning each data point to the cluster with the closest mean central value (“centroid”) (Hartigan and Wong, 1979). The clustering is then iteratively improved until the average sum of squared distances amid points of each cluster is minimized and no further point shifts occur (Hartigan and Wong, 1979). *k*-means clustering is classified as unsupervised machine learning since labeling, categorization and training of the data set prior to analysis is not required. However, the number of clusters needs to be predetermined by the users, either by knowledge of the phases within the sample (Vignesh et al., 2019) or by the implementation of heuristic methods for quality validation of clustering. These approaches include for instance the elbow method (Thorndike, 1953) and the silhouette method (Rousseeuw, 1987). After specifying the number of clusters, the initial centroids are chosen uniformly at random, then recomputed iteratively until the minimal within-cluster sum of squares is reached. However, this random initialization might affect overall clustering performance for certain data sets. Implementation of the *k*-means++ algorithm (Arthur and Vassilvitskii, 2007) is an approach for improved cluster initialization and was adopted for this study. Property mapping results for H and E_r were clustered using the Python machine learning library scikit-learn (Pedregosa et al., 2011) in order to improve local mean values for the individual mapped phases and to detect boundary effects. The clustering algorithm was applied twice on each data set: (1) the tested minerals were separated from the OM within the map in order to (2) evaluate the different mechanical domains within the OM particles.

10.3 Results

10.3.1 Optical and SEM petrography

Optical and scanning electron microscopy revealed strongly differing textural characteristics of the imaged OM. The following description is ordered according to increasing burial depth and thermal maturity (see table 1).

SK2

Sample SK2 (1.33 %Rr) consists of silicified fossil wood (vitrinite) (figure 2a). The well-preserved cell structure, which is also visible in the BSE overview image (figure 2b), indicates that silicification occurred during early diagenesis. Due to the dilution by microcrystalline quartz (chert), the TOC content is only ~20 wt% (table 1). Nevertheless, SK2 is the most organic matter-rich of all studied samples. The elongated OM parts appear structureless and non-porous at higher BIB-SEM resolution (figure 2c). The chert exhibits occasional pores, which are frequently located in proximity to vitrinite (figure 2d). However, overall porosity is limited in the microcrystalline quartz as well.

SK5

Sample SK5 (1.68 %Rr) hosts solid bitumen filling intergranular pore space in-between coarse quartz and carbonate grains (figure 3a). The solid bitumen forms a continuous OM network throughout the imaged specimen (figures 3b-e). In contrast to sample SK2, vitrinite is largely absent. OM pores are generally rare but occur occasionally within the solid bitumen groundmass or at interfaces with matrix minerals (figures 3d, e). These pores exhibit either rounded or angular morphologies (figures 3b-d).

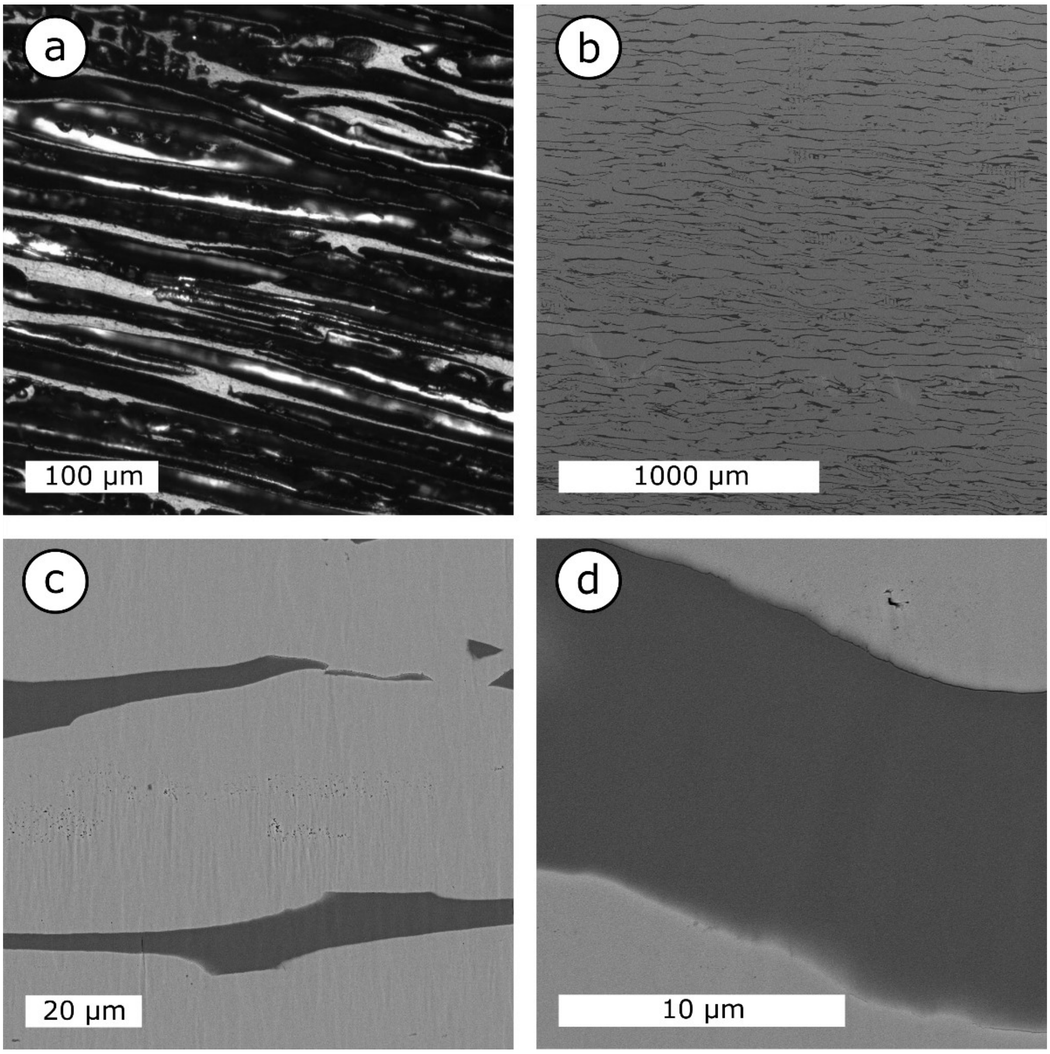

Figure 2: (a) Optical image (oil immersion) of sample SK2 showing silicified fossil wood (vitrinite). (b) BSE overview image of the BIB polished area. (c, d) Non-porous OM within chert exhibiting occasional pores.

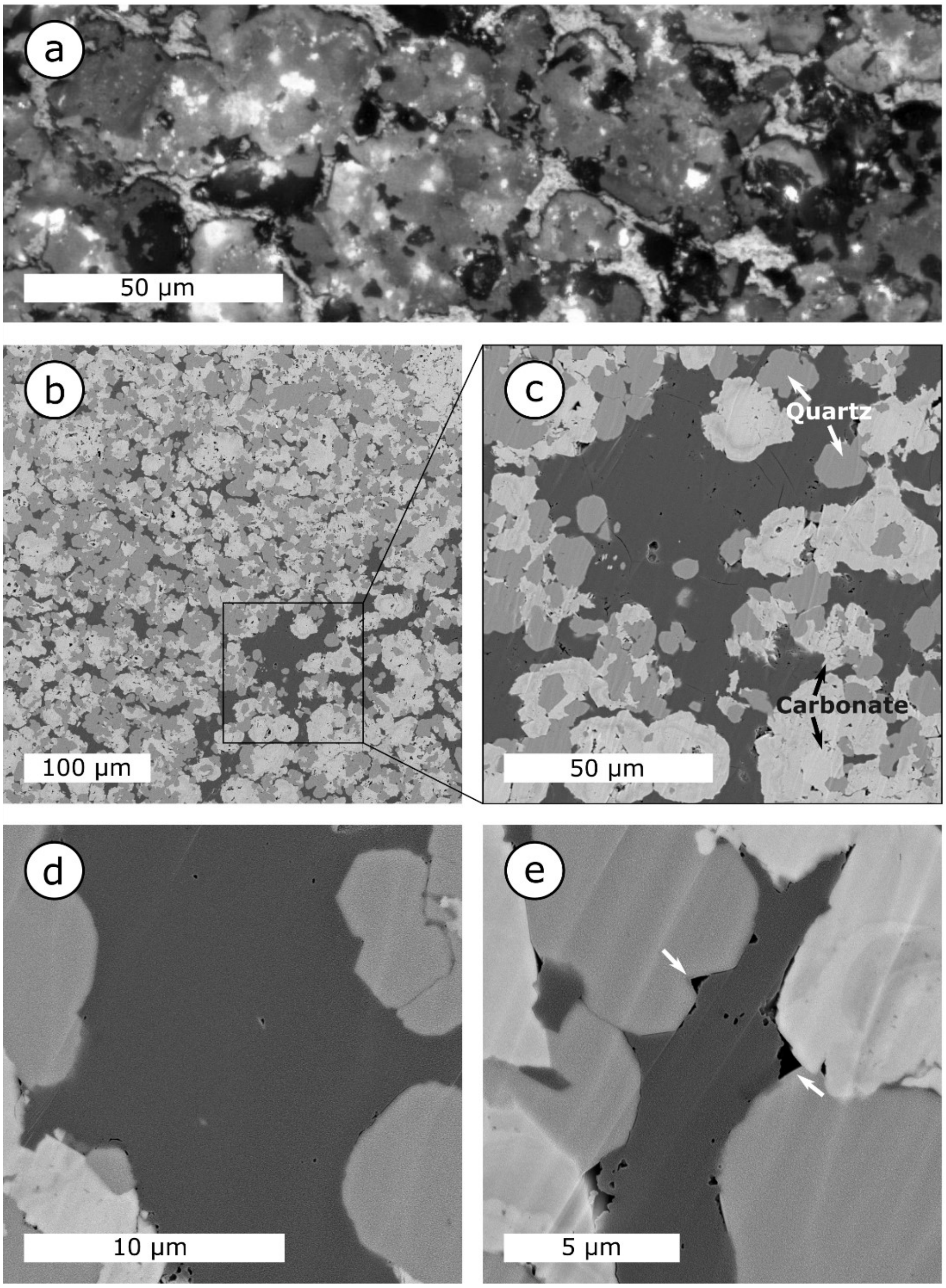

Figure 3: (a) Photomicrograph of the solid bitumen network in sample SK5. (b) BIB-SEM overview of the OM network filling intergranular voids in-between carbonate and quartz grains; the detail image in (c) shows porous bitumen hosting round and angular pores and quartz inclusions. (d) Solid bitumen containing few pores. (e) Porous solid bitumen with large interface pores (white arrows).

SK9, SK10, SK12

Samples SK9 (1.96 %Rr), SK10 (1.89 %Rr) and SK12 (2.00 %Rr) show similar thermal maturity and OM types, SK9 is richest in OM (7.37 wt% TOC; table 1). In contrast to the comparable OM composition, the mineral matrix texture of the three samples varies considerably (figures 4b, 5b, 6b). Sample SK9 is characterized by large grains and considerable carbonate cementation (figure 4b), while SK10 is dominated by fine-grained clay minerals (figure 5b). Sample SK12 is characterized by a clay matrix similar to sample SK10, but coarse grains and carbonate-cemented areas are also present (figure 6b).

All three samples are characterized by relatively large, disseminated vitrinite particles, while inertinite occurs in smaller amounts (figures 4a, 5a, 6a). BIB-SEM images reveal that the structureless OM is non-porous (figures 4c, d, 5c, 6d). However, particularly in samples SK10 and SK12, OM particles with significant amounts of finely dispersed mineral inclusions were observed (figures 5d, 6c).

SK18, SK37

Samples SK18 (2.23 %Rr) and SK37 (2.21 %Rr) are the specimen with the highest maturity. Sample SK18 (4.4 wt% TOC; table 1) contains a shaly part with detrital vitrinite particles and an approximately 5 mm thick vitrinite layer.

One large detrital vitrinite particle in the shaly part contains abundant authigenic quartz (figures 7a-c), while authigenic quartz in the thick vitrinite band occurs less frequently (figures 7d, e). Vitrinite contains occasional pores, which are mostly angular and occur in irregularly distributed clusters mostly adjacent to the authigenic minerals.

Sample SK37 has the lowest TOC content of all studied samples and consequently exhibits a low amount of OM particles (figures 8a, c). The observed OM is mostly vitrinite and inertinite, embedded into a clay mineral-rich matrix (figures 8c, d). Only few vitrinite particles host minor internal porosity (figure 8b).

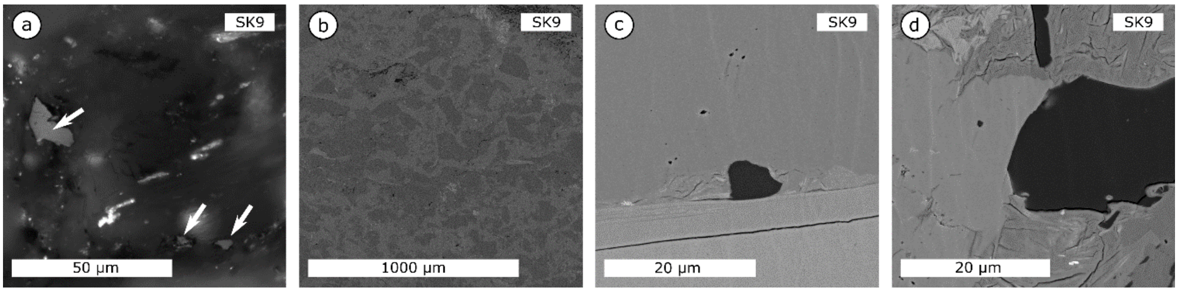

Figure 4: Photomicrograph and BIB-SEM images of sample SK9. (a) Optical image of vitrinite particles (white arrows) under oil immersion. (b) BIB-SEM overview of the rock texture. (c, d) BIB-SEM images of non-porous OM particles.

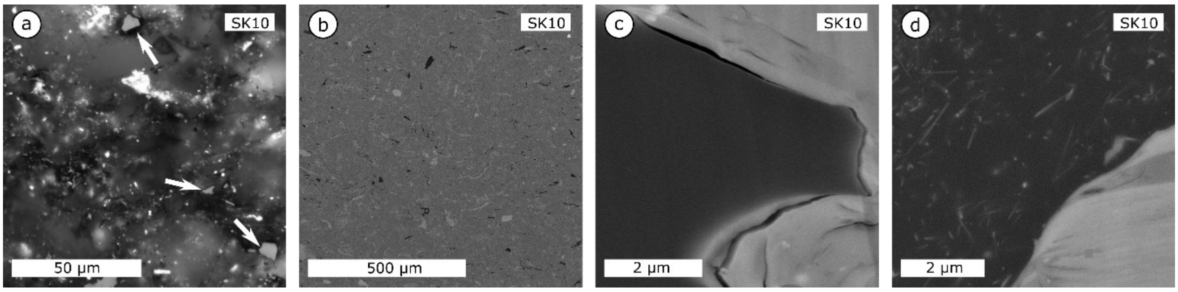

Figure 5: (a) Optical image of vitrinite particles (white arrows) under oil immersion within sample SK10. BIB-SEM images displaying an (b) overview of the mineral fabric, (c) non-porous OM particle and (d) OM hosting finely dispersed mineral inclusions.

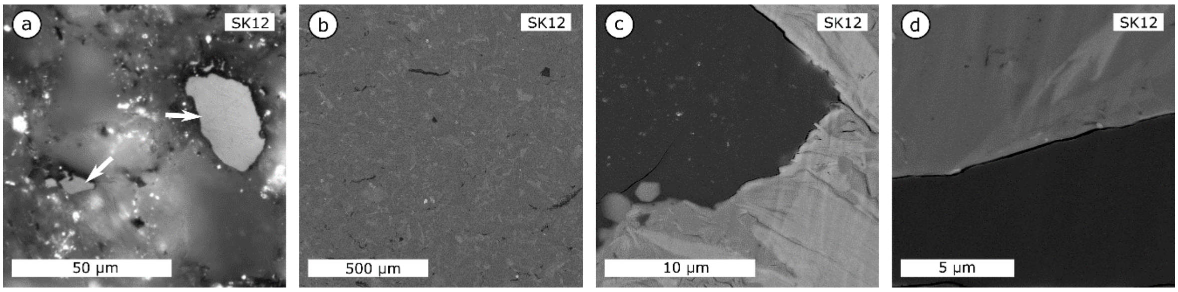

Figure 6: (a) Photomicrograph displaying vitrinite particles in sample SK12. (b) BIB-SEM overview of the sample. (c) OM particle containing mineral matter. (d) BIB-SEM images of a non-porous OM particle of sample.

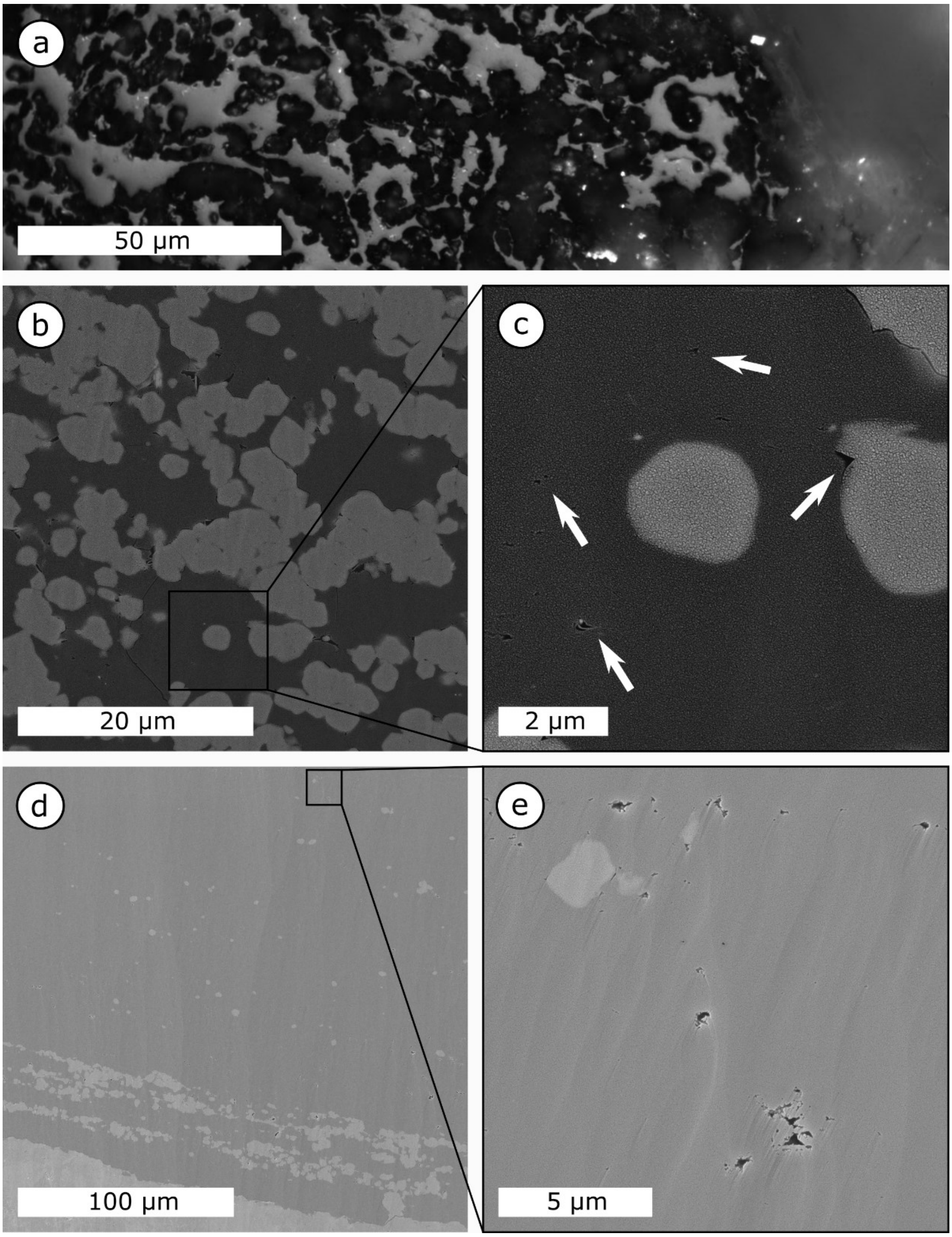

Figure 7: (a) Optical image (oil immersion) of dispersed vitrinite in sample SK18. (b, c) Porous vitrinite hosting authigenic minerals (predominately quartz). (d, e) BIB-SEM overview and detail images of a broad vitrinite layer hosting angular pores and quartz inclusions.

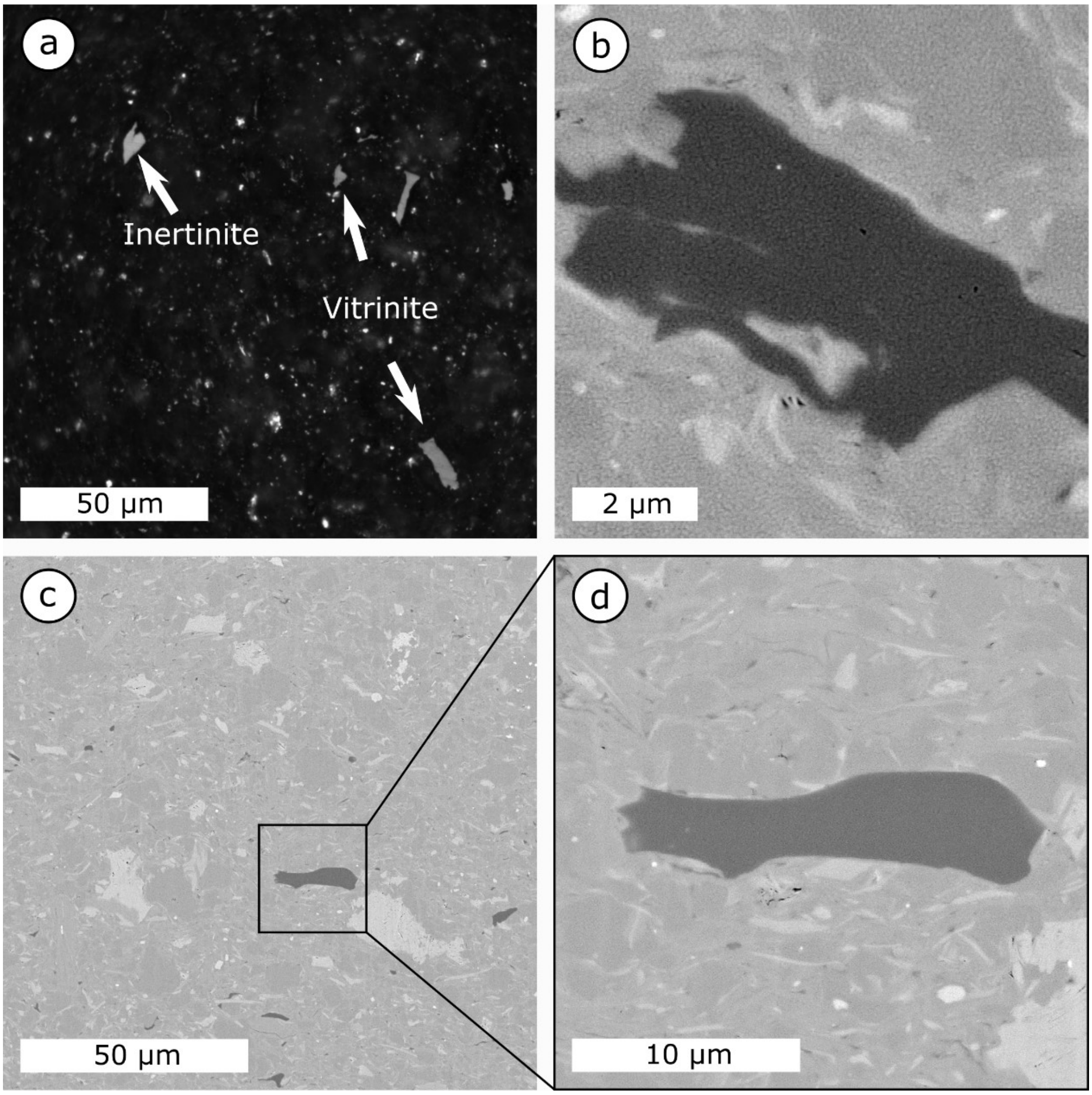

Figure 8: (a) Photomicrograph of vitrinite and inertinite particles within sample SK37. (b) BSE image of an OM particle exhibiting few internal pores. (c) BIB-SEM overview of SK37 documenting the OM-lean texture with only few isolated OM particles. (d) Detail image of a non-porous OM particle interpreted as vitrinite.

10.3.2 High-speed nanoindentation mapping and correlative high-resolution imaging

High-speed nanoindentation mapping was performed for 38 selected OM particles within the investigated samples (table 1). The average E_r and H values of all maps are summarized in table 3. Additionally, the total average of all maps from each sample were calculated for a better comparability (table 4).

Seven maps have been collected for vitrinite in sample SK2 (1.33 %Rr). The average E_r values for these maps range from 5.85 to 6.77 GPa, resulting in the highest total average E_r value of all samples (6.26±1.09 GPa). The average H values vary from 0.46 to 0.57 GPa. Variations within a particle and the respective load-displacement curves are displayed for a vitrinite grain (map 5) in SK2 (figure 9).

Five maps representing solid bitumen have been obtained for sample SK5 (1.68 %Rr). Both average E_r (4.98 – 5.81 GPa) and H (0.40 – 0.48 GPa) values are lower than for vitrinite in SK2.

Five vitrinite particles have been selected from sample SK9 (1.96 %Rr). Four of these particles (maps 2–5) show relatively low average E_r (3.86 – 4.68 GPa) and H values (0.36 – 0.48 GPa). The lowest deviation of E_r and H values within a map in SK9 were obtained from a relatively large and homogenous vitrinite particle (map 5) (figure 10). Only map 1 exhibits a higher average E_r of 6.65±1.71 GPa, likely due to abundant authigenic minerals. However, in contrast to E_r, the average H value of map 1 (0.46±0.04 GPa) is within the range of the other vitrinite particles.

Five vitrinite particles (maps 1–5) in sample SK10 (1.89 %Rr) are characterized by higher average E_r (4.83 – 6.37 GPa) and H values (0.47 – 0.57 GPa) compared to SK9, despite of the comparable thermal maturity of both samples.

The average E_r obtained from five vitrinite particles (maps 1–5) in sample SK12 at 2.00 %Rr are rather uniform (4.83 – 4.98 GPa). They range above the values determined in SK9, but lower compared to SK10. The average H values span from 0.39 to 0.54 GPa.

Six vitrinite maps were obtained for sample SK18 (2.23 %Rr). Maps 1 to 3 represent the approximately 5-mm-thick coaly layer described above and display relatively consistent average E_r (4.64 – 4.91 GPa) and H values (0.54 – 0.57 GPa). Maps 4 to 6 represent vitrinite particles in the shaly part of the sample and show slightly higher E_r values (5.04 – 7.52 GPa). The high E_r value of map 4 is also characterized by a large standard deviation (7.52±3.8 GPa). H values in the range of 0.50 to 0.57 GPa are similar to those in the coaly layer.

One inertinite (map 1) and four vitrinite particles (maps 2-5) have been investigated in sample SK37 (2.21 %Rr). Average E_r and H values obtained from the vitrinite maps range from 4.67 to 5.61 GPa and from 0.49 to 0.56 GPa, respectively. The inertinite particle exhibits an average E_r of 5.65±2.7 GPa which is similar to that of vitrinite in map 4, but its H value (0.64±0.09 GPa) is the highest of all investigated OM particles.

The total average E_r and H values obtained of each sample (average of all maps per sample, see table 4) are plotted versus vitrinite reflectance in figure 9. The plot reveals a large variation for the mechanical parameters, in particular for E_r (see figure 11). Based on the average E_r (table 4), a slight decrease with increasing maturity can be observed. In contrast, the average H values vary from 0.40 to 0.56 GPa without a systematic depth or maturity trend.

Figure 12a shows an optical micrograph of a vitrinite particle in sample SK12 (map 4). The correlative HIM image of the OM particle is presented in figure 12b. Nanoindents are shown in the SPM surface map (figure 12c). HIM imaging revealed that the SPM surface scans affected the soft maceral surface (figure 12d, detail in D). Corresponding property maps for E_r and H are displayed in figure 12e, where the highest E_r values are observed in proximity to mineral grain boundaries.

A further example of nanoindentation property maps of a vitrinite particle (map 5; table 3) in sample SK12 is shown in figure 13. HIM imaging enables a more detailed view on individual indents and cracks within the OM (see inset in figure 13a). The property maps exhibit local variability of E_r and (at a lesser degree) H values and in combination with the correlative imaging it appears, that these are often obtained in proximity to surrounding mineral matrix and cracks (figures 13 a, b). E_r values of OM adjacent to minerals are typically enhanced, but reduced values were also obtained (figure 13b). In order to correct for such unwanted boundary and topography effects, *k*-means clustering was executed on the micromechanical dataset in order to obtain “representative” OM properties (see explanations below).

Table 3: Average E_r and H results and corresponding standard deviation (SD) values calculated based on the total number of indents per particle (n) for each map. (v – vitrinite, sb – solid bitumen, i – inertinite).

		Average					
Name	Map	E_r GPa	SD GPa	H GPa	SD GPa	OM type	n
SK2	1	6.77	1.71	0.46	0.05	v	33
	2	5.90	0.80	0.46	0.05	v	40
	3	6.46	1.26	0.45	0.05	v	14
	4	5.85	0.45	0.55	0.02	v	30
	5	6.11	0.97	0.57	0.03	v	58
	6	6.01	0.25	0.53	0.03	v	24
	7	6.76	1.15	0.53	0.06	v	41
SK5	1	5.81	1.51	0.47	0.09	sb	21
	2	5.09	0.52	0.40	0.02	sb	46
	3	4.98	0.73	0.44	0.04	sb	40
	4	5.50	1.35	0.48	0.06	sb	34
	5	5.33	1.27	0.41	0.02	sb	15
SK9	1	6.65	1.71	0.46	0.04	v	24
	2	4.30	0.57	0.48	0.04	v	33
	3	4.28	0.80	0.36	0.02	v	35
	4	4.68	1.12	0.46	0.07	v	18
	5	3.86	0.17	0.36	0.02	v	48
SK10	1	5.20	0.81	0.51	0.02	v	30
	2	5.41	0.44	0.53	0.02	v	39
	3	4.83	0.43	0.47	0.02	v	66
	4	5.72	1.49	0.54	0.05	v	28
	5	6.34	1.76	0.49	0.05	v	27
SK12	1	4.85	1.26	0.47	0.06	v	41
	2	4.98	0.77	0.39	0.03	v	44
	3	4.94	0.57	0.48	0.02	v	37
	4	4.94	1.09	0.49	0.03	v	62
	5	4.83	0.64	0.54	0.03	v	24
SK18	1	4.91	0.18	0.57	0.02	v	22
	2	4.76	0.18	0.55	0.01	v	47
	3	4.64	0.38	0.54	0.01	v	21
	4	7.52	3.80	0.57	0.15	v	22
	5	5.06	0.56	0.56	0.06	v	36
	6	5.04	0.92	0.50	0.03	v	32
SK37	1	5.65	2.70	0.64	0.09	i	39
	2	4.67	1.01	0.52	0.08	v	50
	3	4.98	1.23	0.59	0.05	v	25
	4	5.61	2.07	0.56	0.04	v	25
	5	4.69	0.83	0.49	0.03	v	25

Table 4: Average E_r and H values for each sample. (v – vitrinite, sb – solid bitumen, i – inertinite).

			Average						
Name	Depth m	*VR* %Rr	E_r GPa	SD GPa	*H* GPa	SD GPa	Indents *n*	OM types	Comments
SK2	3376	1.33	6.26	1.09	0.52	0.06	240	v	all data included
SK5	3466	1.68	5.27	1.06	0.44	0.06	156	sb	all data included
SK9	3586	1.96	4.19	0.70	0.40	0.06	134	v	outlier excluded (map 1)
			4.56	1.27	0.41	0.07	158	v	all data included
SK10	3616	1.89	5.35	1.10	0.50	0.04	190	v	all data included
SK12	3676	2.00	4.92	0.94	0.47	0.06	208	v	all data included
SK18	3866	2.23	5.21	1.64	0.55	0.06	180	v	all data included
			4.77	0.26	0.56	0.02	90	v	coaly part (maps 1, 2, 3)
			5.65	2.23	0.54	0.09	90	v	shaly part (maps 4, 5, 6)
SK37	4426	2.21	5.09	1.78	0.56	0.09	164	v, i	all data included

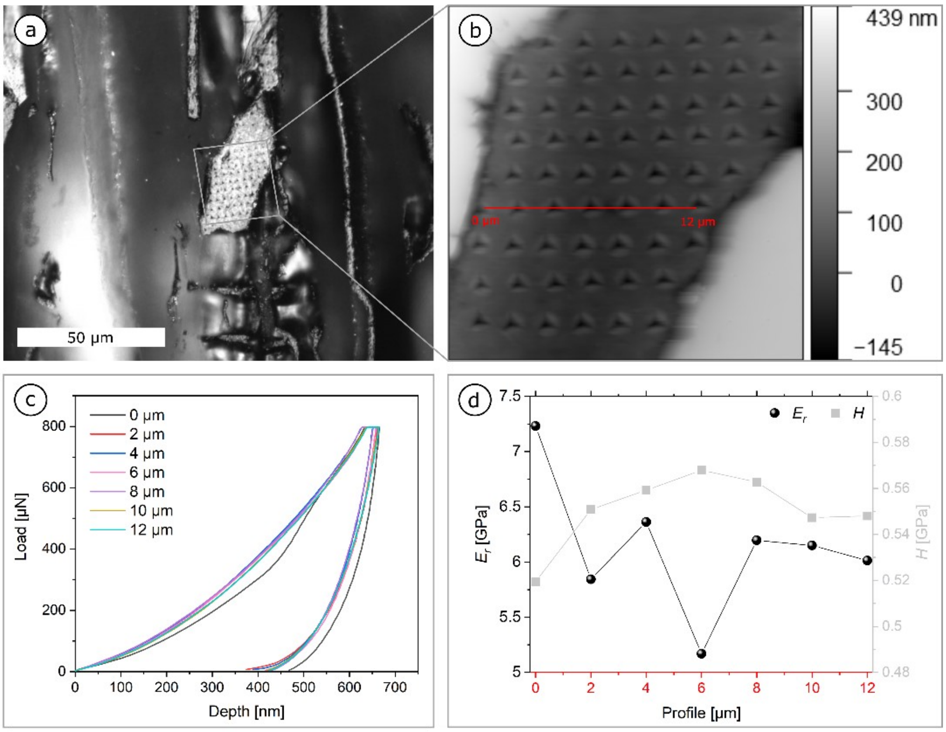

Figure 9: (a) Photomicrograph of a vitrinite particle (map 5) in sample SK2 under oil-immersion and (b) the corresponding SPM image (20x20 µm scan). (c) Nanoindentation load-displacement curves measured along the profile (red line in (b)) resulting in the respective E_r and H values shown in (d).

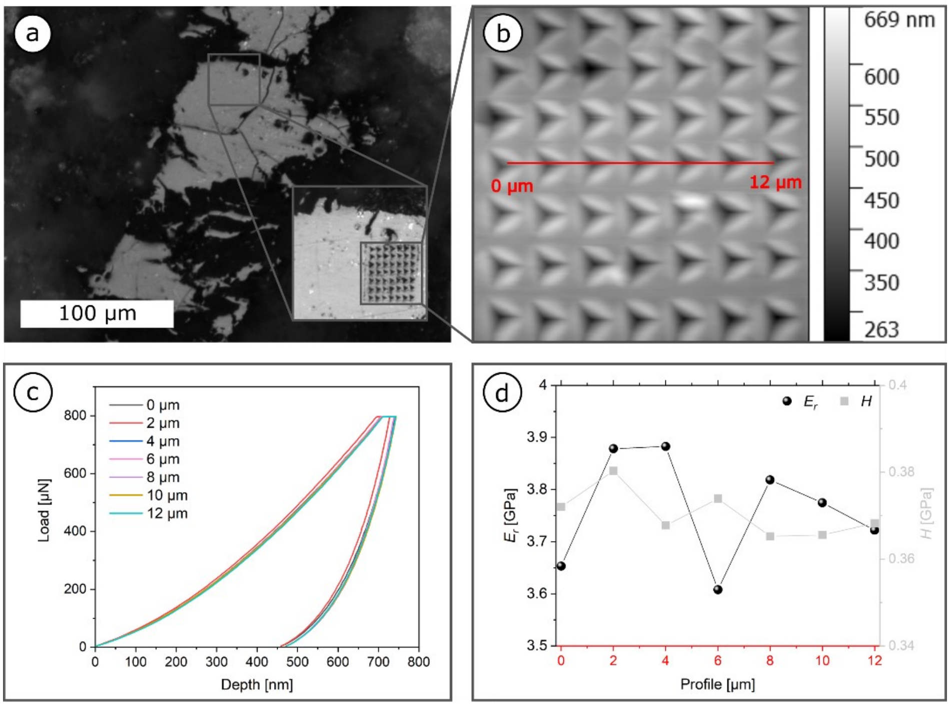

Figure 10: Optical micrograph of a large vitrinite particle (map 5) in sample SK9 under oil immersion pre and after indention mapping (see inset). (b) SPM surface map (15x15 µm) of the tested area and (c) load-displacement curves obtained along the profile (red line in (b)). (d) Slight variations of E_r and *H* along measured profile (red line in (b)).

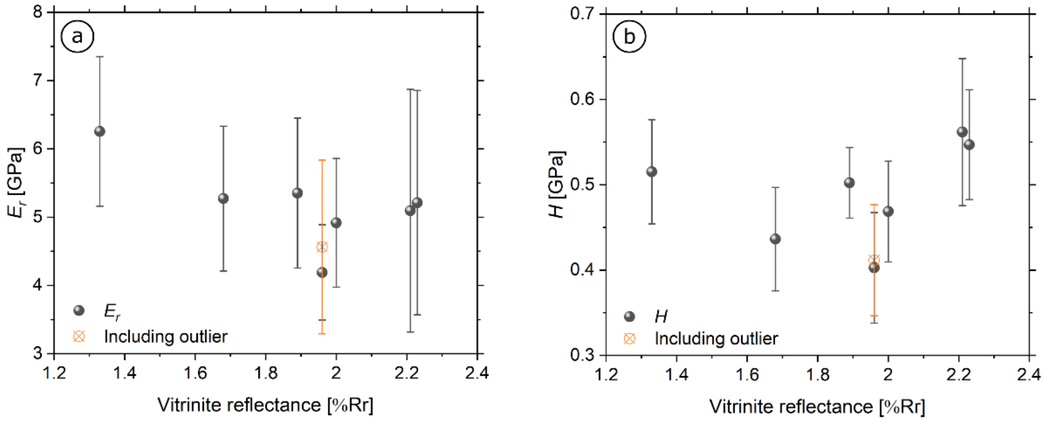

Figure 11: Averages for (a) E_r and (b) *H* versus vitrinite reflectance (see table 3).

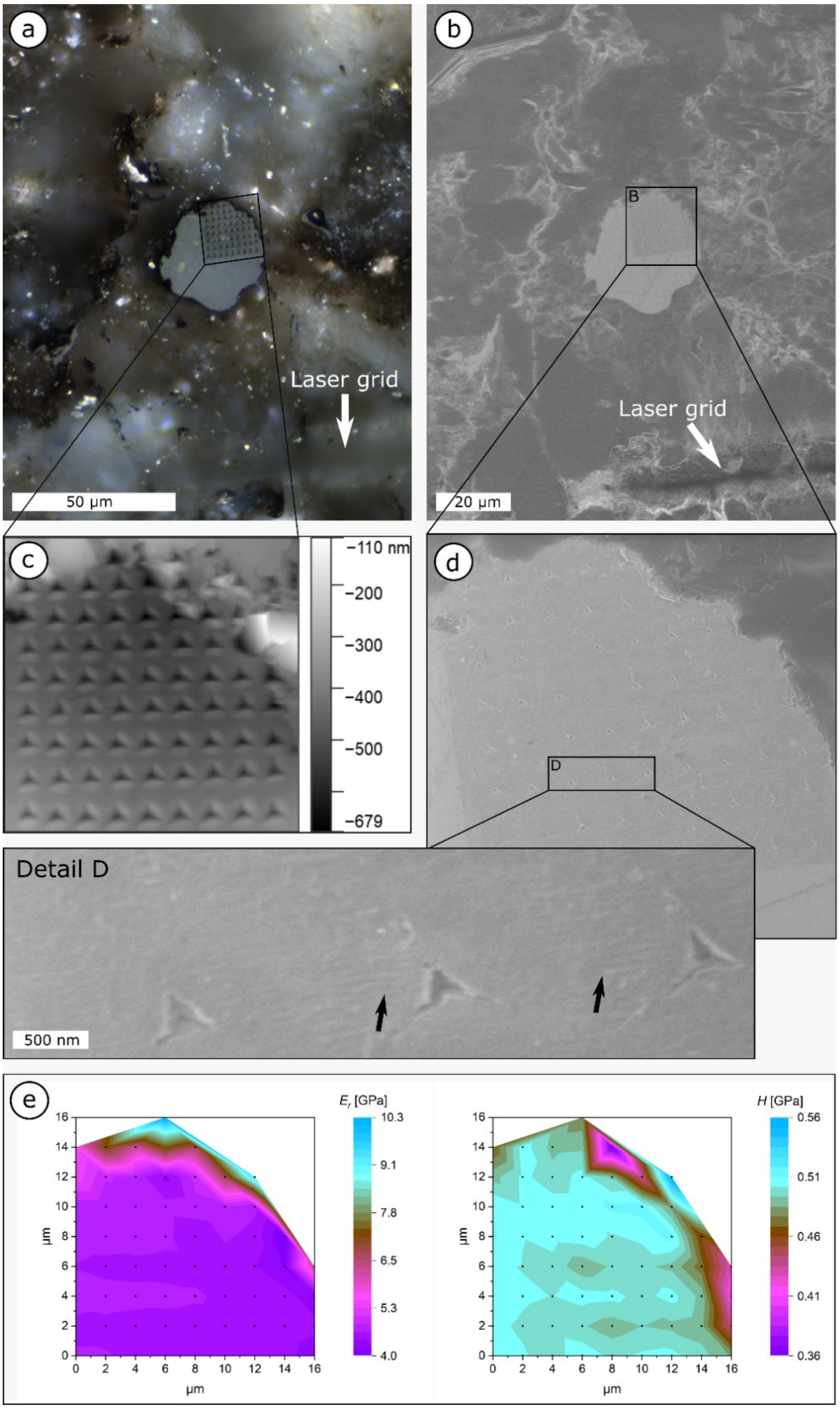

Figure 12: (a) Optical micrograph (oil immersion) of a vitrinite particle in sample SK12; the corresponding HIM images in (b, d) show a slight alteration (fine lines indicated by variations in SE contrast) of the mapped surface caused by the diamond tip during (c) SPM scanning (20x20 µm scan). (e) Corresponding E_r and H property maps (map 4) of the respective area. The black dots represent the positions of individual indents, while the property maps are created by linear interpolation between these values.

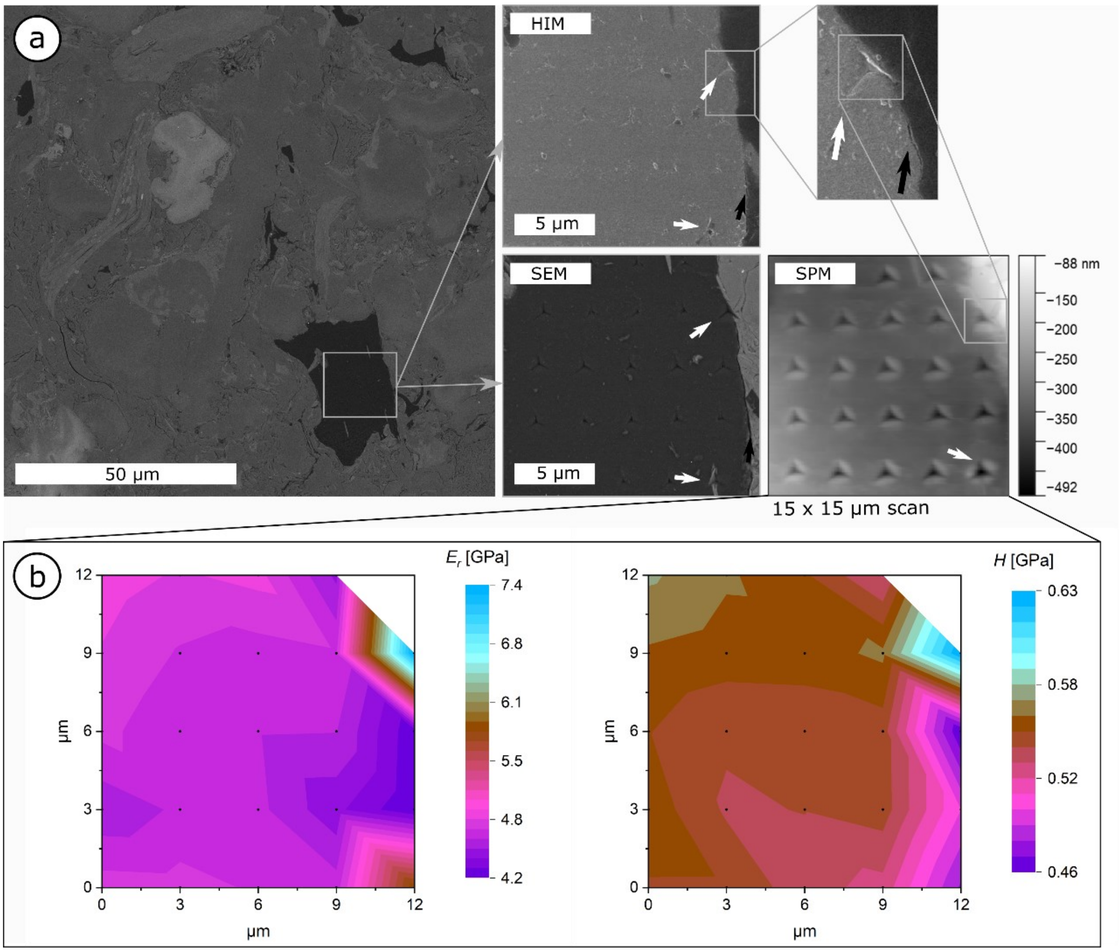

Figure 13: Correlative analysis of an OM particle (map 5) in sample SK12 including (a) SEM, HIM and SPM (15x15 µm scan) imaging (see insets). (b) displays the linearly interpolated E_r and H property maps of the respective area (black dots represent individual indents). Indents in proximity to minerals are indicated by white arrows, while interpreted shrinkage cracks are highlighted by black arrows.

10.3.3 *k*-means clustering

k-means clustering was applied on the mapping datasets in order to study the data structure by identifying clusters and their centers (figure 14a). The maximum number of clusters was set to four. These different clusters within an individual OM particle may represent influencing factors such as proximity to mineral grain boundaries (figure 14b, c) or the local presence of pores or cracks. For several samples, the elbow method (Thorndike, 1953) and the silhouette method (Rousseeuw, 1987) proved helpful in predetermining the cluster number. The final assignment of clusters and the quality check of individual measurements was assisted by the evaluation of SPM maps and, if available, data from correlative high-resolution imaging (figures 12, 13).

Usually, the most "representative" OM domains (no apparent mineral inclusions/pores/cracks; distant to grain boundaries) are represented by the largest clusters for most property maps (figures 14, 15). The remaining obtained clusters and their respective centroids are denominated as "low", "elevated" and "high" based on their values compared to the "representative" clusters/centroids (table 5). In contrast to map 1 in sample SK2 (figure 14), map 1 in SK9 also needs to be corrected for a "low" cluster, underestimating the representative results (figure 15; table 5).

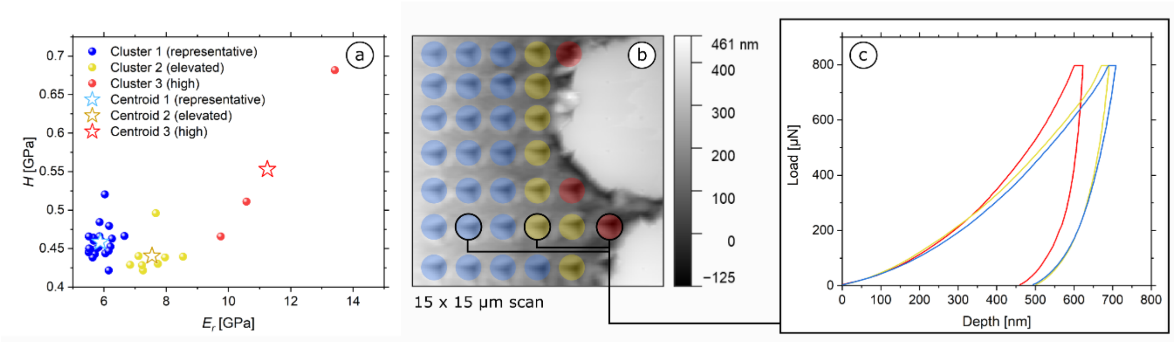

Figure 14: *k*-means clustering results for a map of sample SK2 (map 1). (a) *H* plotted versus E_r; the individuall data points are color-coded according to their cluster assignment. The representative centroids are indicated by stars (b) The color-coded nanoindents visualized within an SPM scan. (c) Example of load-displacement curves; the color-coding corresponds to the cluster colors shown in (a) and (b).

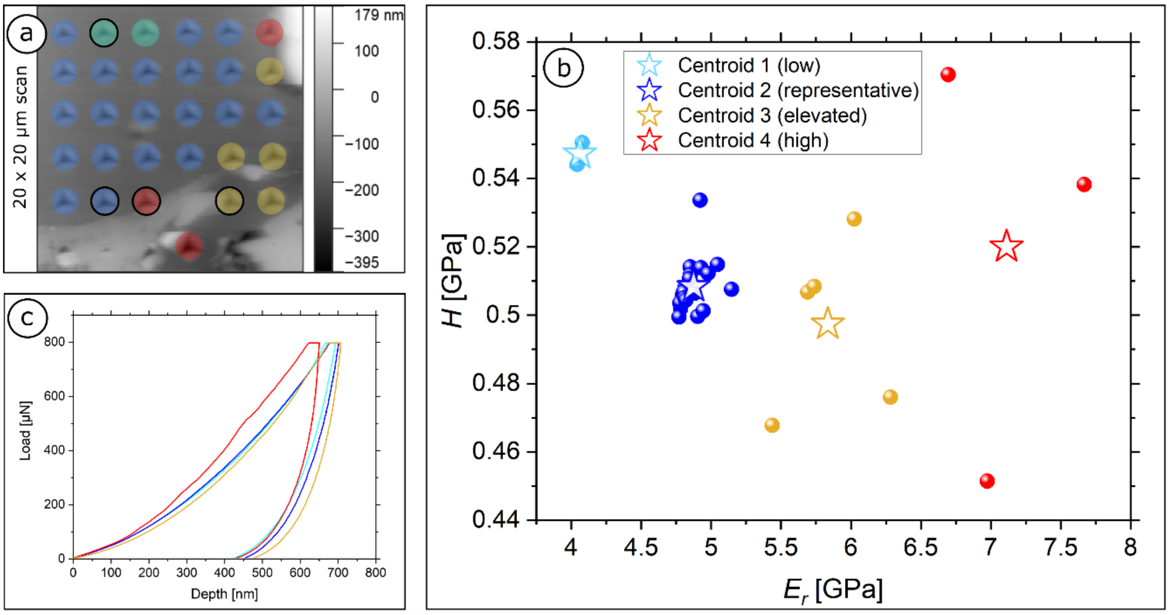

Figure 15: (a) SPM surface scan of a vitrinite particle in sample SK10 (map 1). The nanoindents are color-coded according to the *k*-means clustering results shown in (b). (c) Load displacement curves for the indents highlighted by black circles in (a).

Table 5 summarizes the *k*-means clustering results for E_r and H values obtained from each property map. In order to ensure reliability and enable comparability between the samples, the average of all data points within the representative centroids per sample/vitrinite reflectance are calculated (table 6). Average representative *k*-means E_r shows a decreasing trend with increasing vitrinite reflectance (figure 16a). In contrast, no maturity trend exists for the average *k*-means H (figure 16b), which remains relatively constant for all samples (average 0.40 – 0.55 GPa).

Table 5: *k*-means clustering results for all studied samples. All cluster centroids (representative, low, elevated, high) are shown together with their corresponding indent numbers (*n*) and OM types (v – vitrinite, sb – solid bitumen, i – inertinite).

		Representative			Low			Elevated			High			
Name	Map	*k*-means E_r	*k*-means H	n	*k*-means E_r	*k*-means H	n	*k*-means E_r	*k*-means H	n	*k*-means E_r	*k*-means H	n	OM type
		GPa	GPa		GPa	GPa		GPa	GPa		GPa	GPa		
SK2	1	5.88	0.46	22	-	-	-	7.54	0.44	8	11.25	0.55	3	v
	2	5.41	0.45	27	-	-	-	6.91	0.47	13	-	-	-	v
	3	5.86	0.44	10	-	-	-	7.24	0.44	3	10.19	0.59	1	v
	4	6.02	0.55	25	4.96	0.57	5	-	-	-	-	-	-	v
	5	6.17	0.57	26	5.25	0.56	20	7.11	0.56	11	10.95	0.64	1	v
	6	5.82	0.54	13	-	-	-	6.23	0.52	11	-	-	-	v
	7	6.02	0.51	20	-	-	-	7.23	0.53	20	12.32	0.78	1	v
SK5	1	5.25	0.45	15	-	-	-	6.25	0.47	5	12.03	0.82	1	sb
	2	4.98	0.40	43	-	-	-	6.68	0.40	3	-	-	-	sb
	3	4.68	0.42	31	-	-	-	5.61	0.46	7	7.48	0.55	2	sb
	4	5.14	0.48	31	-	-	-	7.89	0.37	2	11.92	0.53	1	sb
	5	5.03	0.41	14	-	-	-	-	-	-	9.55	0.37	1	sb
SK9	1	5.58	0.44	16	-	-	-	8.78	0.50	8	-	-	-	v
	2	4.22	0.48	32	-	-	-	6.82	0.35	1	-	-	-	v
	3	4.15	0.36	34	-	-	-	8.80	0.38	1	-	-	-	v
	4	4.27	0.45	15	-	-	-	6.76	0.51	3	-	-	-	v
	5	3.86	0.36	48	-	-	-	-	-	-	-	-	-	v
SK10	1	4.87	0.51	20	4.06	0.55	2	5.83	0.50	5	7.11	0.52	3	v
	2	5.27	0.53	33	-	-	-	6.20	0.52	6	-	-	-	v
	3	4.78	0.47	65	-	-	-	7.79	0.53	1	-	-	-	v
	4	5.08	0.53	23	-	-	-	8.67	0.60	5	-	-	-	v
	5	5.40	0.47	19	-	-	-	7.75	0.49	6	11.03	0.64	2	v
SK12	1	4.46	0.46	36	-	-	-	6.81	0.45	4	10.85	0.61	1	v
	2	4.68	0.39	36	-	-	-	6.12	0.38	7	8.13	0.42	1	v
	3	4.77	0.48	33	-	-	-	6.34	0.48	4	-	-	-	v
	4	4.61	0.49	55	-	-	-	6.59	0.44	5	9.90	0.52	2	v
	5	4.66	0.54	22	-	-	-	6.67	0.56	2	-	-	-	v
SK18	1	4.82	0.57	17	-	-	-	5.20	0.58	5	-	-	-	v
	2	4.79	0.55	45	4.10	0.58	2	-	-	-	-	-	-	v
	3	4.83	0.54	16	4.06	0.56	5	-	-	-	-	-	-	v
	4	5.37	0.48	15	-	-	-	10.25	0.70	5	16.86	0.89	2	v
	5	4.79	0.54	28	-	-	-	5.99	0.60	8	-	-	-	v
	6	4.77	0.50	29	-	-	-	7.62	0.48	3	-	-	-	v
SK37	1	4.41	0.60	30	-	-	-	8.04	0.72	6	13.36	0.89	3	i
	2	4.24	0.51	40	-	-	-	6.39	0.56	10	-	-	-	v
	3	4.45	0.57	20	-	-	-	6.05	0.59	3	8.59	0.74	2	v
	4	4.72	0.56	19	-	-	-	6.79	0.53	4	11.68	0.64	2	v
	5	4.67	0.49	13	3.58	0.45	6	5.84	0.52	6	-	-	-	v

Table 6: Averaged representative centroid values for each sample (see table 4 for raw data). (v – vitrinite, sb – solid bitumen, i – inertinite).

			Representative average						
Name	Depth m	*VR* %Rr	*k*-means E_r GPa	SD GPa	*k*-means *H* GPa	SD GPa	Indents *n*	OM types	Comments
SK2	3376	1.33	5.88	0.37	0.51	0.05	143	v	all data included
SK5	3466	1.68	4.98	0.36	0.43	0.05	134	sb	all data included
SK9	3586	1.96	4.07	0.32	0.40	0.06	129	v	outlier excluded (map 1)
			4.24	0.59	0.41	0.06	145	v	all centroids included
SK10	3616	1.89	5.01	0.34	0.50	0.03	160	v	all centroids included
SK12	3676	2.00	4.63	0.28	0.47	0.06	182	v	all centroids included
SK18	3866	2.23	4.85	0.35	0.53	0.03	150	v	all centroids included
			4.81	0.12	0.55	0.01	78	v	coaly part (maps 1, 2, 3)
			4.90	0.48	0.51	0.03	72	v	shaly part (maps 4, 5, 6)
SK37	4426	2.21	4.43	0.55	0.42	0.05	122	v, i	all centroids included

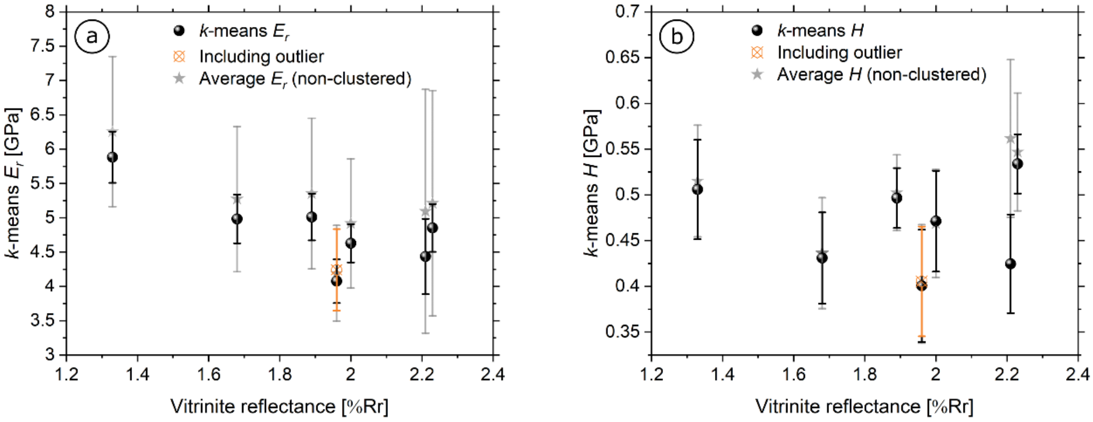

Figure 16: Average *k*-means representative centroids for (a) E_r and (b) *H* plotted against vitrinite reflectance (see table 6). Non-clustered averages were included for comparison (see table 4, figure 11).

OM at 1.33 %Rr (SK2) exhibits the highest E_r with representative *k*-means centroids ranging from 5.41 to 6.17 GPa (seven maps, average *k*-means center at 5.88±0.37 GPa). For solid bitumen in SK5 at 1.68 %Rr the representative *k*-means centroids for E_r vary from 4.68 to 5.25 GPa. The representative average *k*-means centroids for E_r at 1.89 %Rr (SK10), 1.96 %Rr (SK9) and 2.00 %Rr (SK12), obtained from 5 maps each, deviate significantly from each other, despite the minor differences in thermal maturity (table 6). The largest discrepancy between representative E_r centroids is observed at 1.96 %Rr (SK9), where the *k*-means centroids of four out of five maps show only minor variation from 3.86 to 4.27 GPa, whereas one larger OM layer with mineral inclusions is strongly shifted to 5.58 GPa (table 5, map 1).

The average E_r centroids obtained from samples at ~2.2 %Rr range at 4.43±0.55 for sample SK37 (five maps) and 4.85±0.35 GPa (six maps) for sample SK18. In contrast to the remaining samples, an inertinite particle was also included in the testing of sample SK37, exhibiting similar results compared to vitrinite (table 5, map 1 of SK37). The average *k*-means centroids from SK18 were obtained from six property maps including three maps from a single vitrinite layer and three maps from dispersed vitrinite hosting authigenic minerals. The representative centroids from the particles with authigenic mineral inclusions show slightly elevated E_r values and more variation between the individual average values (4.77 – 5.37 GPa) compared to those obtained from the homogeneous vitrinite layer (4.79 – 4.83 GPa). Furthermore, the non-representative "elevated" and "high" clusters of vitrinites with extensive authigenic mineral occurrence show considerably higher E_r values with a maximum at 16.86 GPa (table 5; map 4).

10.4 Discussion

10.4.1 Influence of boundary proximity and mineral inclusions on micromechanical properties of organic matter

The nanoindentation property mapping revealed strong heterogeneities of the micromechanical parameters (especially E_r) within individual OM particles. As evidence for correlating nanoindentation property maps (figures 12, 13) and high-resolution images (figures 5d, 6c), these variations are mostly noticed either in presence of mineral inclusions within OM or the restraint by surrounding mineral grains, mostly resulting in increased elastic modulus values near OM – mineral grain boundary regions (figures 12–15). Also, the nanoindentation mapping-procedure might also induce cracks in tested particle (figure 17). For the postmature samples investigated here, the locally increased E_r values are interpreted as the result of intense burial compaction and consequently the OM being indented by the grain framework. Similar observations (enhance apparent modulus of OM due to surrounding and underlying mineral matrix) were also reported by Zargari et al. (2016) for OM in Bakken shales.

Vranjes et al. (2018) observed a positive correlation of ash yield (inorganic residue after coal combustion) and the E_r of vitrinite in coals. As the mineral matter content of a coal seam can be approximated by its ash yield, this trend was interpreted as the result of a relative density increase of the tested vitrinite particles due to mineral inclusions.

Even for the undisturbed OM groundmass (representative centroids from *k*-means clustering), significantly different E_r values have been determined for samples at comparable thermal maturity (e.g., samples SK10 and SK9 at 1.89 and 1.96 %Rr VR, respectively; table 5, 6). For these samples, BIB-SEM images reveal substantial differences regarding grain size and diagenetic cementation (figures 4b, 5b, 6b,). The average E_r obtained from *k*-means centroids for the OM within the coarse-grained, well-cemented sample SK9 is 4.07±0.32 GPa (excluding an outlier from mineral matter-rich OM; see tables 3, 5; map 1) and ranges considerably lower compared to the finer-grained, clay-rich sample SK10 (average 5.01±0.34 GPa).

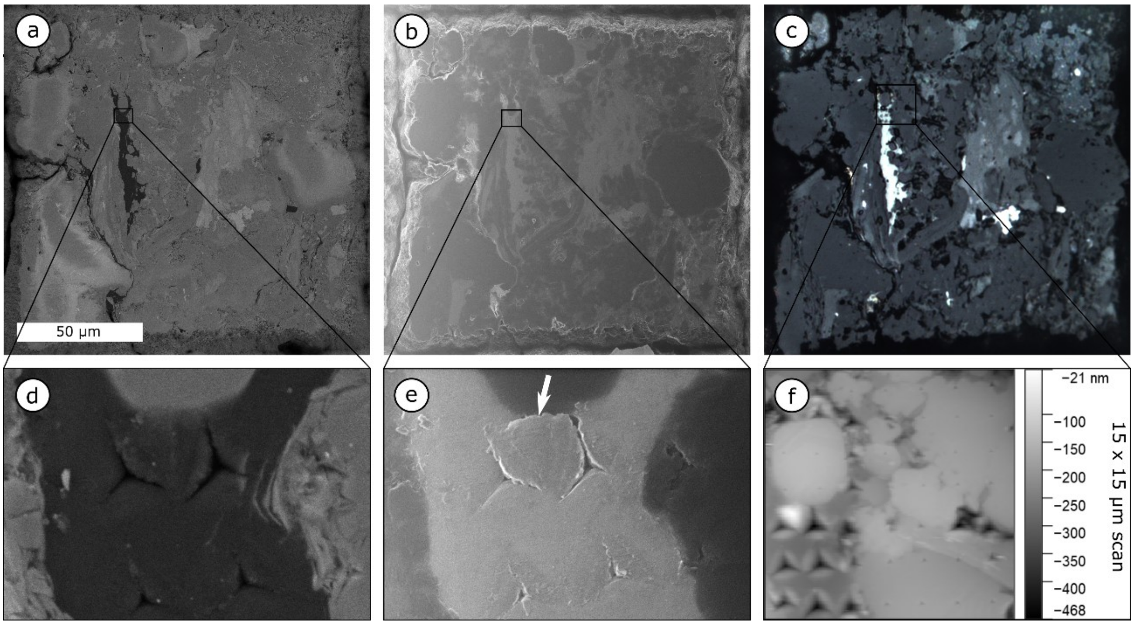

Figure 17: Correlative imaging of a vitrinite particle within sample SK12. (a) SEM and (b) HIM overview with detailed excerpts (d, e respectively). (c) Optical overview of a laser grid quadrant (no oil immersion). (f) SPM image with indicated topographical feature within tested OM area (15x15 µm scan). A crack likely resulting from the property mapping can be imaged by means of HIM imaging (see e).

This difference in stiffness is likely attributed to the more intense burial compaction in the clay-rich facies. The absence of pressure shadows in-between large, brittle mineral grains results in a systematic increase in OM compression by the surrounding clay matrix. Enhanced compression might be an effect of more efficient compaction effects based on the plate-like morphologies of clay minerals (Hubbert and Rubey, 1959; Revil et al., 2002). Hence, the lower clay content and predominately coarse-grained mineral matrix of sample SK9 likely impeded compaction, thereby leading to less confinement and lower average E_r of OM particles (figure 10).

10.4.2 Micromechanical changes with thermal maturation and pore structure evolution

The representative *k*-means centers for the E_r of OM exhibit a decreasing trend with increasing thermal maturity (%Rr). Declining modulus values were also observed by Zargari et al. (2016) for kerogen at maturity levels from the onset of the oil window throughout the gas window. According to these authors, this observation is likely related to the formation of gas- or bitumen-filled nanopores with proceeding thermal maturity. In contrast, Emmanuel (2016) showed a general increase of the elastic modulus for kerogen between 0.40 and 0.82 %Rr and stable mechanical properties between 0.82 and 1.25 %Rr. A general increase of the Young´s modulus of vitrinite with thermal maturity (between 0.62 and 1.13

%Rr) was also demonstrated in the nanoindentation study by Zhao et al. (2020). Both studies (Emmanuel et al., 2016; Zhao et al., 2020) concluded that the thermally-induced stiffness increase is likely a result of ongoing aromatization. These findings are supported by an atomistic modelling study where the Young´s modulus of kerogen increases exponentially with density and aromatic ordering caused by increasing burial stress (Kashinath et al., 2020). However, the natural variability of OM-hosted porosity was not accounted for in the fundamental property modelling study and the authors emphasize that local porosity may lead to a significant weakening (Kashinath et al., 2020). The competing effects of structural ordering (aromatization) versus pore generation have been demonstrated within a previous TEM study on vitrinite macerals in coals (Vranjes-Wessely et al., 2020). While increased ordering of aromatic stacks was suggested to increase the stiffness of vitrinite, a stiffness decrease could be linked to increasingly larger mesoporosity due to hydrocarbon cracking from the primary kerogen. Vranjes-Wessley et al. (2020) concluded that smaller pores can share an applied load more efficiently in contrast to samples containing fewer but larger pores. It also needs to be emphasized that most experimental data cited for kerogen (Emmanuel et al., 2016; Zargari et al., 2016; Zhao et al., 2020) was obtained from samples below a thermal maturity of 1.25 %Rr, whereas the specimen in this study cover postmature samples up to 2.23 %Rr. No major SEM-visible OM-hosted porosity was observed in samples at 1.33 %Rr, 1.89 %Rr, 1.96 and 2.00 %Rr. Furthermore, the apparent absence of visible OM porosity at 1.33 %Rr (figures 2c, d) might be linked to pore occlusion by hydrocarbons (bitumen), as previously demonstrated by bitumen-extraction experiments of post-mature samples (Misch et al., 2019b; Valenza et al., 2013; Wei et al., 2014). In comparison, kerogen at 2.23 %Rr (sample SK18) exhibits distinct porosity (figures 7c, e) indicating removal of clogging bitumen from pores and further thermally induced pore generation (Misch et al., 2019a). The OM pores at 2.23 %Rr are characterized by angular/asymmetrical shapes and inhomogeneous distribution within the particles (figures 7c, e). Irregular pore distribution within a single OM particle might be attributed to initial inherent inhomogeneities (Löhr et al., 2015), differential grain support during compaction (Curtis et al., 2012; Mathia et al., 2016; Schieber, 2013) and intercalations between OM and mineral matter (Mathia et al., 2016; Milliken et al., 2013). Misch et al., (2020) showed that OM-hosted pore shapes are influenced by burial compaction similar as mineral matrix pores. The virtual absence of SEM-visible porosity likely results from increased confinement effects of OM restrained within the grain framework. A dependence of OM porosity and pore geometry factors on brittle mineral content was also reported by Misch et al. (2018) for oil to wet gas mature shales. In the aforementioned study, abundant OM pores at gas window maturity were interpreted as being the result of lesser compaction in-between a brittle grain fabric. Nevertheless, the visible OM pores within the sample SK5 (figures 3c-e) at 1.68 %Rr might be rather associated with organic – inorganic interfaces than under-compaction, which is supported by relatively high E_r values despite a porous structure of the investigated OM. Interestingly, despite the OM tested in SK5 is interpreted as secondary solid bitumen rather than vitrinite, the determined stiffness is among the highest values of all investigated samples (tables 3 – 6). Therefore, it is suggested that the controlling factors for micromechanical properties are complex and not solely related to the evolving pore structure. In consequence, the general decrease of E_r with increasing thermal maturity cannot exclusively be assigned to evolving pore development and stiffness prediction therefore requires a comprehensive evaluation of all possible maturity-related geochemical and structural changes, as well as the microstructural characteristics of the individual sample, which in turn controls the porosity preservation (see also Curtis et al. (2012)). Thus, the material properties of OM can be viewed as the result of mechanical and geochemical processes that vary for each unique geological environment. Our novel approach using *k*-means clustering in conjunction with high-resolution imaging techniques has proven to be an effective approach for geological reasoning of micromechanical property variations.

10.4.3 Micromechanical properties of vitrinite/inertinite versus solid bitumen

Different OM classifications are used in organic geochemical and petrographical studies (see Misch et al., 2019 and Mastalerz et al., 2018). Vitrinite is the predominant OM constituent in the studied sample set (see figures 2a, 4a, 5a, 6a, 7a, 8a). The structure of vitrinite is characterized by a great degree of aromaticity, which further increases with thermal maturity. In contrast, solid bitumen, a transformation product of primary OM during thermal alteration, hosts a significant proportion of aliphatic hydrocarbon chains. However, these aliphatic compounds break down with ongoing cracking, resulting in a relative increase of aromaticity (Craddock et al., 2015). This leads to a convergence of the reflectance properties of solid bitumen and vitrinite above 1.0 %Rr (Hackley and Lewan, 2018; Landis and Castaño, 1995) and particularly in overmature stage, growing a challenge in their discrimination.

According to previous nanomechanical studies, primary macerals (vitrinite and inertinite) exhibit a higher stiffness compared to more ductile solid bitumen (Emmanuel et al., 2016; Zhao et al., 2020). However, the results of Zhao et al. (2020) indicate that the Young´s modulus of solid bitumen increases with thermal maturity and becomes more similar to the values determined for vitrinite at equal maturity beyond the late oil window (see table 2 in Zhao et al. (2020)). This is supported by the mechanical parameters determined for solid bitumen in sample SK5 of this study; E_r and H values comparable to vitrinite in the overmature sample are likely a result of the increased aromaticity at this stage. Nevertheless, different character of solid bitumen due to changing organofacies was reported, and particularly the solid bitumen-hosted porosity trends may deviate substantially for changing primary OM composition (Misch et al., 2019a, b), which may result in changing mechanical behavior as well. On the other hand, it may be difficult to delineate between solid bitumen and vitrinite, in cases where soluble bitumen is retained by vitrinite an both form an entity even in overmature state (Cardott et al., 2015; Misch et al., 2019a).

The representative *k*-means E_r of an inertinite particle in sample SK37 (table 5; map 1) shows no significant deviation from the values determined for vitrinite in the same specimen. Inertinite is mainly a product of land plant material charred during paleo-wildfires. As a consequence, it shows considerably higher initial C and O contents, as well as lower initial H clontents compared to vitrinite and other primary OM types. It is well accepted that structural changes (devolatilization, aromatization) of inertinite occur comparably early during diagenesis (International Committee for Coal and Organic Petrology (ICCP), 2001; Levine, 1993). Furthermore, Vranjes et al. (2018) clearly showed that the micromechanical properties of inertinite macerals in coals from the Ukrainian Donets Basin correlate perfectly with the inertinite reflectance, which reflects the temperature conditions during paleo-wildfires and hence pre-depositional processes. In spite of these fundamental differences to the diagenetic evolution of vitrinite, previous studies postulated a converge of properties particularly at high rank >2 %Rr (Levine, 1993). Relating this to the overmature state of the samples investigated here, it is reasonable to assume that ongoing homogenization may have occurred, leading to similar material behavior of vitrinite and inertinite.

10.4.4 Improved workflow and quality control in micromechanical testing

Specimen preparation by a femto-second laser grid (figure 1) enabled correlation between imaging and mechanical testing. This approach should be adopted in future micromechanical studies, as a strong interdependency between mechanical parameters and structural features was clearly proven by nanoindentation mapping combined with SEM and HIM (figures 12, 13). Material parameters (E_r and H) were identified from individual OM particles and analyzed by *k*-means clustering. In combination with the SPM images and the correlative high-resolution imaging, the obtained E_r and H clusters were correlated evaluated to identify the reasons behind local variations (e.g., boundary effects, intraparticle heterogeneity, etc.). It proved extremely valuable to be able to trace back to the individual indent in the complementary image data. Thereby, outlier measurements, e.g., due to breakouts along OM – mineral contacts, could easily be identified. A further enhancement of data quality and property correlations was achieved by the *k*-means++-enhanced *k*-means clustering of the high-speed nanoindentation mapping data (figures 14, 15). Microstructural and thermal maturity influences which were not clearly resolved by the initial data set, became more distinct after cluster-processing (table 3, 5; figure 16). However, further analytical improvement, particularly for the investigation of OM-rich rocks, may be achieved by optimized low- or non-invasive preparation (Hackley et al., 2020; Loucks et al., 2009). Particularly the influence of variations in the array spacing during high-speed property mapping in soft materials such as kerogen and bitumen needs to be addressed further, in order to balance maximum resolution and minimize interference between neighboring indents. Also, the impact of surface alteration by the Cube Corner tip during scanning, which was clearly observed in HIM images (figure 12), has to be considered. HIM proved a very valuable tool for the detection of such surface effects, as the image contrast created by the helium ion beam is not based on atomic number as compared to an electron beam (Ward et al., 2006), and thus OM structures can be visualized at even higher resolution and topographic sensitivity compared to conventional SEM systems (Bell, 2009; Scipioni et al., 2009). This includes detailed images of indents in OM and at OM/mineral interfaces (figures 12, 13), which helped to identify outliers such as nanoindentation-induced cracks at OM – mineral boundaries (figure 17).

10.5 Conclusion

In this study the OM of an over-mature sample set from the Songliao Basin in China was mechanically characterized by a new approach of combined high-speed nanoindentation property mapping, high-resolution imaging and machine learning based data processing. Femto-second laser marked areas enabled a correlative study, which facilitated further evaluation of the mechanically tested areas. In order to gain a better understanding regarding the material characteristics and potential influencing factors, high-resolution SEM and HIM imaging was carried out. The resulting E_r and H data from each high-speed nanoindentation property map was subsequently processed by the unsupervised machine learning algorithm k-means clustering to evaluate the representative material properties of OM particles which in general exhibit inhomogeneous stiffness and thus a large spread of E_r. Enhanced OM modulus values were associated with adjacent mineral matter, while pores, cracks and surface artifacts likely lead to significantly lowered E_r. The formation of these varying mechanical domains is interpreted to be a result of differential density and compaction of the OM on the submicron level. It was also determined that the E_r of OM generally decreases with increasing maturity. This trend must be viewed with caution, as the compaction and stress support of the OM particles are likely dependent on the mineral fabric. At comparable maturity, OM within predominant clay matrix exhibits higher E_r results compared to OM embedded within a rock fabric with coarse character, as the presence of clay minerals favors a more effective compaction.

The lacking porosity of kerogen presumably related to pore occlusion by secondary generated bitumen. Although solid bitumen is believed to have similar properties to vitrinite in the over-mature state, it is not yet clear how it affects the mechanical properties of kerogen while occluding pores and forming an interphase.

In conclusion, this approach has proven itself extremely valuable for the detailed material characterization of complex and highly inhomogeneous materials. While this already opens a wealth of exciting new possibilities, future studies on this subject shall also focus on the further optimization of the experimental settings and enhancement of the workflow.

References

Abedi, S., Slim, M., Ulm, F.-J., 2016. Nanomechanics of organic-rich shales: the role of thermal maturity and organic matter content on texture. Acta Geotech. 11, 775–787. https://doi.org/10.1007/s11440-016-0476-2

Ahmadov, R., Vanorio, T., Mavko, G., 2009. Confocal laser scanning and atomic-force microscopy in estimation of elastic properties of the organic-rich Bazhenov Formation. Lead. Edge 28, 18–23. https://doi.org/10.1190/1.3064141

Alstadt, K.N., Katti, K.S., Katti, D.R., 2016. Nanoscale Morphology of Kerogen and In Situ Nanomechanical Properties of Green River Oil Shale. J. Nanomechanics Micromechanics 6, 04015003. https://doi.org/10.1061/(ASCE)NM.2153-5477.0000103

Arthur, D., Vassilvitskii, S., 2007. K-Means++: The Advantages of Careful Seeding. Proc. Eighteenth Annu. ACM-SIAM Symp. Discrete Algorithms 1027–1035.

Bell, D.C., 2009. Contrast Mechanisms and Image Formation in Helium Ion Microscopy. Microsc. Microanal. 15, 147–153. https://doi.org/10.1017/S1431927609090138

Bennett, K.C., Berla, L.A., Nix, W.D., Borja, R.I., 2015. Instrumented nanoindentation and 3D mechanistic modeling of a shale at multiple scales. Acta Geotech. 10, 1–14. https://doi.org/10.1007/s11440-014-0363-7

Bobko, C., Ulm, F.-J., 2008. The nano-mechanical morphology of shale. Mech. Mater. 40, 318–337. https://doi.org/10.1016/j.mechmat.2007.09.006

Cardott, B.J., Landis, C.R., Curtis, M.E., 2015. Post-oil solid bitumen network in the Woodford Shale, USA — A potential primary migration pathway. Int. J. Coal Geol. 139, 106–113. https://doi.org/10.1016/j.coal.2014.08.012

Cavanaugh, T., Walls, J., 2016. Multiresolution Imaging of Shales Using Electron and Helium Ion Microscopy, in: Olson, T. (Ed.), Imaging Unconventional Reservoir Pore Systems. American Association of Petroleum Geologists, pp. 65–76. https://doi.org/10.1306/13592017M1123693

Charlet, L., Alt-Epping, P., Wersin, P., Gilbert, B., 2017. Diffusive transport and reaction in clay rocks: A storage (nuclear waste, CO2, H2), energy (shale gas) and water quality issue. Adv. Water Resour. 106, 39–59. https://doi.org/10.1016/j.advwatres.2017.03.019

Constantinides, G., Ravi Chandran, K.S., Ulm, F.-J., Van Vliet, K.J., 2006. Grid indentation analysis of composite microstructure and mechanics: Principles and validation. Mater. Sci. Eng. A 430, 189–202. https://doi.org/10.1016/j.msea.2006.05.125

Craddock, P.R., Le Doan, T.V., Bake, K., Polyakov, M., Charsky, A.M., Pomerantz, A.E., 2015. Evolution of Kerogen and Bitumen during Thermal Maturation via Semi-Open Pyrolysis Investigated by Infrared Spectroscopy. Energy Fuels 29, 2197–2210. https://doi.org/10.1021/ef5027532

Curtis, M.E., Cardott, B.J., Sondergeld, C.H., Rai, C.S., 2012. Development of organic porosity in the Woodford Shale with increasing thermal maturity. Int. J. Coal Geol. 103, 26–31. https://doi.org/10.1016/j.coal.2012.08.004

Desheng, L., Renqi, J., Katz, Barry Jay, 1995. Petroleum Generation in the Nonmarine Qingshankou Formation (Lower Cretaceous), Songliao Basin, China, in: Katz, Barry J. (Ed.), Petroleum Source Rocks, Casebooks in Earth Sciences. Springer Berlin Heidelberg, Berlin, Heidelberg, pp. 131–148. https://doi.org/10.1007/978-3-642-78911-3_8

Ebenstein, D.M., Pruitt, L.A., 2006. Nanoindentation of biological materials. Nano Today 1, 26–33. https://doi.org/10.1016/S1748-0132(06)70077-9

Eliyahu, M., Emmanuel, S., Day-Stirrat, R.J., Macaulay, C.I., 2015. Mechanical properties of organic matter in shales mapped at the nanometer scale. Mar. Pet. Geol. 59, 294–304. https://doi.org/10.1016/j.marpetgeo.2014.09.007

Emmanuel, S., Eliyahu, M., Day-Stirrat, R.J., Hofmann, R., Macaulay, C.I., 2016. Impact of thermal maturation on nano-scale elastic properties of organic matter in shales. Mar. Pet. Geol. 70, 175–184. https://doi.org/10.1016/j.marpetgeo.2015.12.001

Goldsby, D.L., Rar, A., Pharr, G.M., Tullis, T.E., 2004. Nanoindentation creep of quartz, with implications for rate- and state-variable friction laws relevant to earthquake mechanics. J. Mater. Res. 19, 357–365. https://doi.org/10.1557/jmr.2004.19.1.357

Hackley, P.C., Jubb, A.M., McAleer, R.J., Valentine, B.J., Birdwell, J.E., 2021. A review of spatially resolved techniques and applications of organic petrography in shale petroleum systems. Int. J. Coal Geol. 103745. https://doi.org/10.1016/j.coal.2021.103745

Hackley, P.C., Jubb, A.M., Valentine, B.J., Hatcherian, J.J., Yu, J.-J., Podrazky, W.K., 2020. Investigating the effects of broad ion beam milling to sedimentary organic matter: Surface flattening or heat-induced aromatization and condensation? Fuel 282, 118627. https://doi.org/10.1016/j.fuel.2020.118627

Hackley, P.C., Lewan, M., 2018. Understanding and distinguishing reflectance measurements of solid bitumen and vitrinite using hydrous pyrolysis: Implications to petroleum assessment. AAPG Bull. 102, 1119–1140. https://doi.org/10.1306/08291717097

Hackley, P.C., Valentine, B.J., Voortman, L.M., Van Oosten Slingeland, D.S.B., Hatcherian, J., 2017. Utilization of integrated correlative light and electron microscopy (iCLEM) for imaging sedimentary organic matter. J. Microsc. 267, 371–383. https://doi.org/10.1111/jmi.12576

Hartigan, J.A., Wong, M.A., 1979. Algorithm AS 136: A K-Means Clustering Algorithm. Appl. Stat. 28, 100. https://doi.org/10.2307/2346830

Hay, J., 2009. INTRODUCTION TO INSTRUMENTED INDENTATION TESTING. Exp. Tech. 33, 66–72. https://doi.org/10.1111/j.1747-1567.2009.00541.x

Hlawacek, G., Veligura, V., van Gastel, R., Poelsema, B., 2014. Helium ion microscopy. J. Vac. Sci. Technol. B Nanotechnol. Microelectron. Mater. Process. Meas. Phenom. 32, 020801. https://doi.org/10.1116/1.4863676

Hou, H., Wang, C., Zhang, J., Ma, F., Fu, W., Wang, P., Huang, Y., Zou, C., Gao, You-feng, Gao, Yuan, Zhang, L., Yang, J., Guo, R., 2018. Deep Continental Scientific Drilling Engineering Project in Songliao Basin: progress in Earth Science research. China Geol. 1, 173–186. https://doi.org/10.31035/cg2018036

Huang, C., Ju, Y., Zhu, H., Lash, G.G., Qi, Y., Yu, K., Feng, H., Ju, L., Qiao, P., 2020. Investigation of formation and evolution of organic matter pores in marine shale by helium ion microscope: An example from the Lower Silurian Longmaxi Shale, South China. Mar. Pet. Geol. 120, 104550. https://doi.org/10.1016/j.marpetgeo.2020.104550

Hubbert, M., Rubey, W.W., 1959. ROLE OF FLUID PRESSURE IN MECHANICS OF OVERTHRUST FAULTING. Geol. Soc. Am. Bull. 70, 115. https://doi.org/10.1130/0016-7606(1959)70[115:ROFPIM]2.0.CO;2

International Committee for Coal and Organic Petrology (ICCP), 2001. The new inertinite classification (ICCP System 1994). Fuel 80, 459–471. https://doi.org/10.1016/S0016-2361(00)00102-2

Jakob, S., Pfeifenberger, M.J., Hohenwarter, A., Pippan, R., 2017. Femtosecond laser machining for characterization of local mechanical properties of biomaterials: a case study on wood. Sci. Technol. Adv. Mater. 18, 574–583. https://doi.org/10.1080/14686996.2017.1360751

Kashinath, A., Szulczewski, M., Dogru, A.H., 2020. Modeling the Effect of Maturity on the Elastic Moduli of Kerogen Using Atomistic Simulations. Energy Fuels 34, 1378–1385. https://doi.org/10.1021/acs.energyfuels.9b03221

Khatibi, S., Aghajanpour, A., Ostadhassan, M., Ghanbari, E., Amirian, E., Mohammed, R., 2018. Evaluating the Impact of Mechanical Properties of Kerogen on Hydraulic Fracturing of Organic Rich Formations, in: SPE Canada Unconventional Resources Conference. Presented at the SPE Canada Unconventional Resources Conference, Society of Petroleum Engineers, Calgary, Alberta, Canada. https://doi.org/10.2118/189799-MS

King, H.E., Eberle, A.P.R., Walters, C.C., Kliewer, C.E., Ertas, D., Huynh, C., 2015. Pore Architecture and Connectivity in Gas Shale. Energy Fuels 29, 1375–1390. https://doi.org/10.1021/ef502402e

Konstantopoulos, G., Koumoulos, E.P., Charitidis, C.A., 2020. Classification of mechanism of reinforcement in the fiber-matrix interface: Application of Machine Learning on nanoindentation data. Mater. Des. 192, 108705. https://doi.org/10.1016/j.matdes.2020.108705

Koumoulos, E.P., Paraskevoudis, K., Charitidis, C.A., 2019. Constituents Phase Reconstruction through Applied Machine Learning in Nanoindentation Mapping Data of Mortar Surface. J. Compos. Sci. 3, 63. https://doi.org/10.3390/jcs3030063

Kranjc, K., Rouse, Z., Flores, K.M., Skemer, P., 2016. Low-temperature plastic rheology of olivine determined by nanoindentation. Geophys. Res. Lett. 43, 176–184. https://doi.org/10.1002/2015GL065837

Kumar, V., Curtis, M.E., Gupta, N., Sondergeld, C.H., Rai, C.S., 2012a. Estimation of Elastic Properties of Organic Matter in Woodford Shale Through Nanoindentation Measurements, in: SPE Canadian Unconventional Resources Conference. Presented at the SPE Canadian Unconventional Resources Conference, Society of Petroleum Engineers, Calgary, Alberta, Canada. https://doi.org/10.2118/162778-MS

Kumar, V., Sondergeld, C.H., Rai, C.S., 2012b. Nano to Macro Mechanical Characterization of Shale, in: SPE Annual Technical Conference and Exhibition. Presented at the SPE Annual Technical Conference and Exhibition, Society of Petroleum Engineers, San Antonio, Texas, USA. https://doi.org/10.2118/159804-MS

Kumar, V., Sondergeld, C., Rai, C.S., 2015. Effect of mineralogy and organic matter on mechanical properties of shale. Interpretation 3, SV9–SV15. https://doi.org/10.1190/INT-2014-0238.1

Landis, C.R., Castaño, J.R., 1995. Maturation and bulk chemical properties of a suite of solid hydrocarbons. Org. Geochem. 22, 137–149. https://doi.org/10.1016/0146-6380(95)90013-6

Levine, J.R., 1993. Coalification: The Evolution of Coal as Source Rock and Reservoir Rock for Oil and Gas. https://doi.org/10.1306/St38577C3

Liu, K., Ostadhassan, M., Bubach, B., 2016. Applications of nano-indentation methods to estimate nanoscale mechanical properties of shale reservoir rocks. J. Nat. Gas Sci. Eng. 35, 1310–1319. https://doi.org/10.1016/j.jngse.2016.09.068

Liu, K., Ostadhassan, M., Bubach, B., Ling, K., Tokhmechi, B., Robert, D., 2018. Statistical grid nanoindentation analysis to estimate macro-mechanical properties of the Bakken Shale. J. Nat. Gas Sci. Eng. 53, 181–190. https://doi.org/10.1016/j.jngse.2018.03.005

Löhr, S.C., Baruch, E.T., Hall, P.A., Kennedy, M.J., 2015. Is organic pore development in gas shales influenced by the primary porosity and structure of thermally immature organic matter? Org. Geochem. 87, 119–132. https://doi.org/10.1016/j.orggeochem.2015.07.010

Loucks, R.G., Reed, R.M., Ruppel, S.C., Jarvie, D.M., 2009. Morphology, Genesis, and Distribution of Nanometer-Scale Pores in Siliceous Mudstones of the Mississippian Barnett Shale. J. Sediment. Res. 79, 848–861. https://doi.org/10.2110/jsr.2009.092

Luo, S., Lu, Y., Wu, Y., Song, J., DeGroot, D.J., Jin, Y., Zhang, G., 2020. Cross-scale characterization of the elasticity of shales: Statistical nanoindentation and data analytics. J. Mech. Phys. Solids 140, 103945. https://doi.org/10.1016/j.jmps.2020.103945

Ma, Z., Pathegama Gamage, R., Zhang, C., 2020. Application of nanoindentation technology in rocks: a review. Geomech. Geophys. Geo-Energy Geo-Resour. 6, 60. https://doi.org/10.1007/s40948-020-00178-6

Mashhadian, M., Verde, A., Sharma, P., Abedi, S., 2018. Assessing mechanical properties of organic matter in shales: Results from coupled nanoindentation/SEM-EDX and micromechanical modeling. J. Pet. Sci. Eng. 165, 313–324. https://doi.org/10.1016/j.petrol.2018.02.039

Mastalerz, M., Drobniak, A., Stankiewicz, A.B., 2018. Origin, properties, and implications of solid bitumen in source-rock reservoirs: A review. Int. J. Coal Geol. 195, 14–36. https://doi.org/10.1016/j.coal.2018.05.013

Mathia, E.J., Bowen, L., Thomas, K.M., Aplin, A.C., 2016. Evolution of porosity and pore types in organic-rich, calcareous, Lower Toarcian Posidonia Shale. Mar. Pet. Geol. 75, 117–139. https://doi.org/10.1016/j.marpetgeo.2016.04.009

Milliken, K.L., Rudnicki, M., Awwiller, D.N., Zhang, T., 2013. Organic matter-hosted pore system, Marcellus Formation (Devonian), Pennsylvania. AAPG Bull. 97, 177–200. https://doi.org/10.1306/07231212048

Misch, D., Gross, D., Hawranek, G., Horsfield, B., Klaver, J., Mendez-Martin, F., Urai, J.L., Vranjes-Wessely, S., Sachsenhofer, R.F., Schmatz, J., Li, J., Zou, C., 2019a. Solid bitumen in shales: Petrographic characteristics and implications for reservoir characterization. Int. J. Coal Geol. 205, 14–31. https://doi.org/10.1016/j.coal.2019.02.012

Misch, D., Klaver, J., Gross, D., Mayer-Kiener, V., Mendez-Martin, F., Schmatz, J., Sachsenhofer, R.F., 2018. Factors controlling shale microstructure and porosity: A case study on upper Visean Rudov beds from the Ukrainian Dneiper–Donets Basin. AAPG Bull. 102, 2629–2654. https://doi.org/10.1306/05111817295

Misch, D., Klaver, J., Gross, D., Rustamov, J., Sachsenhofer, R.F., Schmatz, J., Urai, J.L., 2020. Pore space characteristics of the Upper Visean ‘Rudov Beds’: insights from broad ion beam scanning electron microscopy and organic geochemical investigations. Geol. Soc. Lond. Spec. Publ. 484, 205–228. https://doi.org/10.1144/SP484.9

Misch, D., Riedl, F., Liu, B., Horsfield, B., Ziegs, V., Mendez-Martin, F., Vranjes-Wessely, S., Sachsenhofer, R.F., 2019b. Petrographic and sorption-based characterization of bituminous organic matter in the Mandal Formation, Central Graben (Norway). Int. J. Coal Geol. 211, 103229. https://doi.org/10.1016/j.coal.2019.103229

Nečas, D., Klapetek, P., 2012. Gwyddion: an open-source software for SPM data analysis. Open Phys. 10. https://doi.org/10.2478/s11534-011-0096-2

Noah, M., Horsfield, B., Han, S., Wang, C., 2020. Precise maturity assessment over a broad dynamic range using polycyclic and heterocyclic aromatic compounds. Org. Geochem. 148, 104099. https://doi.org/10.1016/j.orggeochem.2020.104099

Oliver, W.C., Pharr, G.M., 2010. Nanoindentation in materials research: Past, present, and future. MRS Bull. 35, 897–907. https://doi.org/10.1557/mrs2010.717

Oliver, W.C., Pharr, G.M., 2004. Measurement of hardness and elastic modulus by instrumented indentation: Advances in understanding and refinements to methodology. J. Mater. Res. 19, 3–20. https://doi.org/10.1557/jmr.2004.19.1.3

Oliver, W.C., Pharr, G.M., 1992. An improved technique for determining hardness and elastic modulus using load and displacement sensing indentation experiments. J. Mater. Res. 7, 1564–1583. https://doi.org/10.1557/JMR.1992.1564

Oyen, M.L., 2013. Nanoindentation of Biological and Biomimetic Materials. Exp. Tech. 37, 73–87. https://doi.org/10.1111/j.1747-1567.2011.00716.x

Pedregosa, F., Varoquaux, G., Gramfort, A., Michel, V., Thirion, B., Grisel, O., Blondel, M., Prettenhofer, P., Weiss, R., Dubourg, V., Vanderplas, J., Passos, A., Cournapeau, D., Brucher, M., Perrot, M., Duchesnay, É., 2011. Scikit-learn: Machine Learning in Python. J. Mach. Learn. Res. 12, 2825–2830.

Pfeifenberger, M.J., Mangang, M., Wurster, S., Reiser, J., Hohenwarter, A., Pfleging, W., Kiener, D., Pippan, R., 2017. The use of femtosecond laser ablation as a novel tool for rapid micro-mechanical sample preparation. Mater. Des. 121, 109–118. https://doi.org/10.1016/j.matdes.2017.02.012

Pfeifenberger, M.J., Milassin, G., Hohenwarter, A., Putz, B., Semprimoschnig, C.O.A., Pippan, R., 2019. Electron Irradiation Effects on Strength and Ductility of Polymer Foils Studied by Femtosecond Laser-Processed Micro-Tensile Specimens. Materials 12, 1468. https://doi.org/10.3390/ma12091468

Revil, A., Grauls, D., Brévart, O., 2002. Mechanical compaction of sand/clay mixtures: COMPACTION OF SAND-CLAY MIXTURES. J. Geophys. Res. Solid Earth 107, ECV 11-1-ECV 11-15. https://doi.org/10.1029/2001JB000318

Rousseeuw, P.J., 1987. Silhouettes: A graphical aid to the interpretation and validation of cluster analysis. J. Comput. Appl. Math. 20, 53–65. https://doi.org/10.1016/0377-0427(87)90125-7

Sayers, C.M., 2013. The effect of kerogen on the elastic anisotropy of organic-rich shales. GEOPHYSICS 78, D65–D74. https://doi.org/10.1190/geo2012-0309.1

Schieber, J., 2013. SEM Observations on Ion-milled Samples of Devonian Black Shales from Indiana and New YorkThe Petrographic Context of Multiple Pore Types, in: Electron Microscopy of Shale Hydrocarbon Reservoirs. American Association of Petroleum Geologists. https://doi.org/10.1306/13391711M1023589

Scipioni, L., Sanford, C.A., Notte, J., Thompson, B., McVey, S., 2009. Understanding imaging modes in the helium ion microscope. J. Vac. Sci. Technol. B Microelectron. Nanometer Struct. 27, 3250. https://doi.org/10.1116/1.3258634

Shukla, P., Kumar, V., Curtis, M., Sondergeld, C.H., Rai, C.S., 2013. Nanoindentation Studies on Shales. ARMA 13-578, 47th U.S. Rock Mechanics/Geomechanics Symposium, San Francisco, California.

Shukla, P., Taneja, S., Sondergeld, C., Rai, C., 2015. Nanoindentation Measurements on Rocks, in: Carroll, J., Daly, S. (Eds.), Fracture, Fatigue, Failure, and Damage

Evolution, Volume 5, Conference Proceedings of the Society for Experimental Mechanics Series. Springer International Publishing, Cham, pp. 99–105. https://doi.org/10.1007/978-3-319-06977-7_13

Sijbrandij, S., Notte, J., Sanford, C., Hill, R., 2010. Analysis of subsurface beam spread and its impact on the image resolution of the helium ion microscope. J. Vac. Sci. Technol. B Nanotechnol. Microelectron. Mater. Process. Meas. Phenom. 28, C6F6-C6F9. https://doi.org/10.1116/1.3497012

Sudharshan Phani, P., Oliver, W.C., 2019. A critical assessment of the effect of indentation spacing on the measurement of hardness and modulus using instrumented indentation testing. Mater. Des. 164, 107563. https://doi.org/10.1016/j.matdes.2018.107563

Thom, C., Goldsby, D., 2019. Nanoindentation Studies of Plasticity and Dislocation Creep in Halite. Geosciences 9, 79. https://doi.org/10.3390/geosciences9020079

Thorndike, R.L., 1953. Who belongs in the family? Psychometrika 18, 267–276. https://doi.org/10.1007/BF02289263

Ulm, F.-J., Abousleiman, Y., 2006. The nanogranular nature of shale. Acta Geotech. 1, 77–88. https://doi.org/10.1007/s11440-006-0009-5

Valenza, J.J., Drenzek, N., Marques, F., Pagels, M., Mastalerz, M., 2013. Geochemical controls on shale microstructure. Geology 41, 611–614. https://doi.org/10.1130/G33639.1

Vignesh, B., Oliver, W.C., Kumar, G.S., Phani, P.S., 2019. Critical assessment of high speed nanoindentation mapping technique and data deconvolution on thermal barrier coatings. Mater. Des. 181, 108084. https://doi.org/10.1016/j.matdes.2019.108084

Vranjes, S., Misch, D., Schöberl, T., Kiener, D., Gross, D., Sachsenhofer, R.F., 2018. Nanoindentation study of macerals in coals from the Ukrainian Donets Basin. Adv. Geosci. 45, 73–83. https://doi.org/10.5194/adgeo-45-73-2018

Vranjes-Wessely, S., Misch, D., Issa, I., Kiener, D., Fink, R., Seemann, T., Liu, B., Rantitsch, G., Sachsenhofer, R.F., 2020. Nanoscale pore structure of Carboniferous coals from the Ukrainian Donets Basin: A combined HRTEM and gas sorption study. Int. J. Coal Geol. 224, 103484. https://doi.org/10.1016/j.coal.2020.103484

Wang, P., Zhang, C., Li, X., Zhang, K., Yuan, Y., Zang, X., Cui, W., Liu, S., Jiang, Z., 2020. Organic matter pores structure and evolution in shales based on the he ion microscopy (HIM): A case study from the Triassic Yanchang, Lower Silurian Longmaxi and Lower Cambrian Niutitang shales in China. J. Nat. Gas Sci. Eng. 84, 103682. https://doi.org/10.1016/j.jngse.2020.103682

Ward, B.W., Notte, J.A., Economou, N.P., 2006. Helium ion microscope: A new tool for nanoscale microscopy and metrology. J. Vac. Sci. Technol. B Microelectron. Nanometer Struct. 24, 2871. https://doi.org/10.1116/1.2357967

Wei, L., Mastalerz, M., Schimmelmann, A., Chen, Y., 2014. Influence of Soxhlet-extractable bitumen and oil on porosity in thermally maturing organic-rich shales. Int. J. Coal Geol. 132, 38–50. https://doi.org/10.1016/j.coal.2014.08.003

Wu, T., Zhao, J., Zhang, W., Zhang, D., 2020. Nanopore structure and nanomechanical properties of organic-rich terrestrial shale: An insight into technical issues for hydrocarbon production. Nano Energy 69, 104426. https://doi.org/10.1016/j.nanoen.2019.104426

Yang, C., Xiong, Y., Wang, J., Li, Y., Jiang, W., 2020. Mechanical characterization of shale matrix minerals using phase-positioned nanoindentation and nano-dynamic mechanical analysis. Int. J. Coal Geol. 229, 103571. https://doi.org/10.1016/j.coal.2020.103571

Yang, J., Hatcherian, J., Hackley, P.C., Pomerantz, A.E., 2017. Nanoscale geochemical and geomechanical characterization of organic matter in shale. Nat. Commun. 8, 2179. https://doi.org/10.1038/s41467-017-02254-0

Yin, H., Zhang, G., 2011. Nanoindentation Behavior of Muscovite Subjected to Repeated Loading. J. Nanomechanics Micromechanics 1, 72–83. https://doi.org/10.1061/(ASCE)NM.2153-5477.0000033

Zargari, S., Wilkinson, T.M., Packard, C.E., Prasad, M., 2016. Effect of thermal maturity on elastic properties of kerogen. GEOPHYSICS 81, M1–M6. https://doi.org/10.1190/geo2015-0194.1

Zeszotarski, J.C., Chromik, R.R., Vinci, R.P., Messmer, M.C., Michels, R., Larsen, J.W., 2004. Imaging and mechanical property measurements of kerogen via nanoindentation. Geochim. Cosmochim. Acta 68, 4113–4119. https://doi.org/10.1016/j.gca.2003.11.031

Zhao, J., Zhang, W., Zhang, D., Wei, R., Wang, Y., 2020. Influence of Geochemical Features on the Mechanical Properties of Organic Matter in Shale. J. Geophys. Res. Solid Earth 125. https://doi.org/10.1029/2020JB019809

Zhu, W., Hughes, J.J., Bicanic, N., Pearce, C.J., 2007. Nanoindentation mapping of mechanical properties of cement paste and natural rocks. Mater. Charact. 58, 1189–1198. https://doi.org/10.1016/j.matchar.2007.05.018